PTB bericht
Wissenschaftliche Veröffentlichungen
Diss-36
September 2026

Dissertation

Elena Kononogova

A Novel Instrumentation for Validated Directional–Hemispherical Reflectance Measurements in the Far-Infrared

ISSN 2941-1297
ISBN 978-3-944659-68-8

DOI 10.7795/110.20260928

Elena Kononogova

A Novel Instrumentation for Validated Directional–Hemispherical Reflectance Measurements in the Far-Infrared

Dissertation

PTB-Diss- 36

Braunschweig, September 2026

ISSN 2751-6598
ISBN 978-3-944659-68-8

DOI 10.7795/110.20260928

Empfohlene Zitierweise/recommended citation

Kononogova, E., 2026. *A Novel Instrumentation for Validated Directional Hemispherical Reflectance Measurements in the Far-Infrared*, Technische Universität Berlin. Braunschweig: Physikalisch-Technische Bundesanstalt. PTB-Bericht Diss-36. ISBN 978-3-944659-68-8.
Verfügbar unter: https://doi.org/10.7795/110.20260928

Herausgeber:
Physikalisch-Technische Bundesanstalt
ISNI: 0000 0001 2186 1887

Presse und Öffentlichkeitsarbeit

Bundesallee 100
38116 Braunschweig

Telefon: (05 31) 592-93 21
Telefax: (05 31) 592-92 92
www.ptb.de

TECHNISCHE UNIVERSITÄT BERLIN

A Novel Instrumentation for Validated Directional–Hemispherical Reflectance Measurements in the Far-Infrared

vorgelegt von

Elena Kononogova, Dipl.-Ing.

an der Fakultät IV – Elektrotechnik und Informatik
der Technischen Universität Berlin
zur Erlangung des akademischen Grades

Doktorin der Naturwissenschaften
- Dr. rer. nat. -

genehmigte Dissertation

Promotionsausschuss:

Vorsitzende:	Prof. Dr.-Ing. Dorothea Kolossa
Gutachter:	Prof. Dr.-Ing. Stephan Völker
Gutachter:	Prof. Dr. Jürgen Hartmann (Technische Hochschule Würzburg Schweinfurt)
Gutachter:	Dr. Christian Monte (PTB Berlin)

Tag der wissenschaftlichen Aussprache: 24. August 2026

Berlin 2026

https://doi.org/10.7795/110.20260928

https://doi.org/10.7795/110.20260928

Abstract

Accurate far-infrared (FIR) radiative data are required for thermal radiation modelling, climate research, remote sensing, space instrumentation, and infrared optical metrology. In particular, directional–hemispherical reflectance in the wavelength range from 25 µm to 100 µm is needed when both specular and diffuse radiation contributions must be considered. However, conventional integrating spheres cannot be directly transferred to this spectral range, because established diffuse coatings exhibit increased absorption and metallic surfaces tend to reflect predominantly specularly at long wavelengths. This creates a metrological gap for traceable far-infrared reflectance measurements with validated uncertainty budgets.

In this work, a novel integrating sphere system for directional–hemispherical reflectance measurements in the far-infrared spectral range was developed, realized, and experimentally validated. The system is based on a structured internal surface topology designed to provide diffuse-like angular redistribution while maintaining high reflectance. For this purpose, a Random Harmonic Function Surface topology (RHFS-800) was developed and optimized, transferred to a spherical geometry, manufactured by stereolithography-based additive manufacturing, and gold-coated.

The integrating sphere was coupled to a Bruker VERTEX 80v Fourier-transform infrared (FTIR) spectrometer using a dedicated external optical relay system. The complete setup, referred to as the Far-Infrared Integrating Sphere (FIR-IS), enables controlled incident and detected radiation paths and supports directional–hemispherical reflectance measurements using the substitution method. A radiometric correction model was implemented to account for finite sphere-wall reflectance, port geometry, and residual background signal. A spectral uncertainty budget was established in accordance with the Guide to the Expression of Uncertainty in Measurement (GUM), and expanded uncertainties were reported with a coverage factor of $k = 2$.

The developed system was validated using samples with different radiative properties, including low-reflectance, high-reflectance, and semi-transparent coatings. The measured directional–hemispherical reflectance spectra were compared with independent Physikalisch-Technische Bundesanstalt (PTB) reference data obtained from spectral emittance and directional reflectance measurements. The results show good

https://doi.org/10.7795/110.20260928

agreement within the expanded uncertainty and demonstrate that the FIR-IS can reproduce both the overall reflectance level and characteristic spectral features of the investigated samples.

This work establishes a design, fabrication, correction, and validation methodology for far-infrared integrating sphere radiometry. The FIR-IS provides a metrological tool for material characterization and supports applications in thermal radiometry, radiative transfer modelling, space instrumentation, and climate-related missions such as the European Space Agency (ESA) Far-infrared Outgoing Radiation Understanding and Monitoring (FORUM) mission.

https://doi.org/10.7795/110.20260928

List of Abbreviations

Abbreviation	Meaning
A515	Bruker external reflection unit / external reflection accessory
A519	Bruker reflectance accessory for directional–directional spectral reflectance measurements
BRDF	Bidirectional Reflectance Distribution Function
CAD	Computer-Aided Design
CNC	Computer Numerical Control
DTGS	Deuterated Triglycine Sulfate
EMAF	Emissivity Measurements in Air Facility
ESA	European Space Agency
FDTGS	Far-infrared-optimized Deuterated Triglycine Sulfate
FIR	Far-Infrared
FIR-IS	Far-Infrared Integrating Sphere
FORUM	Far-infrared Outgoing Radiation Understanding and Monitoring
FTIR	Fourier Transform Infrared
GUM	Guide to the Expression of Uncertainty in Measurement
IR	Infrared
ISO	International Organization for Standardization
LabVIEW	Laboratory Virtual Instrument Engineering Workbench

https://doi.org/10.7795/110.20260928

Abbreviation	Meaning
LED	Light-Emitting Diode
MCT	Mercury Cadmium Telluride
MIR	Mid-Infrared
NIR	Near-Infrared
NSC	Non-Sequential Component / Non-Sequential Mode
OAP	Off-axis parabolic mirror
OPUS	Bruker OPUS spectroscopy software
PMMA	Polymethyl methacrylate
PT100	Platinum resistance temperature sensor
PTB	Physikalisch-Technische Bundesanstalt
PTFE	Polytetrafluoroethylene
RBS	Random Ball Surface(s)
RHFS	Random Harmonic Function Surface(s)
SLA	Stereolithography
SLM	Selective Laser Melting
SLS	Selective Laser Sintering
THz	Terahertz
UV-Vis-NIR	Ultraviolet–Visible–Near-Infrared

https://doi.org/10.7795/110.20260928

Chemical and material designations

Designation	Meaning
Au	Gold
$BaSO_4$	Barium sulfate
CaF_2	Calcium fluoride
KBr	Potassium bromide
NiCr	Nickel–chromium adhesion layer
Y_2O_3	Yttrium oxide
EN AW-6061-T6	Aluminium alloy designation

List of Symbols

Symbol	Meaning	Unit
c	speed of light in vacuum	$m \cdot s^{-1}$
λ	wavelength	m
$\tilde{\nu}$	wavenumber	cm^{-1}
$S(\tilde{\nu})$	spectral intensity	arbitrary units
$I(x)$	interferogram	arbitrary units
ν	frequency	s^{-1}
E	photon energy	J

https://doi.org/10.7795/110.20260928

Symbol	Meaning	Unit
h	Planck constant	J·s
T	temperature	K
b	Wien's displacement constant	m·K
λ_{max}	wavelength of maximum blackbody emission	m
ε	emissivity	–
ε_λ	spectral emissivity	–
α	absorptivity	–
α_λ	spectral absorptivity	–
ρ	reflectivity	–
ρ_λ	spectral reflectivity	–
τ	transmissivity	–
τ_λ	spectral transmissivity	–
$e(\lambda)$	measured directional spectral emittance	–
R	reflectance	–
$R_{d-h,\lambda}$	directional–hemispherical spectral reflectance	–
$R_m(\lambda)$	measured reflectance obtained from the sample/reference signal ratio	–
$R_s(\lambda)$	corrected directional–hemispherical reflectance of the sample	–
$R_{s,+}(\lambda)$	corrected reflectance for positive perturbation	–

https://doi.org/10.7795/110.20260928

Symbol	Meaning	Unit
$R_{s,-}(\lambda)$	corrected reflectance for negative perturbation	–
$\Delta_i(R_s, \lambda)$	numerical variation associated with perturbation of input quantity x_i	–
$R_g(\lambda)$	sphere-wall reflectance assigned to the gold-coated inner surface	–
$R_u(\lambda)$	underground signal / residual background signal	–
$S_{\text{sample}}(\lambda)$	spectral detector signal for sample measurement	arbitrary units
$S_{\text{reference}}(\lambda)$	spectral detector signal for reference measurement	arbitrary units
θ	polar angle	rad or °
ϕ	azimuthal angle	rad or °
θ_i	angle of incidence	rad or °
ϕ_i	azimuthal angle of incidence	rad or °
θ_r	reflection angle	rad or °
ϕ_r	azimuthal angle of reflection	rad or °
L	spectral radiance	$\mathrm{W \cdot m^{-3} \cdot sr^{-1}}$
L_e	emitted spectral radiance of a surface	$\mathrm{W \cdot m^{-3} \cdot sr^{-1}}$
L_{bb}	spectral radiance of a blackbody	$\mathrm{W \cdot m^{-3} \cdot sr^{-1}}$
L_i	incident spectral radiance	$\mathrm{W \cdot m^{-3} \cdot sr^{-1}}$
L_t	transmitted spectral radiance	$\mathrm{W \cdot m^{-3} \cdot sr^{-1}}$
L_r	reflected spectral radiance	$\mathrm{W \cdot m^{-3} \cdot sr^{-1}}$

https://doi.org/10.7795/110.20260928

Symbol	Meaning	Unit
I_r	reflected radiant intensity	$\mathrm{W \cdot sr^{-1}}$
Φ	radiant flux	W
Φ_{inc}	incident radiant flux	W
Φ_{abs}	absorbed radiant flux	W
Φ_D	radiant flux reaching the detector	W
Φ_{sample}	radiant flux interacting with the sample	W
A_{sphere}	internal surface area of integrating sphere	m²
A_{ports}	total open-port area	m²
A_{sample}	area of the sample	m²
A_{gold}	effective area of gold-coated inner sphere wall	m²
D	sphere diameter	m
d_p	representative port diameter	m
d_s	sample port diameter	m
f	port fraction	–
f_s	fractional area of sample	–
f_g	fractional area of gold-coated sphere wall	–
f_{total}	total effective reflective fraction	–
M	sphere multiplier	–
T_{SD}	transfer coefficient between sample and detector ports	–

https://doi.org/10.7795/110.20260928

Symbol	Meaning	Unit
r_{min}	minimum radius of random spherical scatterers	mm
r_{max}	maximum radius of random spherical scatterers	mm
N	number of harmonic components or spherical scatterers	–
x, y	Cartesian coordinates on planar surface	m
$h_{RHFS}(x, y)$	generated planar RHFS surface height field	m or mm
a_n	amplitude coefficient of harmonic component	m or mm
k_n	spatial frequency of harmonic component	m^{-1} or mm^{-1}
φ_n	random phase in x-direction	rad
ϕ_n	random phase in y-direction	rad
dA	differential surface area element	m^2
z	surface height coordinate	m or mm
$h_i(\theta, \phi)$	local interpolation function for sphere segment (i)	m or mm
ϕ'	corrected azimuthal coordinate	rad
r	sphere radius	m or mm
r_0	reference sphere radius	m or mm
$r(\theta, \phi)$	radial coordinate of structured sphere surface	m or mm
$h(\theta, \phi')$	mapped surface relief in spherical coordinates	m or mm
δ	electromagnetic skin depth	m

https://doi.org/10.7795/110.20260928

Symbol	Meaning	Unit
ω	angular frequency	rad·s^{-1}
μ	magnetic permeability	H·m^{-1}
σ_{el}	electrical conductivity	S·m^{-1}
G	optical throughput / étendue	m²·sr
A_{beam}	beam cross-sectional area	m²
Ω	solid angle	sr
f_{focal}	focal length of mirror	mm
$x(\lambda)$	auxiliary correction parameter	–
x_i	generic input quantity in uncertainty propagation	depends on quantity
$u(x_i)$	standard uncertainty of input quantity x_i	unit of x_i
u_c	combined standard uncertainty	–
U	expanded uncertainty	–
k	coverage factor	–
s	experimental standard deviation	unit of quantity
n	number of repeated measurements	–
$\Delta\phi$	phase shift between spectral modulations	rad or °

https://doi.org/10.7795/110.20260928

Physical Constants

c	speed of light in vacuum	2.99792458×10^{8}	$\mathrm{m \cdot s^{-1}}$
h	Planck constant	$6.62607015 \times 10^{-34}$	J·s
k_B	Boltzmann constant	1.380649×10^{-23}	$\mathrm{J \cdot K^{-1}}$
σ	Stefan–Boltzmann constant	5.670374×10^{-8}	$\mathrm{W \cdot m^{-2} \cdot K^{-4}}$
b	Wien's displacement constant	$2.897771955 \times 10^{-3}$	m·K

https://doi.org/10.7795/110.20260928

Contents

Abstract 3
List of Abbreviations 5
Chemical and material designations 7
List of Symbols 7
Physical Constants 13
Contents 14
Introduction 18
Chapter 1. Theory 23
1.1 Electromagnetic Waves and the Far-Infrared Spectral Range 23
1.1.1 Electromagnetic radiation 23
1.1.2 Spectral classification of electromagnetic radiation 24
1.1.3 The far-infrared spectral range 25
1.2 Radiative Properties at Interfaces: Definitions and Characteristics 26
1.2.1 Emissivity 27
1.2.2 Absorptivity 28
1.2.3 Transmissivity 29
1.2.4 Reflectivity 30
1.2.5 Conservation of energy in radiative interactions 33
1.3 Methods of Measuring Radiation in the FIR Range 34
1.3.1 Detector technologies used in this work 35
1.3.2 Fourier Transform Infrared spectroscopy in the FIR 36
1.3.3 Integrating sphere–based FTIR measurements 37
1.4 Integrating Sphere Theory 39
1.4.1 Physical principle of integrating sphere operation 39
1.4.2 Geometrical and optical parameters 40
1.4.3 Sphere multiplier and radiative transfer 41

https://doi.org/10.7795/110.20260928

1.4.4 Applications in optical metrology 42
1.4.5 Limitations of conventional integrating spheres in the FIR 42
1.4.6 Need for new integrating sphere concepts for FIR 43
Chapter 2. Development of Diffuse-Scattering Surfaces for the Far-Infrared Range 44
2.1 Physical Principles of Diffuse Reflection in the Far-Infrared 44
2.2 Surface Concepts for FIR Diffuse Reflection 46
2.2.1 Random Ball Surfaces (RBS) 47
2.2.2 Random Harmonic Function Surfaces (RHFS) 49
2.3 Ray Tracing in Diffuse Surface Analysis Using Zemax 52
2.4 Sample Manufacturing 55
2.4.1 Manufacture of random ball surfaces (RBS) 56
2.4.2 Manufacture of random harmonic function surfaces (RHFS) 58
2.5 Surface Analysis and THz Measurements 60
2.6 Measurement Results 63
2.6.1 Reference measurements: Gold mirror and Infragold 63
2.6.2 RBS: reproducibility limitations 64
2.6.3 RHFS-200: predominantly specular behaviour 66
2.6.4 RHFS-400: transitional scattering regime 67
2.6.5 RHFS-800: broadband diffuse scattering 68
Chapter 3. Design and Fabrication of the Far-Infrared Integrating Sphere 71
3.1 Concept and Design Requirements 72
3.2 Transfer of the RHFS-800 Surface into Spherical Geometry 73
3.3 Sphere Geometry Design 77
3.3.1 Measurement-driven geometrical concept 78
3.3.2 Sphere size and port configuration 81
3.3.3 Integration of geometry and surface topology 82
3.4 Fabrication and Additive Manufacturing of the Integrating Sphere 83

https://doi.org/10.7795/110.20260928

3.4.1 Manufacturing requirements derived from FIR radiometry and RHFS-800 geometry 84
3.4.2 Additive manufacturing process 87
3.4.3 Metallization and gold coating 90
3.4.4 Gold coating physics and optical behaviour 93
3.4.5 Outgassing and material suitability 95
3.4.6 Final assembly, development outcome and relevance to FIR integrating-sphere realization 97
Chapter 4. Development of the Optical Measurement Setup 101
4.1 Throughput Preservation and Aperture Matching 101
4.2 Optical Path Design 104
4.2.1 Optical function of the A515 unit 105
4.2.2 Incident radiation path 107
4.2.3 Detected radiation path 109
4.2.4 Optical relay implementation 110
4.2.5 Alignment methodology 111
4.3 Environmental Enclosure 113
Chapter 5. Measurements, Radiometric Correction and Validation 116
5.1 Measurement Concept 118
5.2 Radiometric Correction of Integrating Sphere Measurements 123
5.2.1 Necessity of integrating sphere correction 123
5.2.2 Geometrical parameters of the integrating sphere 124
5.2.3 Measured quantities 125
5.2.4 Correction equations 126
5.2.5 Implementation of the correction in LabVIEW 128
5.2.6 Processing sequence 130
5.3 Uncertainty Analysis 130
5.3.1 General approach 130

https://doi.org/10.7795/110.20260928

5.3.2 Input quantities and classification 132
5.3.3 Uncertainty propagation method 143
5.4 Results and validation 147
5.4.1 Nextel 811-21 149
5.4.2 Laser-structured gold-coated sample 152
5.4.3 Aeroglaze Z306 coating (99 µm) 155
Conclusion 159
Acknowledgements 163
References 164

https://doi.org/10.7795/110.20260928

Introduction

The far-infrared (FIR) spectral region, typically defined as spanning wavelengths from 25 µm to 1000 µm, is of central relevance for the description of thermal radiation processes in natural and engineered systems. A significant fraction of the thermal radiation emitted by objects at terrestrial temperatures lies within this spectral range when integrated over wavelength. In the FIR, the radiative response of matter is governed primarily by lattice vibrations in solids and rotational transitions in gases. As a result, accurate FIR measurements are required in a wide range of applications, including climate science, atmospheric physics, astrophysics, space instrumentation, materials science, and thermal engineering [1, 2, 3, 4].

From a radiometric perspective, the FIR region represents the long-wavelength part of the thermal emission spectrum, where photon energies are low and detector sensitivities decrease significantly. Consequently, the accurate determination of radiative quantities is inherently challenging. Weak signal levels, strong atmospheric absorption, particularly due to water vapour, and wavelength-scale surface effects introduce specific metrological constraints that are not encountered in shorter spectral regions [3].

In recent years, the demand for accurate FIR radiometric data has increased substantially, particularly in the context of climate monitoring and Earth observation. The infrared spectral region contributes significantly to the Earth's outgoing longwave radiation and is therefore essential for understanding radiative feedback mechanisms in the climate system [4]. Recent laboratory studies of water-vapour continuum absorption further demonstrate that improved infrared spectroscopic data can affect calculated outgoing longwave radiation and therefore remain relevant for climate-oriented radiative transfer modelling [5]. This requirement is directly reflected in current and upcoming space missions, such as the European Space Agency (ESA) FORUM mission, which aims to measure the Earth's outgoing radiation in the spectral range from 25 µm to 100 µm with high accuracy [6, 7, 8]. Achieving the objectives of such missions requires traceable, stable, and well-characterized optical measurement systems operating in the FIR.

Beyond space applications, reliable FIR radiometric data are required for the establishment of calibration chains at national metrology institutes. In this context,

https://doi.org/10.7795/110.20260928

experimentally determined quantities such as reflectance, transmittance, and emittance serve as reference quantities for industrial and scientific applications. The absence of suitable measurement tools for directional–hemispherical reflectance and transmittance in the FIR therefore represents not only a scientific gap, but also a metrological limitation affecting traceability and uncertainty evaluation in long-wavelength radiometry [9, 10].

A central challenge in FIR radiometry is the accurate determination of radiative quantities under defined angular conditions. For many technical materials, the reflected or transmitted radiation contains both specular and diffuse contributions. A purely directional measurement records only radiation within a limited observation direction and may therefore provide incomplete information when significant scattering is present. In contrast, directional–hemispherical reflectance and transmittance describe the total reflected or transmitted radiant flux collected over the corresponding hemisphere for a specified direction of incidence. These quantities are particularly relevant for radiative transfer modelling, material characterization, and calibration of optical systems in which the total redistributed flux is required [1, 11, 12].

Integrating spheres are well-established instruments for determining directional–hemispherical reflectance and transmittance in the ultraviolet, visible, and near-infrared spectral ranges [9, 10, 13, 14]. Their function is to collect radiation reflected or transmitted by a sample over a hemisphere and redistribute it within the cavity by multiple reflections. In this way, the detector signal becomes largely independent of the detailed angular scattering distribution within the collected hemisphere. However, the measured quantity remains defined by the illumination geometry; for example, a measurement performed at an incidence angle of 8° represents the directional–hemispherical reflectance for that specific incidence condition.

Although integrating spheres are mature and standardized in shorter spectral ranges, their direct transfer to the FIR is not possible. Diffuse reflector materials commonly used in the ultraviolet, visible, and near-infrared ranges, such as polytetrafluoroethylene (PTFE)-based materials and barium sulfate coatings, are optimized for shorter wavelengths and do not provide suitable diffuse-reflectance performance for mid-infrared (MIR) and FIR integrating-sphere operation [14, 15]. In the MIR, gold-based diffuse reflectance standards such as Infragold are commonly used [15]. However, at far-infrared wavelengths, the characteristic surface structure of such standards

https://doi.org/10.7795/110.20260928

becomes small compared with the wavelength. As a result, the diffuse fraction of the reflected radiation decreases and the reflection becomes increasingly directional. Consequently, established diffuse reflectance standards do not provide the required combination of high reflectance and sufficiently diffuse angular redistribution for integrating-sphere operation in the far-infrared spectral range [16, 17, 18, 19].

In addition to material-related limitations, the optical behaviour of surfaces in the FIR differs fundamentally from that at shorter wavelengths. As the wavelength becomes comparable to characteristic surface features, scattering behaviour transitions from micro-scale roughness scattering to geometrically governed reflection regimes. Surfaces that are optically rough in the visible may behave as comparatively smooth in the FIR, while specifically structured surfaces with wavelength-scale features can promote diffuse-like angular redistribution. Consequently, an integrating sphere for FIR operation requires not only a highly reflective internal surface, but also a surface topology specifically designed to redistribute radiation at long wavelengths [16, 17, 18, 19].

Without an integrating sphere optimized for the FIR, directional–hemispherical measurements require angular-resolved setups, in which the reflected or transmitted radiation must be sampled over many directions and subsequently integrated. Such approaches are technically demanding, time-consuming, and sensitive to alignment, detector nonlinearity, angular sampling, and stability of the radiation source. The absence of spatially integrating measurement concepts therefore directly limits achievable uncertainty budgets in FIR radiometry [9, 10].

Despite previous work on infrared and far-infrared diffuse reflecting surfaces [20], no integrating sphere concept specifically optimized for the spectral range from 25 µm to 100 µm has been experimentally validated with a quantified uncertainty budget [10, 19]. Existing long-wavelength sphere concepts are either limited to the mid-infrared spectral range or rely on metallic cavities without controlled diffuse-like angular redistribution [9, 10, 13, 14].

The objective of this dissertation is the development, realization, and experimental validation of an integrating sphere system designed for directional–hemispherical reflectance measurements in the far-infrared spectral range. The work addresses the coupled challenges of surface topology design, spherical geometry implementation, additive manufacturing, metallic coating, optical coupling to a Fourier-transform

https://doi.org/10.7795/110.20260928

infrared (FTIR) spectrometer, radiometric correction, and uncertainty evaluation. In contrast to conventional developments, in which surface coating, mechanical realization, and measurement configuration are often treated separately, the present work approaches the system as a coupled radiometric instrument.

To address the lack of suitable diffuse reflectors in the FIR, a structured internal surface topology based on Random Harmonic Function Surfaces is developed. The RHFS concept enables the generation of reproducible stochastic surface structures with characteristic dimensions compatible with far-infrared wavelengths. The selected RHFS-800 topology is transferred from a planar surface to a spherical geometry and forms the functional internal surface of the integrating sphere. The sphere is fabricated by stereolithography-based additive manufacturing and metallized with gold to provide a high-reflectance, low-loss boundary for multiple internal reflections.

In addition to the sphere design, the work includes the optical measurement setup required for coupling to a Bruker VERTEX 80v FTIR spectrometer. The integrating sphere is coupled to the spectrometer by means of a dedicated external optical relay system. This configuration separates the incident and detected radiation paths, preserves optical throughput, and allows operation with different detector configurations. The setup, referred to as FIR-IS, is experimentally evaluated using the substitution method.

The experimental validation presented in this dissertation focuses on directional–hemispherical reflectance measurements. Although the sphere design also supports transmittance configurations, the final validation results are based on reflectance measurements. A radiometric correction model is implemented to account for finite sphere-wall reflectance, geometrical port effects, and residual background signal. In addition, a spectral uncertainty budget is established in accordance with the Guide to the Expression of Uncertainty in Measurement (GUM). The measurement results are compared with independent reference data obtained at the Physikalisch-Technische Bundesanstalt (PTB), providing a metrological basis for evaluating the performance of the developed system [21].

The integrating sphere developed within this work extends the available experimental methods for far-infrared material characterization and long-wavelength radiometry. It is relevant for thermal engineering, infrared material science, radiative

https://doi.org/10.7795/110.20260928

transfer modelling, and space-related applications. In particular, traceable laboratory measurements in the 25 µm to 100 µm range are important for climate-oriented missions such as ESA FORUM, where reliable FIR radiative data are required for instrument calibration, model validation, and interpretation of outgoing longwave radiation.

The dissertation is structured as follows. Chapter 1 introduces the theoretical foundations of far-infrared radiation, radiative quantities, detector technologies, FTIR spectroscopy, and integrating sphere theory. Chapter 2 presents the modelling, fabrication, and evaluation of diffuse-scattering surface topologies for the FIR, leading to the selection of the RHFS-800 surface. Chapter 3 describes the transfer of this topology to spherical geometry, the fabrication of the integrating sphere, and the gold-coating characterization. Chapter 4 presents the external optical relay system used to couple the FIR-IS to the FTIR spectrometer. Chapter 5 describes the measurement concept, radiometric correction, uncertainty analysis, experimental validation, and comparison with PTB reference data.

https://doi.org/10.7795/110.20260928

Chapter 1. Theory

This chapter summarizes the theoretical concepts required for the physical and metrological aspects of FIR radiometry in the context of directional–hemispherical reflectance and transmittance measurements.

The focus is placed on the physical aspects of electromagnetic radiation that are directly relevant to long wavelengths, including thermal emission, interaction of FIR radiation with matter, and scattering phenomena at wavelengths comparable to characteristic surface-structure dimensions. Particular attention is given to directional–hemispherical radiative quantities and to the physical interpretation of diffuse and directional reflection.

In addition, the chapter outlines the principles of FIR detection and highlights the limitations imposed by low photon energies and weak thermal signals. The theoretical concepts introduced here form the basis for the surface design presented in Chapter 2 and for the integrating sphere implementation developed in the subsequent chapters.

1.1 Electromagnetic Waves and the Far-Infrared Spectral Range

1.1.1 Electromagnetic radiation

Electromagnetic radiation consists of coupled oscillations of electric and magnetic fields that propagate through space at the speed of light in vacuum. It is fully described by its wavelength λ in vacuum, frequency ν, and photon energy E.

The relationship between wavelength and frequency is given by

$$c = \lambda\nu \qquad (1.1)$$

where c denotes the speed of light in vacuum. The photon energy is related to the frequency by

$$E = h\nu \qquad (1.2)$$

where h is Planck's constant [1].

The broad range of possible wavelengths and frequencies forms the electromagnetic spectrum, within which different spectral regions exhibit distinct physical behaviour and technological relevance.

https://doi.org/10.7795/110.20260928

In optical and infrared radiometry, wavelength is a fundamental parameter, since it determines the interaction of radiation with matter [1, 2], influences the optical properties of materials, and defines the applicability of optical components and detector technologies. These interactions become particularly important in the infrared spectral range, where thermal radiation dominates and radiative properties are strongly wavelength dependent.

1.1.2 Spectral classification of electromagnetic radiation

For practical and historical reasons, the electromagnetic spectrum is divided into several spectral regions based on wavelength or frequency. While the exact boundaries may vary slightly between disciplines, the classification commonly used in optics and infrared spectroscopy is summarized in Table 1.1.

Spectral region	Wavelength range	Typical applications
Gamma rays	< 0.01 nm	Nuclear physics, medical imaging
X-rays	0.01–10 nm	Medical diagnostics, crystallography
Ultraviolet (UV)	10 - 400 nm	Sterilization, fluorescence
Visible	400 - 700 nm	Vision, illumination
Near infrared (NIR)	0.7 - 2.5 µm	Fiber optics, imaging
Mid infrared (MIR)	2.5 - 25 µm	Molecular spectroscopy, thermal imaging
Far infrared (FIR)	**25 µm - 1000 µm**	**Thermal radiation, astronomy, material analysis**
Microwaves	1 mm - 30 cm	Radar, communication
Radio waves	> 30 cm	Broadcasting, telecommunications

Table 1.1. Classification of electromagnetic radiation by spectral region, including corresponding wavelength ranges and representative applications.

In the context of this dissertation, particular emphasis is placed on the spectral range from 25 µm to 1000 µm, which is of central relevance for thermal radiation measurements and space-based climate observation.

https://doi.org/10.7795/110.20260928

1.1.3 The far-infrared spectral range

Infrared radiation occupies the spectral region between visible light and microwaves, extending approximately from 0.7 μm to 1000 μm in wavelength. The far-infrared range forms the long-wavelength part of the infrared spectrum and bridges the gap between the mid-infrared and microwave regions.

This wavelength range is of particular importance because it encompasses the dominant thermal emission of objects at cryogenic to ambient temperatures. According to Wien's displacement law, the wavelength at which a blackbody emits maximum radiation is given by

$$\lambda_{\max} = \frac{b}{T} \qquad (1.3)$$

where T is the absolute temperature and b is Wien's displacement constant [1].

Equation (1.3) shows that decreasing temperature shifts the peak of thermal emission toward longer wavelengths.

For example, the thermal radiation peak of the Sun at approximately 5800 K lies in the visible spectral range, while objects at room temperature (~300 K) emit predominantly in the infrared. At cryogenic temperatures, such as liquid nitrogen temperature (77 K), the emission peak shifts into the far-infrared region. Consequently, radiation in this spectral range is primarily associated with thermal emission from objects with temperatures ranging from a few kelvin up to several hundred kelvin.

In this spectral range, radiative behaviour is dominated by thermal processes, and radiative properties such as emissivity, reflectivity, and transmissivity exhibit strong wavelength dependence. Interaction mechanisms between radiation and matter include low-frequency vibrational modes in solids (phonons), rotational transitions in gases, and collective lattice excitations [2, 3].

Due to the long wavelengths involved, the interaction of radiation with surface topology differs significantly from that observed at shorter wavelengths. In the far-infrared spectral range, many technical and structured surfaces exhibit a combination of directional and diffuse reflection components. As a consequence, directional measurements alone are often insufficient for complete radiative characterization, and

https://doi.org/10.7795/110.20260928

directional–hemispherical quantities become particularly relevant for radiometric applications.

This has direct implications for optical measurements and motivates the use of integrating spheres for the determination of directional–hemispherical reflectance and transmittance, provided that their design, materials, and surface properties are adapted to operation at long wavelengths.

1.2 Radiative Properties at Interfaces: Definitions and Characteristics

When electromagnetic radiation encounters the interface between two media, such as air and a solid surface, it undergoes reflection, absorption, and transmission. The relative contribution of each process is governed by the radiative properties of the surface, which depend on wavelength, angle of incidence, polarization, temperature, and surface structure. These properties determine how energy is exchanged between radiation and matter and are therefore central to thermal radiation theory, optical metrology, climate science, astrophysics, and materials characterization [1, 11, 22].

In the FIR spectral range, radiative interactions are dominated by thermal processes, and radiative properties such as spectral emissivity, reflectivity, absorptivity, and transmissivity exhibit strong wavelength and angular dependence. For many technical and structured surfaces, directional measurements alone may not provide sufficient information for complete radiative characterization, particularly when diffuse and directional reflection components coexist. This makes integrating spheres particularly suitable for the determination of directional–hemispherical reflectance and transmittance, provided that their design, materials, and surface properties are properly adapted to this spectral range [9].

Throughout this work, the terminology follows ISO 80000-7 (Quantities and units — Part 7: Light and radiation) [22]. According to this convention, quantities ending in "-ivity" (e.g. emissivity, reflectivity, absorptivity, transmissivity) describe intrinsic material properties, whereas quantities ending in "-ance" (e.g. emittance, reflectance, absorptance, transmittance) denote radiometric quantities defined for a specific sample under specified spectral and geometrical measurement conditions. In accordance with this distinction, "-ivity" is used in the theoretical description of material

https://doi.org/10.7795/110.20260928

properties, while “-ance” is used when referring to experimentally determined quantities. Accordingly, the quantities measured with the integrating sphere in this work are referred to as directional–hemispherical reflectance and transmittance, because they are defined by the specific measurement geometry and sample configuration.

1.2.1 Emissivity

Emissivity describes the radiative emission of a real surface relative to that of an ideal blackbody at the same temperature. The directional spectral emissivity is defined as the ratio of the emitted spectral radiance of the surface to the spectral radiance of a blackbody

$$\varepsilon(\lambda, \theta, \varphi, T) = \frac{L_e(\lambda, \theta, \varphi, T)}{L_{bb}(\lambda, T)} \qquad (1.4)$$

where θ denotes the polar angle measured from the surface normal, and φ is the azimuthal angle in the surface plane. L_e is the emitted spectral radiance of the surface at temperature T and L_{bb} is the spectral radiance of a blackbody at temperature T.

The spectral radiance of a blackbody is given by Planck’s law

$$L_{bb}(\lambda, T) = \frac{2hc^2}{\lambda^5} \cdot \frac{1}{\exp\left(\frac{hc}{\lambda k_B T}\right) - 1} \qquad (1.5)$$

where h is Planck’s constant, c is the speed of light in vacuum, and k_B is Boltzmann’s constant [1].

Equation (1.4) defines emissivity as a relative quantity with respect to an ideal blackbody, while Equation (1.5) provides the spectral radiance of the blackbody used as a reference.

Emissivity generally depends on wavelength, temperature, surface condition, and observation direction. For an ideal blackbody, the directional spectral emissivity is equal to unity at all wavelengths and in all directions. In practical applications, different forms of emissivity are distinguished depending on the spectral and angular treatment. These include spectral emissivity defined at a specific wavelength, total emissivity integrated over wavelength, directional emissivity specified for a particular observation

https://doi.org/10.7795/110.20260928

direction, and hemispherical emissivity obtained by integration over all directions within the upper hemisphere.

1.2.2 Absorptivity

Absorptivity describes the fraction of incident radiation absorbed by a material. The directional spectral absorptivity is defined as the ratio of the absorbed radiant flux to the incident radiant flux

$$\alpha(\lambda, \theta, \varphi, T) = \frac{\Phi_{\text{abs}}(\lambda, \theta, \varphi, T)}{\Phi_{\text{inc}}(\lambda, \theta, \varphi, T)} \qquad (1.6)$$

where Φ_{abs} is the absorbed radiant flux at temperature T and Φ_{inc} is the incident radiant flux at temperature T. The angle θ denotes the angle of incidence measured from the surface normal, and φ is the azimuthal angle in the surface plane.

Absorptivity depends on wavelength, angle of incidence, polarization, temperature, and material properties. In general, it is both wavelength- and angle-dependent.

When radiation is incident on a material, part of it is absorbed, part is reflected, and part may be transmitted through the material. The relative contribution of these processes depends on the optical properties and thickness of the material. Radiative interactions at material interfaces are governed by energy conservation. In general form,

$$\alpha_\lambda + \rho_\lambda + \tau_\lambda = 1 \qquad (1.7)$$

where ρ_λ is the spectral reflectivity and τ_λ is the spectral transmissivity.

For many materials in the far-infrared spectral range, particularly metals, the transmissivity is negligible due to strong absorption within the material. Such materials are commonly referred to as optically opaque. For opaque materials, Equation (1.7) reduces to

$$\alpha_\lambda + \rho_\lambda = 1 \qquad (1.8)$$

This relation shows that, for opaque materials, absorptivity and reflectivity are directly linked.

A fundamental thermodynamic relation between emission and absorption is established by Kirchhoff's law. Under conditions of local thermodynamic equilibrium,

https://doi.org/10.7795/110.20260928

the directional spectral emissivity of a surface is equal to its directional spectral absorptivity [1]

$$\varepsilon(\lambda, \theta, \varphi, T) = \alpha(\lambda, \theta, \varphi, T) \qquad (1.9)$$

This relation forms the theoretical basis for indirect determination of emittance from reflectance measurements. In particular, for opaque materials in the far-infrared spectral range, absorptance can be derived from measurements of reflectance.

1.2.3 Transmissivity

Transmissivity characterizes the fraction of incident radiation that propagates through a material under specified spectral and angular conditions. The directional spectral transmissivity is defined as the ratio of transmitted radiance to incident radiance at a given wavelength and incidence direction,

$$\tau(\lambda, \theta, \varphi, T) = \frac{L_t(\lambda, \theta, \varphi, T)}{L_i(\lambda, \theta, \varphi, T)} \qquad (1.10)$$

where L_t denotes the transmitted radiance at temperature T and L_i the incident radiance at temperature T. The angular coordinates θ and φ describe the direction of incidence in spherical coordinates, with θ measured from the surface normal and φrepresenting the azimuthal angle within the surface plane.

For optically opaque materials, such as most metals in the far-infrared spectral range, transmissivity is negligible. However, for semi-transparent materials - including thin films, polymers, certain ceramics, and porous structures - transmission can contribute significantly to the overall radiative behaviour [23]. As with other radiative properties, transmissivity may be defined in spectral or total form. Corresponding experimentally determined quantities are described by transmittance, which may be specified under directional or directional–hemispherical measurement conditions depending on whether angular resolution or angular integration is considered.

In the context of integrating sphere measurements, the relevant experimentally accessible quantity is the directional–hemispherical transmittance. This quantity represents the ratio of the transmitted radiant flux integrated over the transmission hemisphere to the incident radiant flux for a specified direction of incidence. Such measurements are particularly important in FIR radiometry when characterizing materials

https://doi.org/10.7795/110.20260928

designed for thermal insulation, radiative filtering, or spectral-control applications, where the total transmitted radiant flux rather than its angular distribution is of primary interest.

1.2.4 Reflectivity

Reflectivity describes the fraction of incident radiation redirected by a surface under specified spectral and angular conditions. In general, reflectivity may also depend on temperature. For clarity, this dependence is omitted in the following expressions. In its directional spectral form, reflectivity depends on both the direction of incidence and the direction of reflection and may be represented as

$$\rho_\lambda(\theta_i, \varphi_i, \theta_r, \varphi_r) = \frac{L_r(\lambda, \theta_r, \varphi_r)}{L_i(\lambda, \theta_i, \varphi_i)} \qquad (1.11)$$

where L_i and L_r denote the incident and reflected spectral radiances, respectively. The angles θ_i, φ_i define the direction of incidence, while θ_r, φ_r specify the direction of reflection, all expressed in spherical coordinates with respect to the surface normal.

Reflectivity depends strongly on material composition, surface roughness, and surface topology, and it may exhibit pronounced wavelength and angular dependence. Accordingly, several forms are distinguished, including spectral reflectivity defined at a given wavelength, total reflectivity integrated over wavelength, directional reflectivity specified for defined angular conditions, and hemispherical reflectivity obtained by integration over the reflected hemisphere. Figure 1.1 schematically illustrates different reflection mechanisms occurring at material surfaces, including specular, anisotropic diffuse, diffuse, Lambertian, and mixed reflection. The distribution of reflected radiation depends on the surface roughness, material properties, and the ratio between characteristic surface features and the wavelength of the incident radiation.

https://doi.org/10.7795/110.20260928

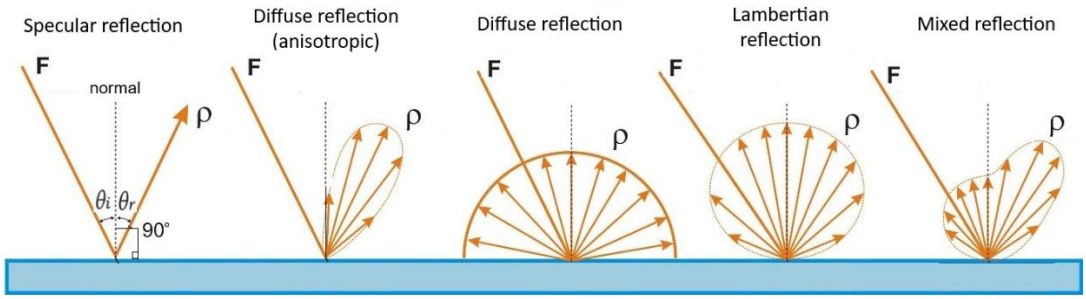


Fig. 1.1. Schematic representation of different reflection mechanisms, including specular, anisotropic diffuse, diffuse, Lambertian, and mixed reflection. This illustrates the transition from purely directional reflection to hemispherically distributed reflection, which forms the basis for the definition of directional–hemispherical reflectance. Here, F denotes the incident radiant flux, and the reflected arrows indicate the angular distribution of the reflected radiation. The dashed lines indicate the surface normal.

In radiometric measurements using integrating spheres, the experimentally accessible quantity is the directional–hemispherical reflectance, defined as the ratio of reflected radiant flux integrated over the reflection hemisphere to the incident flux for a specified direction of incidence. For thermal radiation problems and far-infrared radiometry, this quantity is often of primary relevance, since many practical applications require knowledge of the total reflected radiant flux rather than its detailed angular distribution [10].

The angular redistribution of radiation is strongly influenced by surface roughness. According to the Rayleigh criterion, a surface may be considered optically smooth if its characteristic roughness h satisfies

$$h < \frac{\lambda}{8\cos\,\theta_i} \qquad (1.12)$$

where λ is the wavelength and θ_i is the angle of incidence [1, 16]. At far-infrared wavelengths, surfaces that appear optically rough in the visible spectral range may behave as optically smooth surfaces, resulting in predominantly specular reflection. Conversely, structured surfaces with characteristic dimensions comparable to the wavelength can enhance diffuse scattering. This wavelength-dependent behaviour highlights the need for specifically engineered surface topologies in FIR optical design.

Figure 1.2 illustrates the transition from specular to diffuse reflection as a function of surface roughness. For optically smooth surfaces, reflection is predominantly

https://doi.org/10.7795/110.20260928

specular, with the angle of reflection equal to the angle of incidence. In contrast, rough surfaces lead to diffuse scattering, where radiation is redistributed over a wide range of angles.

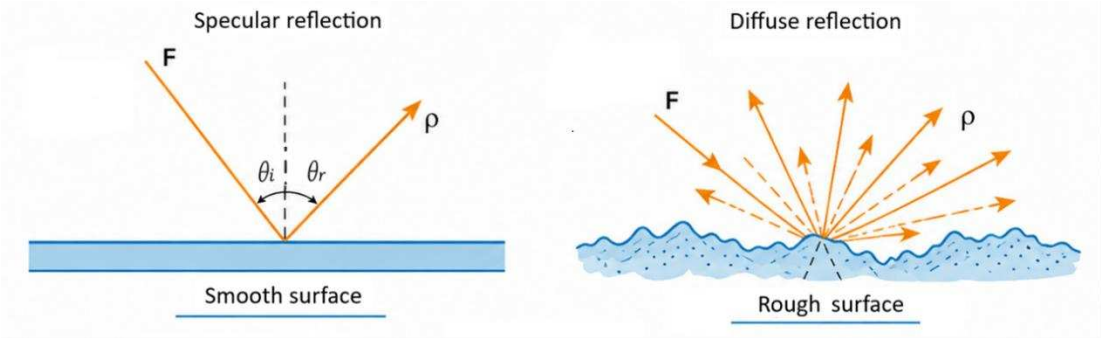


Fig. 1.2. Schematic representation of radiation reflection from surfaces with different roughness characteristics: specular reflection from an optically smooth surface (left) and diffuse reflection from a rough surface (right). The angles of incidence θ_i and reflection θ_r are defined with respect to the surface normal. The distribution of reflected radiation depends on the surface roughness relative to the wavelength.

Most real surfaces exhibit a combination of specular and diffuse reflection. This behaviour is quantitatively described by the bidirectional reflectance distribution function (BRDF), which relates the reflected radiance in a given direction to the incident irradiance as a function of both incoming and outgoing angles [11]. In the ideal case of a perfectly diffuse, or Lambertian, surface, the reflected radiance is direction-independent [1].

Lambert's cosine law does not describe an angular dependence of radiance itself, but the angular dependence of the reflected radiant intensity, which results from the projected surface area. Thus, the reflected radiant intensity decreases with increasing reflection angle according to

$$I_r(\theta_r) = I_r(0)\cos\,\theta_r \qquad (1.13)$$

where $I_r(\theta_r)$ is the reflected radiant intensity at the reflection angle θ_r, and $I_r(0)$ is the reflected radiant intensity in the surface-normal direction. Although the radiant intensity decreases with angle, the radiance of an ideal Lambertian surface remains constant with direction. This is why such a surface appears equally bright when observed from different directions.

https://doi.org/10.7795/110.20260928

For an ideal Lambertian reflector, the BRDF is constant and is given by

$$\mathrm{BRDF} = \frac{\rho_\lambda}{\pi} \qquad (1.14)$$

Equation (1.14) follows from the definition of the BRDF together with the assumption of direction-independent reflected radiance. It indicates that, for an ideal Lambertian surface, the reflected radiance is constant over the hemisphere, while the angular dependence of the emitted or reflected intensity is governed by the cosine projection factor.

Under these idealized conditions, directional and hemispherical reflectance become identical, which greatly simplifies radiative transfer calculations. In practical FIR systems, however, deviations from ideal Lambertian behaviour must be considered. The design of integrating spheres for the far-infrared therefore requires careful control of surface topology in order to approximate diffuse scattering conditions and ensure reliable measurement of directional–hemispherical reflectance.

1.2.5 Conservation of energy in radiative interactions

Radiative interactions at material interfaces are governed by the principle of energy conservation. For any surface exposed to incident radiation, the incoming radiant energy must be redistributed through reflection, absorption, and transmission, as expressed by Eq. (1.7). The specific form of this relation depends on whether the quantities are defined spectrally, directionally, or hemispherically; however, the conservation principle remains universally valid.

In the far-infrared spectral range, many materials of practical relevance, particularly metals and coated metallic structures, can be treated as optically opaque. Under these conditions, transmissivity is negligible and the energy balance simplifies to Eq. (1.8). In terms of intrinsic material properties, this relation links absorptivity and reflectivity. In terms of experimentally determined radiometric quantities, the corresponding relation links absorptance and reflectance under the specified measurement geometry.

A further fundamental relation is provided by Kirchhoff’s law. Under conditions of local thermodynamic equilibrium, directional spectral emissivity is equal to

https://doi.org/10.7795/110.20260928

directional spectral absorptivity, as given by Eq. (1.9). For opaque materials, this relation establishes a direct link between emissivity and reflectivity:

$$\varepsilon_\lambda = 1 - \rho_\lambda \qquad (1.15)$$

where ε_λ denotes the directional spectral emissivity and ρ_λ denotes the corresponding spectral reflectivity, understood as the hemispherically integrated reflected fraction for the specified direction of incidence at wavelength λ.

For experimentally determined quantities, the analogous relation can be applied under the same opaque-material assumption and defined measurement geometry. In this work, the relevant measured quantity is the directional–hemispherical reflectance, because the integrating sphere collects the reflected radiant flux over the hemisphere for a defined direction of incidence. Accordingly, for opaque samples, emittance-related quantities can be related to the measured directional–hemispherical reflectance under the corresponding geometrical conditions.

This distinction is important for the terminology used throughout this work. Reflectivity, transmissivity, absorptivity, and emissivity refer to intrinsic material properties, whereas reflectance, transmittance, absorptance, and emittance refer to radiometric quantities defined by a specific sample and measurement geometry. Consequently, the quantities measured with the integrating sphere are referred to as directional–hemispherical reflectance and transmittance.

The combined application of energy conservation and Kirchhoff's law therefore provides the radiometric basis for interpreting integrating-sphere measurements of opaque samples in the far-infrared spectral range. This interdependence underpins the measurement strategy adopted in the present work and is relevant for FIR applications in infrared thermography, FTIR spectroscopy, remote sensing, and thermal modelling of spacecraft systems [1, 10, 24].

1.3 Methods of Measuring Radiation in the FIR Range

Radiometric measurements in the FIR spectral range are subject to several intrinsic limitations, including low photon energies, strong thermal background radiation, atmospheric absorption - particularly due to water vapour - and reduced detector sensitivity at long wavelengths [1, 25, 26]. These factors impose strict requirements on environmental control, optical throughput, and detection principles. In contrast to

https://doi.org/10.7795/110.20260928

shorter wavelengths, where photon-based detectors dominate, FIR measurements rely primarily on thermal detection mechanisms, which respond to absorbed radiant energy rather than to individual photons.

In the present work, spectral measurements in the range from 25 µm to 100 µm were carried out using an FTIR spectrometer (Bruker VERTEX 80v), operated under dry-air purging conditions in order to suppress atmospheric absorption while ensuring compatibility with the externally coupled integrating sphere system. The primary radiometric quantities investigated are directional–hemispherical reflectance and transmittance. These quantities are obtained by combining interferometric spectral analysis with hemispherical collection of reflected or transmitted radiation inside the integrating sphere, thereby forming a unified radiometric measurement system [9, 27, 28].

1.3.1 Detector technologies used in this work

In this dissertation, far-infrared radiation was detected using thermal detectors operated in two distinct optical configurations within the measurement system. A cryogenic bolometer was connected in the standard internal detector position of the spectrometer, representing the conventional FTIR detection scheme. Bolometers operate by converting absorbed radiation into heat, leading to a temperature-dependent resistance change in the sensing element. When operated at cryogenic temperatures, thermal noise is significantly reduced, providing high sensitivity at long wavelengths [25, 26]. In this configuration, the radiation returning from the integrating sphere is guided back through the interferometer optics and detected by the internal bolometric system.

In addition to the bolometric configuration, a far-infrared-optimized deuterated triglycine sulfate (FDTGS) detector was positioned directly at the integrating sphere detector port. DTGS detectors operate at room temperature and provide a broadband spectral response without the need for cryogenic cooling [3]. By locating the detector in close proximity to the sphere, hemispherically collected radiation can be detected without additional propagation through the interferometer return optics.

The two detector arrangements therefore represent different radiometric coupling strategies within the same optical measurement system and are treated as part of the overall optical configuration rather than as separate experimental methodologies.

https://doi.org/10.7795/110.20260928

1.3.2 Fourier Transform Infrared spectroscopy in the FIR

FIR measurements in this work were performed using FTIR spectroscopy. The Bruker VERTEX 80v spectrometer enables measurements in the spectral region from 25 µm to 100 µm and was operated under dry-air purging conditions in order to minimize atmospheric absorption effects, which become increasingly significant at long wavelengths.

FTIR spectroscopy is based on interferometric measurement of broadband radiation using a Michelson interferometer (Fig. 1.3). The incident radiation is divided into two beams by a beamsplitter, reflected from a fixed and a moving mirror, and subsequently recombined. The resulting interference signal, recorded as a function of optical path difference, forms an interferogram containing spectral information over the complete investigated wavelength range. The variation of the optical path difference introduced by the movable mirror leads to constructive and destructive interference of the recombined beams, which is detected as an interferogram.

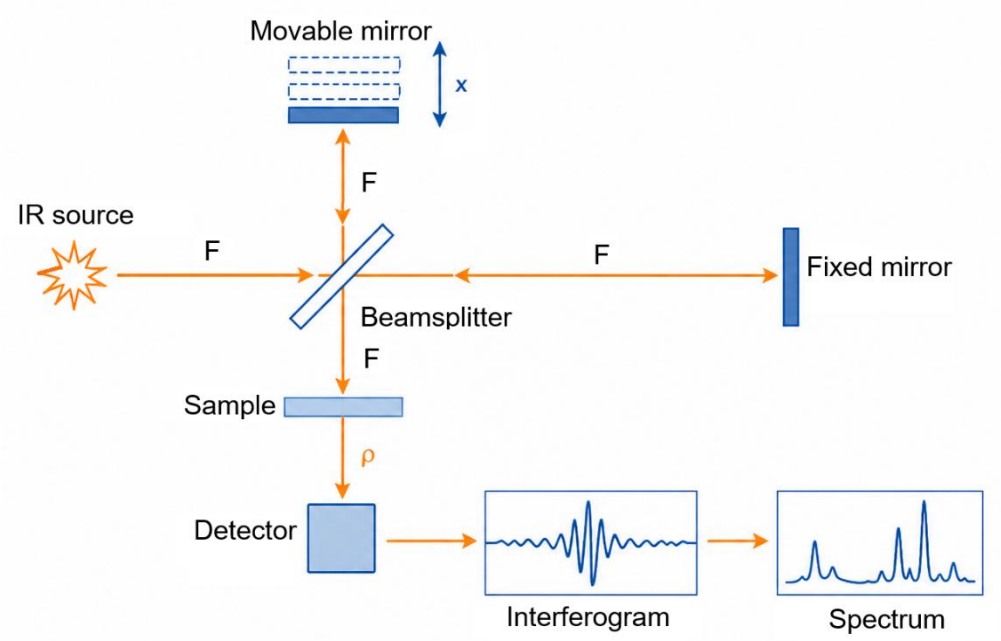


Fig. 1.3. Schematic representation of a FTIR spectrometer. The incident radiation is divided by a beamsplitter into two paths, reflected by a fixed and a movable mirror, and subsequently recombined to produce an interference signal (interferogram). The detected interferogram is Fourier-transformed to obtain the spectral distribution of the radiation.

https://doi.org/10.7795/110.20260928

The spectral intensity $S(\tilde{\nu})$ is obtained by Fourier transformation of the interferogram $I(x)$

$$S(\tilde{\nu}) = \int_{-\infty}^{\infty} I(x)\, e^{-2\pi i \tilde{\nu} x}\, dx \qquad (1.16)$$

where x is the optical path difference and $\tilde{\nu}$ is the wavenumber [27, 28].

The interferometric approach allows simultaneous acquisition of all spectral components (Fellgett advantage), precise wavelength calibration determined by the reference laser (Connes advantage), and high optical throughput due to the absence of entrance slits (Jacquinot advantage) [27, 28].

In the context of this dissertation, the FTIR spectrometer provides spectral discrimination, while angular integration of reflected or transmitted radiation is performed by the integrating sphere. The interferometer therefore defines the spectral resolution and wavelength accuracy of the measurement, whereas the sphere determines the radiometric geometry. The combination of the interferometer and integrating sphere enables broadband characterization of directional–hemispherical reflectance and transmittance in the far-infrared range.

1.3.3 Integrating sphere–based FTIR measurements

For the characterization of scattering and thermally emitting materials in the far-infrared range, the FTIR spectrometer was externally coupled to the developed integrating sphere. A schematic representation of the optical coupling between the FTIR spectrometer and the integrating sphere is shown in Fig. 1.4, while the detailed optical implementation is discussed in Chapter 4. In this configuration, the sample is illuminated under a defined direction of incidence, while the integrating sphere collects radiation reflected or transmitted by the sample over the reflection or transmission hemisphere. The measurable quantities therefore correspond to directional–hemispherical reflectance and transmittance.

Inside the integrating sphere, radiation undergoes multiple reflections at the structured inner surface. The design and radiometric properties of the integrating sphere are described in detail in Chapter 3. Provided that the sphere geometry, port configuration, and surface scattering properties are properly designed, this multiple-reflection process results in angular redistribution of the radiation and enables hemispherical

https://doi.org/10.7795/110.20260928

integration of the reflected or transmitted flux. The detected signal is thus proportional to the total radiant flux leaving the sample into the respective hemisphere, rather than to a specific scattering direction.

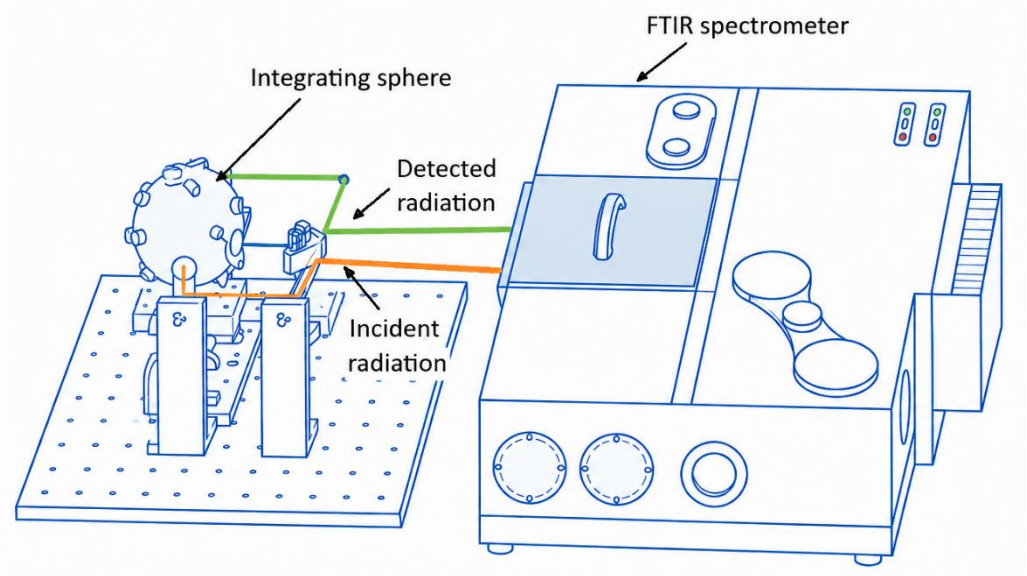


Fig. 1.4. Schematic representation of the integrating sphere-based FTIR measurement configuration. The radiation emerging from the spectrometer is externally coupled to the integrating sphere, where the sample is illuminated under defined incidence conditions. The reflected or transmitted radiation is collected over the corresponding hemisphere within the sphere and directed toward the detector, enabling spectral determination of directional–hemispherical reflectance and transmittance in the far-infrared range.

Measurements were performed by sequentially recording interferograms corresponding to defined radiometric states of the system, including reference measurements using a reference surface and measurements with the sample in place. Spectral directional–hemispherical reflectance and transmittance were obtained from ratios of the detected signals under identical optical alignment and detector configuration. This procedure eliminates instrumental transfer functions and isolates the sample-dependent radiometric response. The measurement procedure and data evaluation are presented in detail in Chapter 5.

The integration of interferometric spectral analysis with hemispherical flux collection constitutes the experimental basis of the measurement methodology developed in this dissertation and described in detail in the subsequent chapters. The integrating sphere does not merely serve as an accessory component, but defines the angular

https://doi.org/10.7795/110.20260928

measurement geometry required for determination of directional–hemispherical quantities in the 25 μm to 100 μm spectral range.

1.4 Integrating Sphere Theory

Integrating spheres are fundamental optical instruments used in radiometry and optical metrology for measurement of directional–hemispherical reflectance and transmittance of materials. Their primary function is the spatial averaging of radiation scattered by a sample, enabling measurements that are largely independent of the angular distribution of reflected or transmitted radiation. This makes integrating spheres essential for the characterization of optically rough, diffusely scattering, and semi-transparent materials.

Integrating spheres are widely used in UV-Vis-NIR spectroscopy, radiometric calibration, remote sensing, and detector characterization [29]. However, their application in the FIR region remains limited due to material, thermal, and geometrical constraints. Understanding the theoretical foundations of integrating spheres is therefore essential for adapting this concept to FIR measurements.

1.4.1 Physical principle of integrating sphere operation

An integrating sphere is a hollow spherical cavity with an inner surface designed to provide diffuse reflection characteristics (Fig. 1.5). Radiation entering the sphere undergoes multiple reflections at the inner surface, leading to angular redistribution and a nearly uniform radiance distribution inside the cavity. A detector positioned at one of the ports measures this spatially averaged radiance. Figure 1.5 illustrates the redistribution of radiation inside the integrating sphere. Radiation entering through the input port undergoes multiple reflections within the cavity, resulting in hemispherical integration of the reflected radiation.

The fundamental advantage of an integrating sphere is the ability to collect both specular and diffuse radiation components and integrate them over a hemisphere, enabling measurements that are largely independent of the angular distribution of the scattered radiation [13, 14]. The operation of the sphere is based on the idealized assumption of Lambertian reflection of the internal surface, where the radiance is independent of observation direction.

https://doi.org/10.7795/110.20260928

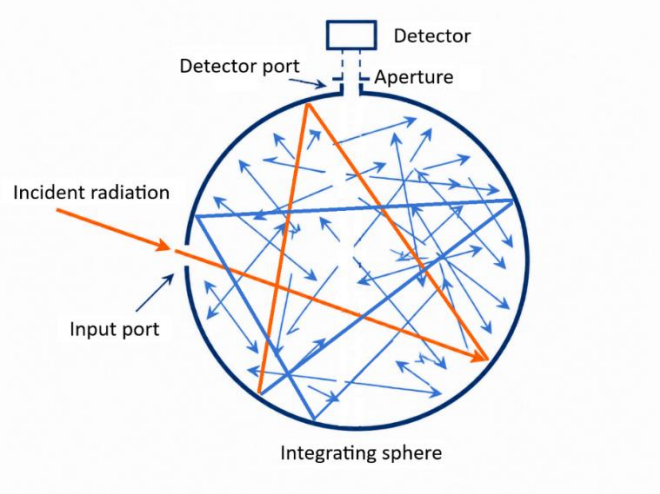


Fig. 1.5. Schematic representation of radiation redistribution in an integrating sphere. The incident radiation enters through the input port and undergoes an initial reflection at the sphere wall or sample surface. Subsequent multiple reflections redistribute the radiation within the sphere cavity, and a fraction of this radiation is collected through the detector port aperture and directed to the detector.

1.4.2 Geometrical and optical parameters

The radiometric performance of an integrating sphere is determined by the interplay between its geometry and the optical properties of the internal surface. These parameters do not act independently; rather, they collectively define the degree of radiance uniformity, optical throughput, and radiometric sensitivity.

The sphere diameter D defines the internal cavity volume and thus influences both spatial averaging and signal level. Larger spheres improve radiance uniformity due to increased path length and a greater number of reflections before detection. However, this also reduces the irradiance reaching the detector, since radiant flux is distributed over a larger internal surface area. The internal surface area of a sphere is given by

$$A_{sphere} = 4\pi \left(\frac{D}{2}\right)^2 \qquad (1.17)$$

where A_{sphere} is the internal surface area of the sphere, D is the sphere diameter, and π is the constant pi.

The reflectivity ρ of the internal surface is of central importance. High reflectivity, typically exceeding 0.95 in conventional integrating spheres, ensures that

https://doi.org/10.7795/110.20260928

radiation undergoes multiple reflections before absorption. Each reflection contributes to spatial redistribution of energy, promoting radiance homogenization within the cavity. A decrease in reflectivity reduces the number of effective reflections and directly impacts the radiometric gain of the sphere.

Another important parameter is the port configuration. Openings are required for illumination, sample placement, and detector coupling, yet each port introduces losses and disturbs the ideal spherical symmetry. The cumulative effect of these openings is quantified by the port fraction

$$f = \frac{A_{\text{ports}}}{A_{sphere}} \qquad (1.18)$$

where A_{ports} is the total area of all ports and A_{sphere} is the internal surface area of the sphere. Increasing port fraction leads to reduced uniformity and decreased internal radiance amplification. Consequently, sphere design involves a compromise between functional accessibility and radiometric performance.

Additional geometric elements, such as baffles and knife-edge ports, are introduced to suppress direct illumination of the detector and minimize stray radiation. While these elements improve measurement fidelity, they also modify internal radiative transfer and must therefore be considered within the overall optical model [13, 14].

1.4.3 Sphere multiplier and radiative transfer

A defining feature of integrating spheres is the radiometric amplification resulting from multiple internal reflections. After each reflection, a fraction ρ of the radiation remains within the cavity, while a fraction is absorbed or lost through ports. The cumulative effect of this recursive process is described by the sphere multiplier M,

$$M = \frac{1}{1 - \rho(1 - f)} \qquad (1.19)$$

where ρ represents the effective reflectivity of the internal surface and f is the port fraction.

The sphere multiplier quantifies the enhancement of irradiance within the cavity relative to the initial incident flux and is therefore fundamental to interpreting detector

https://doi.org/10.7795/110.20260928

signals in reflectance and transmittance measurements [13]. The radiant flux reaching the detector can be expressed as

$$\Phi_D = M \cdot \Phi_{\text{sample}} \cdot T_{SD} \qquad (1.20)$$

where Φ_D is the radiant flux at the detector, Φ_{sample} is the radiant flux interacting with the sample, and T_{SD} represents the transfer coefficient between the sample and detector ports.

In practical systems, internal radiative transfer deviates from the idealized Lambertian assumption due to finite reflectivity, non-uniform surface properties, and geometric perturbations introduced by ports and baffles. For this reason, Monte Carlo ray-tracing simulations are often employed to model realistic sphere behaviour and to quantify deviations from ideal radiance uniformity.

1.4.4 Applications in optical metrology

Integrating spheres are widely established in optical metrology as tools for determination of directional–hemispherical reflectance and transmittance, detector calibration, radiometric standard realization, and material characterization [30, 31]. Their primary advantage lies in reducing angular dependence and enabling reproducible measurements independent of detailed scattering distributions.

In conventional UV-Vis-NIR applications, integrating spheres are routinely coupled to spectrophotometers and FTIR systems, providing reliable angle-integrated radiometric data. The success of these implementations relies on the availability of highly diffuse coatings and the validity of geometric optics assumptions. However, these conditions are no longer fully satisfied in the far-infrared spectral range, which leads to significant limitations of conventional integrating sphere concepts.

1.4.5 Limitations of conventional integrating spheres in the FIR

Despite their widespread use at shorter wavelengths, conventional integrating sphere concepts encounter significant limitations in the far-infrared region. These limitations arise from both material and physical constraints.

A primary challenge is the lack of suitable diffusely reflecting materials. Coatings commonly employed in UV–Vis–NIR spheres, such as PTFE-based materials or $BaSO_4$, exhibit strong absorption and reduced reflectivity beyond the mid-infrared

https://doi.org/10.7795/110.20260928

range. In contrast, metallic surfaces such as gold or aluminium provide high reflectivity at long wavelengths but exhibit predominantly specular behaviour, violating the Lambertian assumption underlying classical integrating sphere theory [2].

Thermal self-emission represents an additional complication. At these wavelengths, thermal radiation emitted by the sphere walls can become comparable to the reflected signal. This introduces systematic offsets and necessitates careful background correction or temperature stabilization [1].

Furthermore, detector sensitivity decreases at longer wavelengths, and multiple internal reflections increase the effective optical path length, which may reduce the signal-to-noise ratio. Diffraction and wave-optical effects also become significant when wavelengths approach port dimensions or characteristic surface structures, leading to deviations from purely geometric optics behaviour [32].

These limitations necessitate the development of modified integrating sphere concepts specifically adapted to this spectral range.

1.4.6 Need for new integrating sphere concepts for FIR

The combined influence of material absorption, specular metallic reflection, thermal self-emission, detector limitations, and wave-optical effects explains why integrating sphere designs developed for shorter wavelengths cannot be directly transferred to the far-infrared region.

Reliable FIR measurements require surface topologies capable of approximating Lambertian behaviour at long wavelengths, while maintaining high reflectivity and low absorptivity. At the same time, geometrical parameters must be optimized to limit port losses, reduce thermal background contributions, and ensure compatibility with sensitive FIR detection systems.

These constraints motivate the development of new integrating sphere concepts specifically optimized for the 25 µm to 100 µm spectral range. The research presented in this dissertation addresses these challenges through the design of structured surfaces, tailored geometries, and dedicated optical coupling strategies for FIR radiometry. The development of such solutions is addressed in the following chapter.

https://doi.org/10.7795/110.20260928

Chapter 2. Development of Diffuse-Scattering Surfaces for the Far-Infrared Range

This chapter addresses the absence of suitable diffuse-scattering reflectors for wavelengths above approximately 25 μm, as identified in Chapter 1, and presents the development of a structured surface capable of producing broadband angular redistribution of radiation in the far-infrared spectral range.

Two surface concepts are investigated: structures composed of randomly distributed spherical elements and surfaces generated from randomized harmonic function (RHFS). The chapter describes their mathematical modelling, optical analysis using ray-tracing techniques, fabrication of physical samples, and experimental characterization in the terahertz range.

The comparative analysis of experimental and simulated results leads to the identification of an RHFS-type topology as a reproducible and optically suitable surface concept for use as the internal reflective surface of a far-infrared integrating sphere.

2.1 Physical Principles of Diffuse Reflection in the Far-Infrared

The far-infrared spectral region, typically spanning wavelengths from approximately 25 μm to 1000 μm, plays a crucial role in thermal radiation studies, astronomical instrumentation, remote sensing, and spectroscopic characterization of materials. Optical components operating in this range must provide controlled propagation and redistribution of radiation, particularly in measurement systems requiring angular averaging, such as Fourier-transform spectrometers and integrating spheres.

A central challenge in FIR optical engineering is the development of surfaces capable of producing stable broadband angular redistribution of reflected radiation. Unlike the visible and near-infrared ranges, where established coatings exhibit scattering behaviour approaching Lambertian characteristics, the FIR region is characterized by fundamentally different scattering mechanisms governed by long wavelengths, increased material absorption, and reduced scattering efficiency of conventional rough surfaces.

https://doi.org/10.7795/110.20260928

Diffuse reflection occurs when incident radiation is scattered over a wide angular range rather than reflected in a single specular direction. In the FIR regime, this process is governed primarily by surface geometry, while material properties play a secondary but still significant role. Effective scattering is achieved when characteristic surface features are comparable to, or larger than, the wavelength of the incident radiation [16, 17, 33].

Several physical limitations hinder the realization of diffuse FIR reflectors. First, FIR wavelengths extend from tens to hundreds of micrometres; therefore, surface structures capable of efficient scattering must be of comparable dimensions. Second, many polymers and dielectric coatings exhibit strong photon absorption in the FIR, significantly reducing reflectivity [2]. Third, surfaces that appear optically rough in the visible often become effectively smooth in the FIR, resulting in dominant specular reflection rather than diffuse scattering [16, 17, 18].

Consequently, conventional diffuse coatings such as PTFE-based materials, white paints, or oxide layers lose their Lambertian character in the far-infrared and instead behave either as absorbers or partially specular reflectors. This effect becomes particularly critical for wavelengths above approximately 25 μm, where material absorption and insufficient structural roughness significantly limit the efficiency of diffuse scattering.

The radiative behaviour of rough surfaces and the transition between specular and diffuse reflection are commonly described using statistical scattering theory and the bidirectional reflectance distribution function (BRDF) formalism [11, 19, 34, 35, 36]. In the FIR, these mechanisms are strongly influenced by the relationship between wavelength and surface topology, as well as by the electromagnetic properties of the reflecting material [1].

To approximate Lambertian behaviour in the FIR spectral region, a reflecting surface must satisfy several conditions:

- provide diffuse scattering over a broad range of incident and reflection angles;
- suppress specular reflection components;
- maintain high reflectivity across the target FIR wavelength range;

https://doi.org/10.7795/110.20260928

- possess structural features with characteristic dimensions comparable to the operating wavelength.

These requirements can be addressed through the engineering of micro- and millimetre-scale surface topologies specifically designed for long-wavelength radiation. Structured metallic or coated surfaces, porous geometries, and randomized relief patterns can promote multiple internal reflections and thereby enhance angular redistribution of radiation, resulting in diffuse-like scattering behaviour.

Randomization of the surface topology plays a critical role in suppressing coherent reflection effects. Periodic structures tend to produce diffraction phenomena and directional scattering lobes, whereas stochastic geometries enable broadband angular redistribution of radiation and reduce the contribution of specular reflection [16, 33].

Recent advances in additive manufacturing and micro-structuring technologies enable the fabrication of tailored surface geometries with controlled roughness and reproducible topology at sub-millimetre scales. These developments create new opportunities for designing diffuse-scattering surfaces specifically optimized for the far-infrared spectral range.

Within this framework, the present work focuses on the development of engineered surface topologies intended for use as internal diffuse-scattering reflectors in far-infrared integrating spheres. Two conceptually different approaches are investigated: surfaces composed of randomly distributed spherical scatterers and surfaces generated from randomized harmonic functions (RHFS). These concepts are analysed using numerical modelling, ray-tracing simulations, fabrication of physical samples, and experimental validation in the terahertz spectral range.

2.2 Surface Concepts for FIR Diffuse Reflection

The realization of diffuse reflection in the far-infrared requires surface topologies specifically engineered for long-wavelength radiation. Conventional rough surfaces designed for visible or near-infrared applications are insufficient in the FIR, where scattering efficiency depends strongly on the relation between wavelength and characteristic feature size. As a result, dedicated geometrical concepts must be developed to promote broadband angular redistribution of radiation while maintaining high reflectivity.

https://doi.org/10.7795/110.20260928

To enable directional–hemispherical reflectance and transmittance measurements in the far-infrared, a surface intended for use as an internal diffuser must redistribute incident radiation over a wide angular range while maintaining high overall reflectivity [33, 34]. As established in Section 2.1, diffuse scattering in the FIR is governed primarily by surface topology at the wavelength scale, whereas material absorption and coating losses impose additional constraints.

Based on these considerations, this work investigates two engineered surface topology concepts designed for long-wavelength diffuse reflection behaviour: Random Ball Surfaces (Section 2.2.1) and Random Harmonic Function Surfaces (Section 2.2.2). Both concepts are generated parametrically, enabling systematic variation of feature size and roughness, followed by optical evaluation using ray-tracing techniques and experimental validation.

2.2.1 Random Ball Surfaces (RBS)

The first concept is based on randomly distributed spherical scatterers placed on a planar substrate. The underlying idea is that convex micro-geometries with characteristic sizes comparable to FIR wavelengths can act as efficient scattering elements. Random placement is used deliberately to suppress periodicity-related diffraction artefacts and to promote broadband angular redistribution of reflected radiation [33].

In this work, spherical elements are treated as primary geometrical scatterers, while the gaps between neighbouring spheres form small cavities that can increase the number of internal reflections before radiation exits the surface. Such multi-bounce behaviour is expected to broaden the angular distribution of the reflected signal and reduce the dominance of a single specular direction.

Since the FIR wavelength range of interest for the subsequent integrating sphere design is 25 µm to 100 µm, the characteristic dimensions of the surface features were selected to be comparable to, or larger than, the wavelength. As a practical design assumption, sphere radii in the range of 0.1 mm to 0.8 mm were considered suitable for producing significant geometric scattering in the far-infrared. These values were used as starting parameters for numerical exploration rather than as experimentally verified optima.

https://doi.org/10.7795/110.20260928

To minimize absorption and ensure high reflectivity at long wavelengths, the concept assumes the use of a reflective metallic surface. In the present work, the fabricated RBS samples are made of aluminium, which exhibits high reflectivity in the far-infrared spectral range. The role of the material is primarily to provide high reflectivity, whereas the scattering behaviour is governed predominantly by the surface topology. Metallic materials such as aluminium exhibit favourable radiometric properties in the FIR and ensure stable reflectivity characteristics [2].

Random Ball Surfaces were generated using Wolfram Mathematica by constructing a parametric 3D geometry consisting of:

- a planar base surface;
- a set of spheres with randomly assigned radii within a defined interval;
- random 2D positions for sphere centres within a defined surface area;
- optional overlap constraints or packing rules, depending on the desired surface coverage.

The following Mathematica routine illustrates the basic procedure used to generate the RBS geometry. The parameters $r_{\min}$ and $r_{\max}$ define the minimum and maximum radii of the spherical scatterers, while $n$specifies the number of spheres placed on the substrate. The command RandomReal[{0, 25}, {N, 2}] generates random two-dimensional coordinates for the sphere centres within a square surface area of 25 mm × 25 mm. Thus, each realization consists of $n$spheres with randomly assigned radii between 0.1 mm and 0.8 mm and randomly distributed centre positions on the planar base surface.

An example of the generation procedure is given below:

```
rmin = 0.1; rmax = 0.8; N = 200;

centers = RandomReal[{0, 25}, {N, 2}];

radii = RandomReal[{rmin, rmax}, N];

balls = Table[

Sphere[{centers[[i, 1]], centers[[i, 2]], radii[[i]]}, radii[[i]]], {i, 1,
N}];
```

The generated spheres are then combined into a surface model, which can be exported as a three-dimensional mesh for optical simulation and fabrication. By

https://doi.org/10.7795/110.20260928

changing the number of spheres N, the surface coverage and density of scattering elements can be varied systematically (Fig. 2.1).

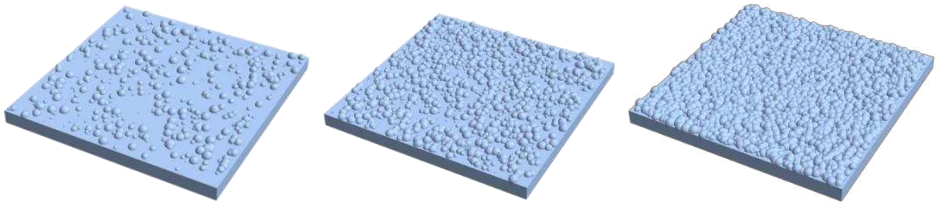


Fig. 2.1. Examples of RBS geometries generated with different numbers (N) of randomly distributed spherical scatterers on a 25 mm × 25 mm planar substrate. Increasing the number of spheres increases the surface coverage and density of scattering elements, while the individual sphere radii are randomly selected between 0.1 mm and 0.8 mm.

This numerical approach enabled the creation of a large number of statistically different RBS realizations, which were subsequently evaluated using ray-tracing techniques (Section 2.3) and, later, assessed experimentally for manufacturability and reproducibility (Section 2.6).

2.2.2 Random Harmonic Function Surfaces (RHFS)

The second concept employs surfaces generated from randomized harmonic components. Harmonic-based surface descriptions provide smooth and continuous relief structures and enable explicit parametric control of surface topology. By introducing random amplitudes, phases, and spatial frequencies, the resulting surfaces acquire controlled stochastic roughness across multiple spatial scales.

A general representation used in this work is a random superposition of sinusoidal components:

$$h_{RHFS}(x,y) = \sum_{n=1}^{N} a_n \sin^4(k_n x + \varphi_n) \sin^4(k_n y + \phi_n) \qquad (2.1)$$

where a_n are amplitudes controlling roughness magnitude, k_n are spatial frequencies controlling feature periods, and φ_n, ϕ_n are random phases. The use of the fourth power of the sine function ensures smooth peak-like features and suppresses sharp discontinuities in the surface profile.

The central motivation for introducing Random Harmonic Function Surfaces (RHFS) lies in the explicit parametric control of surface statistics. Unlike purely

https://doi.org/10.7795/110.20260928

stochastic roughness models, the RHFS approach allows the geometrical characteristics of the surface to be defined through a limited set of mathematically well-defined parameters. This parametric structure enables systematic tuning of the characteristic feature size by adjusting spatial frequency (interval) parameters, while the distribution of surface slopes and the sharpness of the relief can be modified through the choice of a shaping kernel. Once these parameters are specified, the resulting surface topology becomes fully deterministic, ensuring reproducible surface generation and compatibility with subsequent fabrication steps.

Such controllability is of particular importance for integrating sphere development in the far-infrared. The internal diffuser must not only approximate quasi-Lambertian scattering behaviour at long wavelengths, but also remain manufacturable as a segmented structure suitable for coating. A purely random or empirically roughened surface would not guarantee reproducibility across multiple sphere segments, whereas the RHFS concept ensures that identical parameter sets yield identical geometries.

In the present work, RHFS surfaces were generated by combining two complementary components. The first component consists of a randomized sinusoidal base field, introducing controlled stochastic roughness through randomly distributed phase arguments. The second component is a deterministic shaping kernel based on a $\sin^4(x)\sin^4(y)$function, consistent with the functional form used in Equation (2.1), which governs the geometry of local protrusions and defines the characteristic relief profile. These two components are mathematically combined using a discrete convolution operation, resulting in a randomized yet fully parameter-controlled surface topology. This construction provides a tunable and reproducible relief structure suitable for FIR scattering applications. The two input components of the generation process are illustrated in Fig. 2.2: the randomized base field in Fig. 2.2(a) and the deterministic shaping kernel in Fig. 2.2(b). Their discrete convolution produces the resulting RHFS surface topologies shown in Fig. 2.3, where the intervals parameter controls the spatial density of the randomized base field and therefore the characteristic feature density of the generated surface.

The following Mathematica routine illustrates the generation of the RHFS topology. The array data2D represents the randomized base field. Its discretization is controlled by the parameter intervals, which defines the sampling step π/intervals. Increasing this parameter increases the density of spatial variations in the base field and

https://doi.org/10.7795/110.20260928

therefore produces a finer surface topology. The array kernel2D represents the deterministic shaping kernel, defined by a $\sin^4(x)\sin^4(y)$ function. In this work, the kernel size was kept constant (intervalskernel = 100), while the intervals parameter was varied. The final surface was obtained by discrete convolution of the randomized base field with the shaping kernel using ListConvolve.

An example of the generation procedure is given below:

```
intervals = 800;

data2D = Table[Sin[RandomReal[]*X] Sin[RandomReal[]*Y], {X, 6Pi, 7Pi, Pi/in-
tervals}, {Y, 6Pi, 7Pi, Pi/intervals}];

intervalskernel = 100;

kernel2D = Table[0.5*Sin[X]^4*Sin[Y]^4, {X, 0, Pi, Pi/intervalskernel}, {Y,
0, Pi, Pi/intervalskernel}];

surface = ListConvolve[kernel2D, data2D];
```

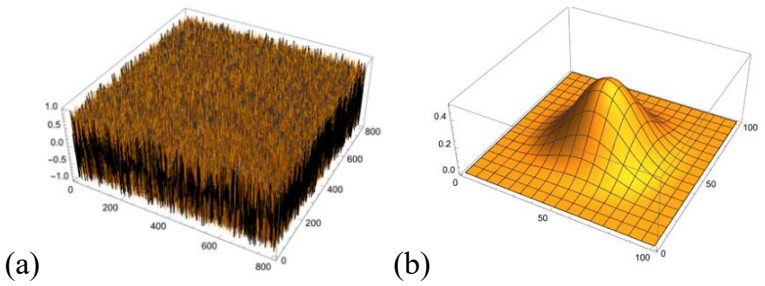


Fig. 2.2. Components used for RHFS generation: (a) randomized base field (data2D), whose spatial density is controlled by the parameter intervals, and (b) deterministic shaping kernel (kernel2D) based on a $\sin^4(x)\sin^4(y)$ function.

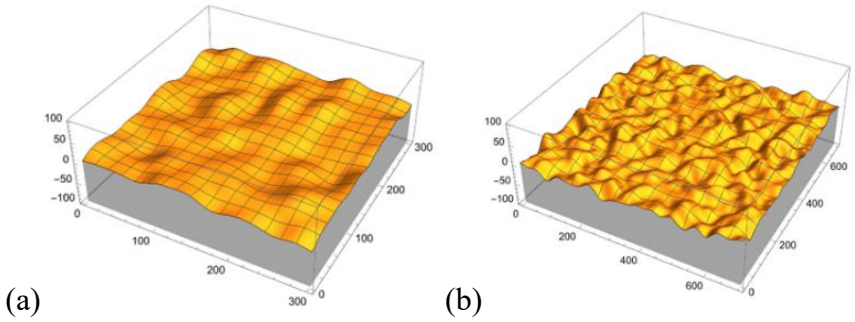


Fig. 2.3. Random harmonic function surfaces obtained by discrete convolution of the randomized base field shown in Fig. 2.2(a) with the deterministic shaping kernel shown in Fig. 2.2(b): (a) intervals = 400, RHFS-400 and (b) intervals = 800, RHFS-800. Increasing the intervals parameter increases the spatial density of the randomized base field, resulting in a finer and more densely structured surface topology.

https://doi.org/10.7795/110.20260928

By varying the intervals parameter, e.g., 200, 400, and 800, RHFS surfaces with increasing spatial feature density and a reduced characteristic period were generated. These RHFS designs were then exported for ray-tracing analysis and fabrication.

Both RBS and RHFS provide parametric, reproducible surface descriptions suitable for numerical study. In the next section, their optical performance is evaluated using non-sequential ray tracing in Zemax, where the angular distribution of reflected radiation is used as the primary metric for diffuser suitability.

2.3 Ray Tracing in Diffuse Surface Analysis Using Zemax

The evaluation of diffuse reflection behaviour in the far-infrared cannot rely solely on analytical models. Due to the complex interaction between long-wavelength radiation and structured surfaces, numerical optical simulation becomes a critical stage in the design process. Ray tracing provides a physically consistent framework for predicting the angular distribution of reflected radiation and for assessing the suitability of candidate surface geometries for integrating sphere applications.

Ray tracing is a computational method that models the propagation of electromagnetic radiation through optical systems using geometrical optics approximations. It enables simulation of reflection, scattering, absorption, and transmission processes for complex three-dimensional geometries. This method is particularly effective for FIR structures where the dominant effects arise from macroscopic geometry and multiple reflections rather than interference phenomena [37, 38].

In this dissertation, ray tracing simulations were performed using Zemax OpticStudio, a widely used software platform for optical system modelling. The Non-Sequential Mode (NSC) was employed, as it allows the simulation of radiation interaction with arbitrarily complex surfaces and accounts for multiple scattering events. The NSC environment enables the import and generation of complex three-dimensional geometries, assignment of wavelength-dependent optical properties, and simulation of scattering processes without predefined ray paths. Custom radiation sources can be defined with specified angular and spectral characteristics, and the resulting angular distribution of reflected radiation can be analysed using virtual hemispherical detectors (Figures 2.4 and 2.5) [38].

https://doi.org/10.7795/110.20260928

The primary objective of the simulations was to evaluate the angular distribution of radiation reflected from candidate surface topologies developed in Section 2.2 and to assess their suitability for diffuse-like angular redistribution in the FIR. Special attention was given to the degree of angular redistribution and to deviations from ideal cosine-law scattering.

The modelling workflow followed a structured sequence. Surface geometries were first generated parametrically in Mathematica, enabling controlled variation of spatial frequencies and relief parameters. The resulting three-dimensional models were exported and imported into the non-sequential environment of Zemax OpticStudio. Within this framework, reflective material properties representative of metallic FIR surfaces were assigned. The surfaces were subsequently illuminated under defined incidence conditions, and the angular distribution of the reflected radiation was recorded using a hemispherical detector. This procedure enabled direct comparison of different surface concepts under identical radiometric conditions.

The simulations were performed using a simplified geometrical optics approach. The wavelength dependence was not explicitly included in the ray tracing procedure; instead, effective material properties were assigned to represent FIR reflectivity. The simulations were intended for comparative qualitative evaluation of candidate surface topologies rather than for quantitative prediction of BRDF characteristics.

A total of 200000 rays were used for each simulation. The surfaces were illuminated by an elliptical source with a diameter of 2 mm positioned at an incidence angle of 13° relative to the surface normal (Fig. 2.4). The angular distribution of reflected radiation was recorded using a hemispherical detector positioned around the sample. This configuration enabled qualitative evaluation of diffuse versus specular reflection behaviour and allowed comparison between different surface designs.

A hemispherical detector was used to capture the spatial distribution of reflected radiation. Such detectors are commonly used in radiometry and optical simulations for the analysis of bidirectional reflectance distribution functions and diffuse scattering processes [11, 19]. A broad and spatially distributed radiation pattern indicates diffuse-like scattering behaviour, whereas localized intensity maxima correspond to specular reflection components.

https://doi.org/10.7795/110.20260928

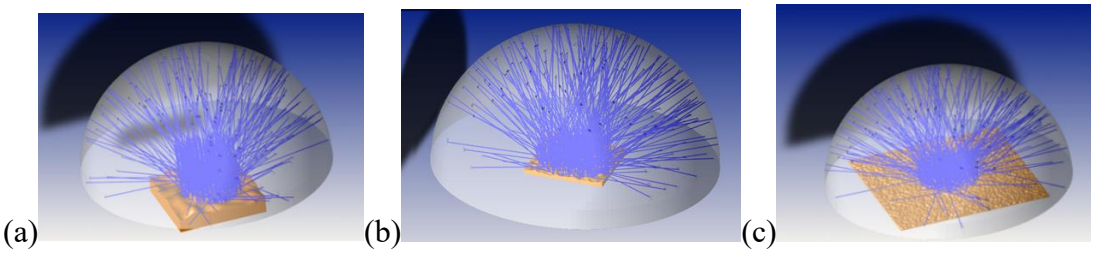


Fig. 2.4. Ray-tracing geometry of structured surface samples: (a) RHFS-400, (b) RHFS-800, and (c) RBS. The samples are illuminated at an incidence angle of 13° and positioned at the center of a hemispherical detector.

The simulation results were analysed in terms of:

- angular irradiance distribution,
- symmetry of reflection,
- presence of specular peaks,

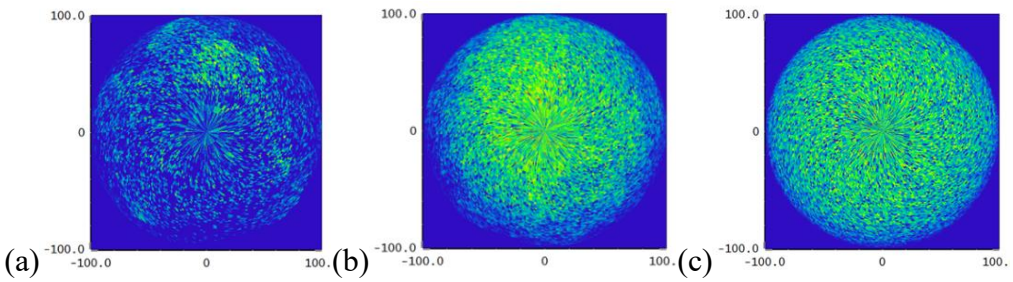


Fig. 2.5. Angular distribution of reflected radiation on the hemispherical detector for structured surface samples: (a) RHFS-400, (b) RHFS-800, and (c) RBS. The RHFS-400 surface exhibits a broad but weak and partially asymmetric distribution with a pronounced specular component. The RHFS-800 surface shows broader and more symmetric angular distribution. The RBS surface demonstrates a broad, highly uniform, and symmetric distribution

The simulation results (Fig. 2.5) reveal distinct differences in the angular scattering behaviour of the investigated surface concepts. The RHFS-400 surface (Fig. 2.5a) exhibits a broad angular distribution; however, the scattered intensity remains relatively low and a pronounced specular component is still present, indicating incomplete suppression of directional reflection. In addition, the angular distribution is not fully symmetric, reflecting the limited effectiveness of the surface topology at this spatial scale.

In contrast, the RHFS-800 surface (Fig. 2.5b), characterized by a more densely structured topology, exhibits a broader angular distribution of reflected radiation

https://doi.org/10.7795/110.20260928

compared to RHFS-400. The increased structural density leads to a wider spatial redistribution of the reflected radiation across the detector surface. The resulting radiation pattern appears visually broader and more evenly distributed, indicating improved approximation of diffuse-like scattering behaviour.

The RBS surface (Fig. 2.5c) exhibits a broad angular distribution of reflected radiation with no dominant specular peak, indicating pronounced angular redistribution. Compared to the RHFS-400 and RHFS-800 geometries, the reflected radiation appears visually more evenly distributed over the detector surface. These qualitative simulation results suggest that RBS geometries are capable of producing broad diffuse-like scattering behaviour.

2.4 Sample Manufacturing

The numerical modelling and ray-tracing analysis described in the previous sections identified several candidate surface geometries capable of producing diffuse scattering in the far-infrared spectral range. The next stage of the study involved the physical realization of these surfaces and evaluation of their manufacturability, reproducibility, and structural stability.

Fabrication of structured FIR surfaces presents specific challenges due to the required feature size (tens to hundreds of micrometres), the need for high reflectivity, and compatibility with metallic coatings. Conventional optical coatings used in the visible and near-infrared are not suitable in this wavelength range due to increased absorption and material dispersion. Therefore, the manufacturing strategy was focused on creating macro-structured surfaces followed by metallic coating optimized for high FIR reflectivity [2, 39].

Three main fabrication approaches were investigated:

- laser micro-texturing,
- CNC milling,
- additive manufacturing (3D printing) followed by metallization.

These methods allow the fabrication of structured surfaces with feature sizes comparable to FIR wavelengths and are commonly used in infrared optical engineering and microstructured material design [40].

https://doi.org/10.7795/110.20260928

2.4.1 Manufacture of random ball surfaces (RBS)

Random Ball Surfaces were realized using laser micro-texturing techniques. Laser surface structuring enables the formation of micro-scale protrusions and cavities with controlled geometry and spatial distribution and is widely applied in surface engineering for optical and thermal applications due to its precision [41].

The surface geometry used for fabrication was derived from the parametric RBS model described in Section 2.2.1. A representative computer-aided design (CAD) model of the surface is shown in Fig. 2.6.



Fig. 2.6. CAD representation of the RBS.

The fabricated samples were produced from aluminium substrates with dimensions of approximately 25 × 25 mm. More than 30 specimens were manufactured based on a single CAD model in order to evaluate production repeatability and structural consistency. Examples of fabricated samples are shown in Fig. 2.7, where noticeable variations in surface appearance can already be observed.

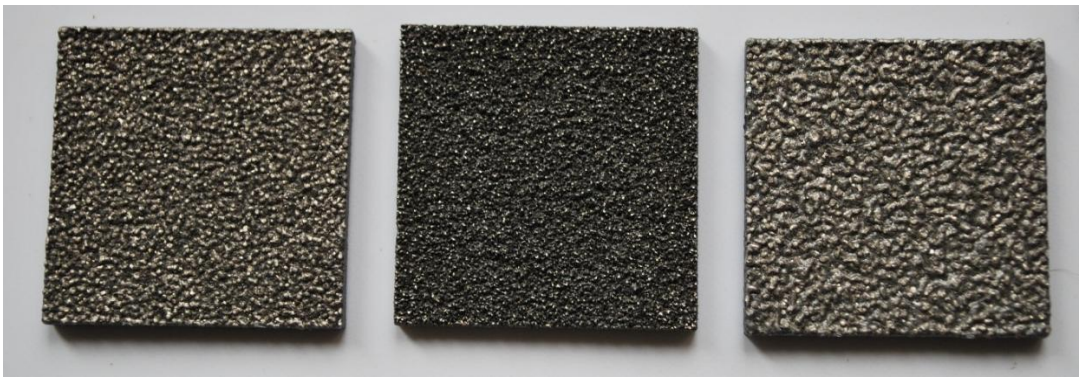


Fig. 2.7. Fabricated aluminium RBS samples (25 mm × 25 mm): RBS-1, RBS-2, and RBS-3. Although all samples were manufactured from the same CAD model, noticeable differences in surface topology are visible, illustrating the limited reproducibility of the laser micro-texturing process.

https://doi.org/10.7795/110.20260928

Microscopic inspection of the surfaces was carried out using a laser confocal microscope (Olympus LEXT OLS5000), which provides high-resolution topography and enables measurement of surface roughness and feature geometry (Fig. 2.8). Confocal laser microscopy is a standard tool for non-contact surface metrology and is particularly suitable for microstructured materials [42].

The measurements revealed deviations between the modelled geometry and the fabricated structures. As shown in Fig. 2.8, the actual surface morphology differs from the idealized spherical topology, with irregular feature shapes and partially merged structures. Furthermore, significant variations were observed between samples produced from the same design (Fig. 2.9), indicating limited reproducibility of the RBS approach using laser micro-texturing.

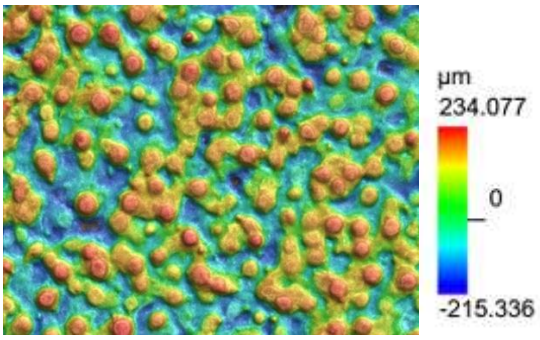


Fig. 2.8. Confocal laser microscopy topographical height map of the random ball surface (RBS-1). The colour scale represents the measured surface height variation in micrometres, illustrating deviations from the idealized spherical geometry and the presence of irregular surface features.

These structural deviations directly affect the scattering behaviour and reduce the suitability of this method for producing a uniform inner surface of an integrating sphere.

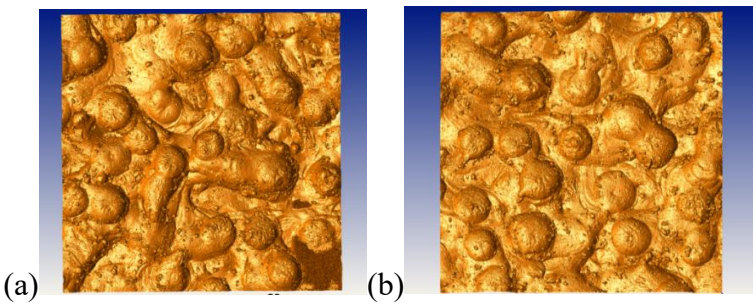


Fig. 2.9. Confocal laser microscopy of fabricated random ball surfaces: (a) RBS-1 and (b) RBS-2, demonstrating structural variability between samples produced from the same design.

https://doi.org/10.7795/110.20260928

In addition to local geometric inaccuracies, the observed sample-to-sample variability demonstrates limited reproducibility of the RBS fabrication process. Even when using identical design parameters, the resulting surface topologies differ significantly, making it difficult to ensure consistent radiometric performance.

This lack of reproducibility presents a critical limitation for practical implementation. The fabrication of an integrating sphere requires multiple segments with identical optical properties. However, the observed variability indicates that producing geometrically and optically equivalent segments using this approach is not feasible.

Consequently, each fabricated surface would require individual characterization, significantly increasing measurement complexity and uncertainty. These limitations ultimately restrict the applicability of the RBS concept for the realization of reliable and reproducible integrating sphere systems in the far-infrared.

2.4.2 Manufacture of random harmonic function surfaces (RHFS)

Surfaces based on harmonic functions were fabricated using additive manufacturing followed by metallic coating. This approach allows precise control of the geometry and provides higher reproducibility compared to laser micro-texturing used for RBS samples.

The structures were printed using a Formlabs Form 2 stereolithography (SLA) 3D printer with Tough 1500 V1 material. Additive manufacturing enables the fabrication of complex geometries and is increasingly used in optical component prototyping and terahertz engineering [40]. Representative computer-aided design (CAD) models of RHFS geometries are shown in Fig. 2.10.

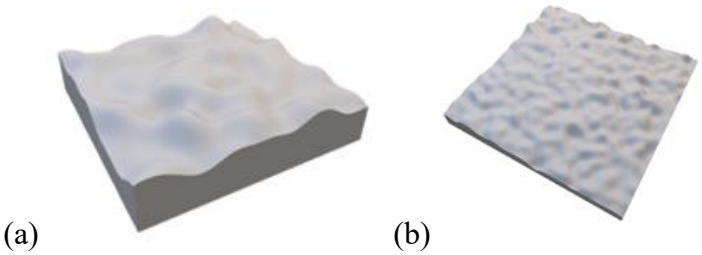


Fig. 2.10. CAD models of random harmonic function surfaces: (a) RHFS-400 and (b) RHFS-800.

https://doi.org/10.7795/110.20260928

After printing, the samples were coated with a thin gold layer using magnetron sputtering under vacuum conditions. Gold was selected due to its high reflectivity in the far-infrared spectral range, chemical stability, and resistance to oxidation, which ensures long-term stability of the optical properties [2, 39].

The thickness of the metallic coating was determined based on the electromagnetic skin effect. For conductive materials, the penetration depth of electromagnetic radiation is given by:

$$\delta = \sqrt{\frac{2}{\omega\mu\sigma}} \qquad (2.2)$$

where δ is the skin depth, $\omega$is the angular frequency, μ is the magnetic permeability, and σ is the electrical conductivity.

For far-infrared frequencies, the skin depth of gold is on the order of tens to hundreds of nanometres. Therefore, a coating thickness of approximately 200 nm is sufficient to ensure that the incident radiation is reflected predominantly by the metallic coating and does not significantly penetrate into the polymer substrate.

The resulting specimens had dimensions of approximately 36 × 36 mm with heights between 5 and 9 mm depending on the structural period. Fabricated RHFS samples are shown in Fig. 2.11, demonstrating high geometric consistency with CAD models. The fabrication process exhibited high reproducibility, and multiple identical samples were produced successfully.

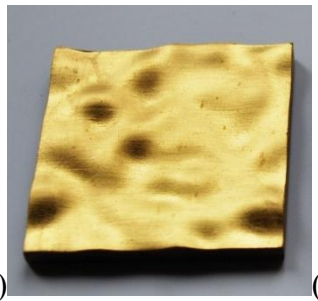
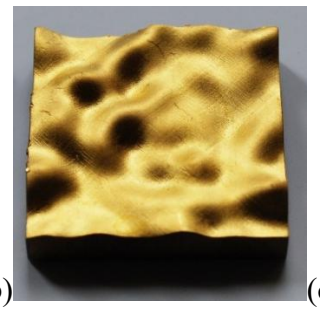
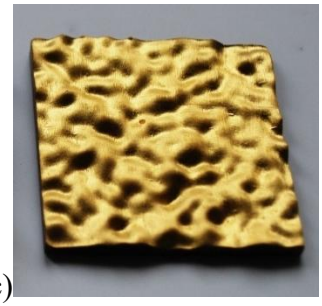
(a)  (b)  (c) 

Fig. 2.11. Fabricated random harmonic function surfaces (a) RHFS-200, (b) RHFS-400, and (c) RHFS-800 produced by additive manufacturing and coated with gold.

To evaluate alternative fabrication techniques, a selected harmonic structure was also produced from aluminium using CNC milling (Fig. 2.12). Due to the limited

https://doi.org/10.7795/110.20260928

resolution of the machining process, only geometries with sufficiently large feature sizes could be realized. In particular, the RHFS-400 structure was successfully manufactured, whereas finer structures such as RHFS-800 could not be reliably reproduced. The aluminium sample was subsequently polished and prepared for optical testing.

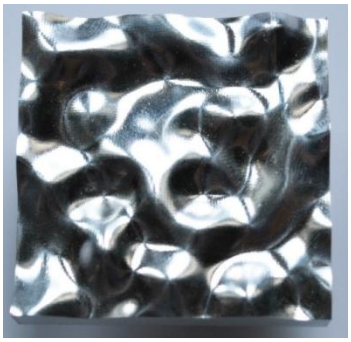


Fig. 2.12. CNC-milled aluminium sample of the RHFS-400.

2.5 Surface Analysis and THz Measurements

After fabrication, the developed surface structures were experimentally investigated to evaluate their scattering behaviour in the far-infrared spectral range. The primary objective of the measurements was to determine the angular distribution of reflected radiation and to assess the degree of diffuse versus specular reflection for the candidate surfaces.

Experimental validation is essential because numerical modelling alone cannot fully account for real surface imperfections, manufacturing tolerances, and material properties. For validation, a terahertz (THz) measurement system was employed. The use of this setup is motivated by its capability to operate in the far-infrared spectral range and to provide a sufficiently large illumination spot, ensuring interaction with a representative area of the structured surfaces. This capability is critical for reliable characterization, since the feature sizes of the investigated surfaces are comparable to the wavelength.

All samples were measured using a far-infrared molecular gas laser operating at discrete frequencies of 1.4 THz and 2.55 THz, corresponding to wavelengths of approximately 214 µm and 117 µm. These frequencies were selected as they represent the most stable operating points of the measurement system [43]. The radiation source consisted of an optically pumped CO_2 laser, a frequency-stabilizing etalon, and a THz

https://doi.org/10.7795/110.20260928

resonator filled with molecular gas, providing monochromatic and stable radiation suitable for metrological measurements in this range.

The beam was expanded to achieve a sufficiently large illumination area, ensuring interaction with a representative region of the structured surface. Large beam diameters are required in FIR measurements because surface features are comparable to the wavelength, and small spot sizes may lead to measurement artefacts. The measurement spot diameter was approximately 12 mm for $\lambda = 214$ μm and approximately 8 mm for $\lambda = 117$ μm.

The measurement configuration is shown in Fig. 2.13. The setup was designed to determine the angular distribution of reflected radiation. A fixed THz radiation source was used, while the sample was mounted on a motorized rotation stage. The detector was positioned at a fixed angle of 25° relative to the incident beam. During measurements, the sample was rotated from −40° to +40° with a step size of 1°, enabling the recording of angular scattering profiles.

A photograph of the experimental setup is presented in Fig. 2.14. The reflected radiation was detected using a Golay cell detector with an aperture of 11 mm positioned at a distance of approximately 300 mm from the sample. Golay detectors are gas-filled thermal detectors widely used in the far-infrared and THz spectral regions due to their broadband sensitivity and room-temperature operation [43]. The detector signal was recorded as a function of the sample rotation angle.

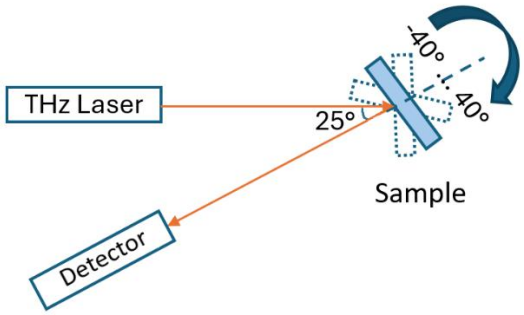


Fig. 2.13. Schematic of the angular-resolved THz reflection measurement setup. The sample is rotated over an angular range of -40° to +40°.

https://doi.org/10.7795/110.20260928

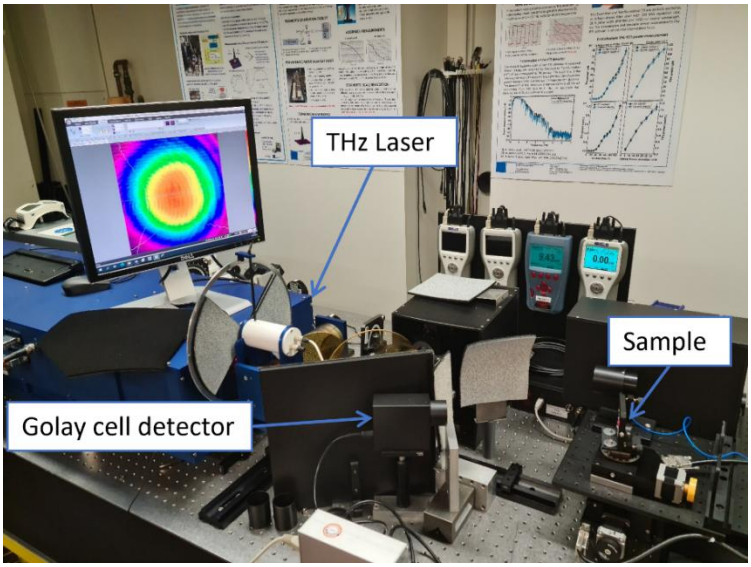


Fig. 2.14. Photograph of the experimental THz measurement setup used for surface sample characterization, including the THz radiation source, the sample stage, and the Golay cell detector.

The investigated samples included Random Ball Surfaces (RBS-1 and RBS-2), fabricated via laser micro-texturing, and Random Harmonic Function Surfaces (RHFS-200, RHFS-400, and RHFS-800), manufactured using additive techniques with subsequent gold coating. In addition, an RHFS-400 sample fabricated by CNC milling was investigated for comparison.

For reference measurements, a plane gold mirror and an Infragold-coated sample were characterized. A polished gold mirror represents an ideal specular reflector in the FIR region, whereas Infragold is a diffuse coating commonly used in integrating spheres for the mid-infrared (MIR) spectral range. In the present work, it serves as a reference to assess the transition from MIR-optimized diffuse behaviour to the FIR regime, where its scattering efficiency is expected to decrease due to surface-scale limitations [14, 16, 17]. Comparison with reference samples allowed identification of the transition from specular to diffuse reflection behaviour in the fabricated structures.

The experimental analysis focused on the angular width of the reflected radiation distribution, the presence of specular components, and the agreement between simulation and measurement results. These parameters provide a direct assessment of the suitability of the investigated surfaces for integrating sphere applications, where broad and stable diffuse-like angular redistribution is required.

https://doi.org/10.7795/110.20260928

2.6 Measurement Results

The angular scattering behaviour of the fabricated surface structures was evaluated based on the detector signal recorded as a function of the sample rotation angle for two wavelengths: λ = 214 µm (1.4 THz) and λ = 117 µm (2.55 THz).

In all presented graphs, the horizontal axis represents the observation angle relative to the surface normal (in degrees), while the vertical axis shows the detector signal in arbitrary units (a.u.), proportional to the radiant power registered by the detector. The angular scanning range was from -40° to +40°.

For comparison with ideal diffuse behaviour, a scaled Lambertian cosine distribution is included in the figures. All measurements were performed under identical optical alignment and detector conditions, allowing direct comparison between different surface geometries.

2.6.1 Reference measurements: Gold mirror and Infragold

Reference measurements were performed using a gold mirror (Y_2O_3 overcoat) and an Infragold-coated sample in order to establish baseline scattering behaviour in the far-infrared range.

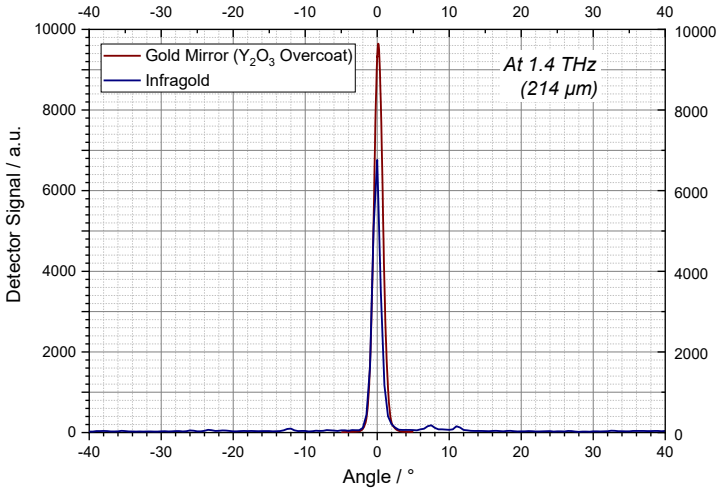


Fig. 2.15. Angular distribution of reflected radiation for a gold mirror (Y_2O_3 overcoat) and an Infragold-coated surface at 1.4 THz (λ= 214 µm). Both samples exhibit strongly peaked distributions, indicating predominantly specular reflection behaviour in the far-infrared range.

https://doi.org/10.7795/110.20260928

The gold mirror represents an ideal specular reflector. As shown in Fig. 2.15, the measured angular distribution exhibits a narrow peak concentrated around the specular reflection direction, confirming the correct alignment of the measurement system and providing a reference for purely specular behaviour. The measurement geometry was defined such that the detector was positioned at 25° relative to the incident beam, corresponding to the specular reflection direction of the gold mirror. This alignment was used as the reference condition for all subsequent angular measurements, with the scanning range defined relative to this position.

The Infragold sample, which is commonly used as a diffuse reflector in the near- and mid-infrared spectral ranges, exhibits a behaviour that is effectively specular in the FIR [44]. As observed in Fig. 2.15, the angular distribution is strongly peaked and closely resembles that of the gold mirror, indicating that diffuse scattering is negligible at this wavelength. This confirms that Infragold does not provide Lambertian-like reflection in the far-infrared and behaves predominantly as a specular reflector under these conditions.

2.6.2 RBS: reproducibility limitations

Random Ball Surfaces (RBS) were among the first investigated geometries. These structures were expected to produce multi-directional scattering due to randomly distributed spherical elements with characteristic dimensions comparable to FIR wavelengths.

The experimental results for RBS-1 and RBS-2 are presented in Figs. 2.16 and 2.17. In both cases, the measured angular distributions are relatively broad, indicating the presence of diffuse scattering components. However, the distributions deviate significantly from the ideal Lambertian cosine behaviour. In particular, pronounced local maxima are observed, indicating residual specular contributions and non-uniform angular redistribution of the reflected radiation.

Furthermore, the overall signal level remains relatively low and unevenly distributed across the angular range, suggesting limited scattering efficiency. The angular profiles exhibit irregular structure, which is not consistent with smooth diffuse-like angular redistribution.

https://doi.org/10.7795/110.20260928

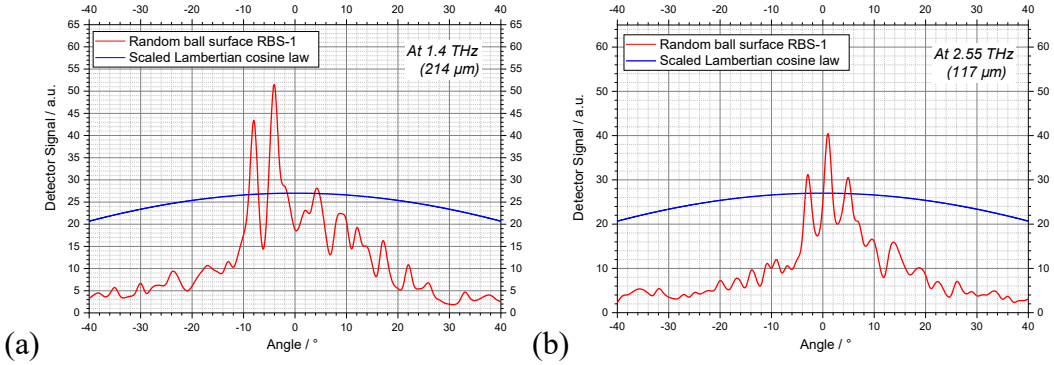


Fig. 2.16. Angular distribution of reflected radiation from the random ball surface RBS-1 at (a) 1.4 THz (214 μm) and (b) 2.55 THz (117 μm). The measured data (red) are compared with a scaled Lambertian cosine distribution (blue).

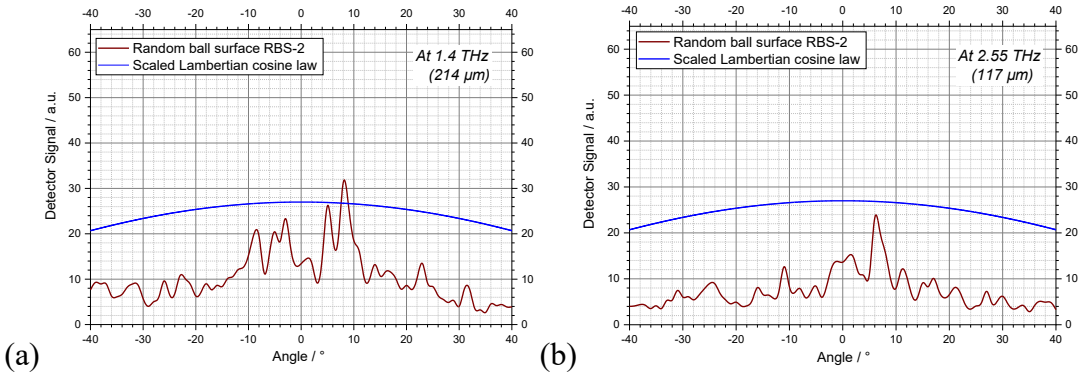


Fig. 2.17. Angular distribution of reflected radiation from the random ball surface RBS-2 at (a) 1.4 THz (214 μm) and (b) 2.55 THz (117 μm). The measured data (brown) are compared with a scaled Lambertian cosine distribution (blue).

A key observation is the significant variation between samples fabricated from the same design. As seen in Figs. 2.16 and 2.17, RBS-1 and RBS-2 exhibit noticeably different angular distributions, despite being based on the same nominal geometry. This confirms the limited reproducibility already identified from the structural analysis (Section 2.4.1).

As a consequence, the optical behaviour of RBS structures cannot be reliably predicted or reproduced. Although these surfaces exhibit partial diffuse scattering, the combination of non-Lambertian angular distributions, residual specular components, and poor reproducibility makes them unsuitable for implementation as the internal surface of an integrating sphere, where uniformity and repeatability are essential.

https://doi.org/10.7795/110.20260928

2.6.3 RHFS-200: predominantly specular behaviour

The surface RHFS-200 represents the smoothest harmonic structure with the largest spatial period. Figure 2.18 presents the angular dependence of the detector signal for the RHFS-200 surface measured at $\lambda = 214$ μm.

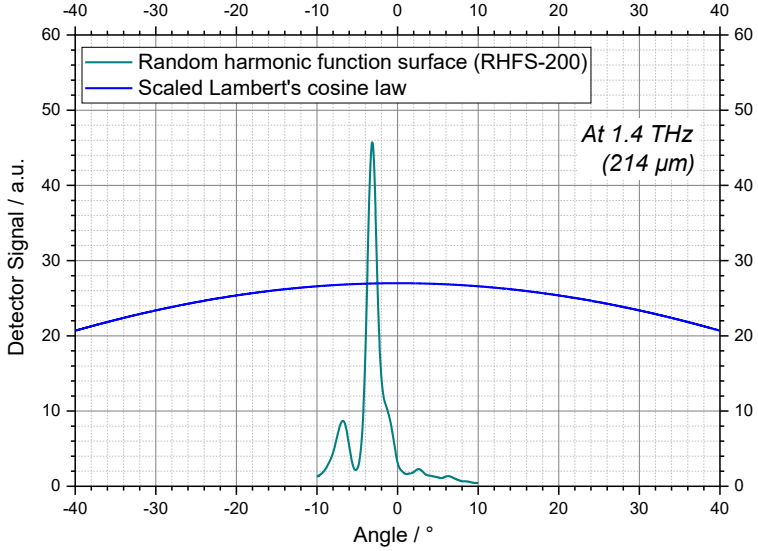


Fig. 2.18. Angular distribution of reflected radiation from the random harmonic function surface RHFS-200 at 1.4 THz (214 μm). The measured data (green) are compared with a scaled Lambertian cosine distribution (blue).

The measured signal exhibits a narrow peak centred near the specular reflection direction, with a rapid decrease in intensity outside this region. The angular distribution is significantly narrower than the corresponding Lambertian cosine profile, indicating predominantly specular reflection.

This behaviour can be explained by the relation between the characteristic surface feature size and the incident wavelength. For RHFS-200, the surface structure is insufficiently developed to induce effective angular redistribution of radiation. As a result, the surface behaves optically smooth in the far-infrared, and scattering remains largely directional [33].

Based on this result, additional measurements at shorter wavelengths were not performed, as the surface does not exhibit sufficient diffuse scattering under the investigated conditions. Consequently, RHFS-200 does not provide sufficient diffuse

https://doi.org/10.7795/110.20260928

scattering in the FIR range and is not suitable for use as an internal diffuse-scattering reflector in integrating sphere applications.

2.6.4 RHFS-400: transitional scattering regime

The angular reflection distributions measured for the RHFS-400 surface are presented in Fig. 2.19 for wavelengths of 214 µm and 117 µm.

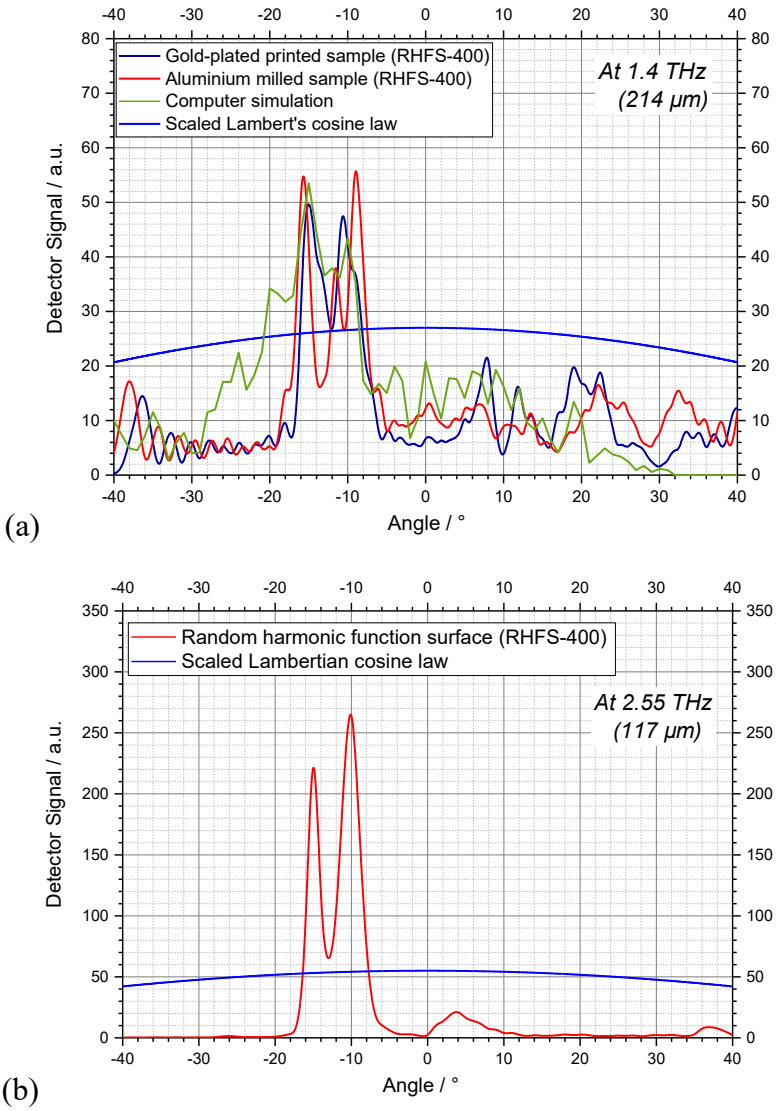


Fig. 2.19. Angular distribution of reflected radiation from the RHFS-400 surface at (a) 1.4 THz (214 µm) and (b) 2.55 THz (117 µm). Measurements for additively manufactured gold-coated and CNC-milled samples are compared with ray-tracing simulation and a scaled Lambertian cosine distribution.

https://doi.org/10.7795/110.20260928

At λ = 214 µm, the measured distribution is significantly broader than that observed for RHFS-200, indicating the onset of diffuse scattering. However, the angular profile still deviates from the ideal Lambertian cosine distribution and exhibits pronounced local maxima. These peaks indicate the presence of residual specular components, which can be attributed to quasi-faceted regions of the harmonic surface structure.

Measurements performed on an additively manufactured, gold-coated sample and on a CNC-milled aluminium sample show good agreement (Fig. 2.19, red and blue curves). This demonstrates that the scattering behaviour is primarily governed by the surface geometry, while the fabrication method has a secondary influence, provided that the geometric structure is preserved. The experimental results are in good qualitative agreement with the numerical ray-tracing simulations (Fig. 2.19, green curve). The simulated distribution reproduces the overall angular width and the presence of local intensity variations observed in the measurements.

For the shorter wavelength λ = 117 µm, only one representative measurement is shown, as the results obtained for different fabrication methods exhibited similar behaviour and did not introduce additional features in the angular distribution. At this wavelength, the angular distribution becomes more structured and exhibits stronger directional features. This behaviour indicates that, despite the increased relative roughness at shorter wavelengths, the scattering remains non-uniform and continues to be influenced by local surface geometry.

Overall, the RHFS-400 surface demonstrates a transitional scattering regime, characterized by a combination of diffuse and directional reflection components. While the angular distribution is significantly broader than that of RHFS-200, it does not yet achieve Lambertian behaviour.

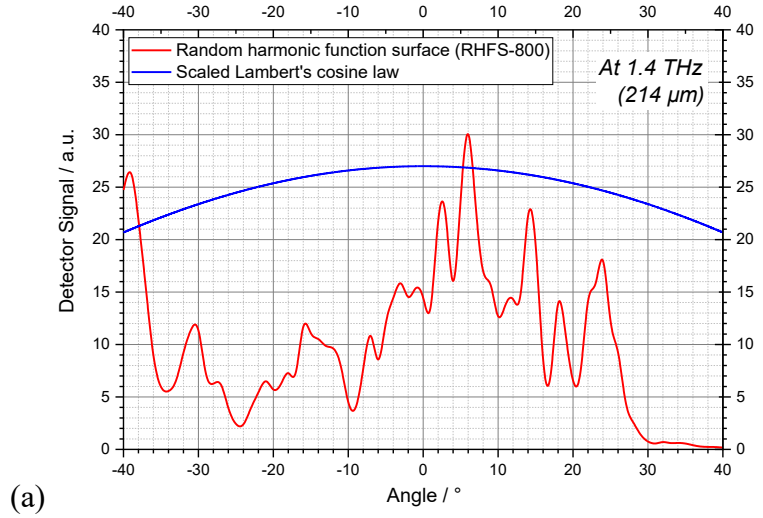
2.6.5 RHFS-800: broadband diffuse scattering

The angular reflection distributions measured for the RHFS-800 surface are presented in Fig. 2.20 for both investigated wavelengths. The detector signal is plotted as a function of the observation angle, and a scaled Lambertian cosine distribution is included as a reference.

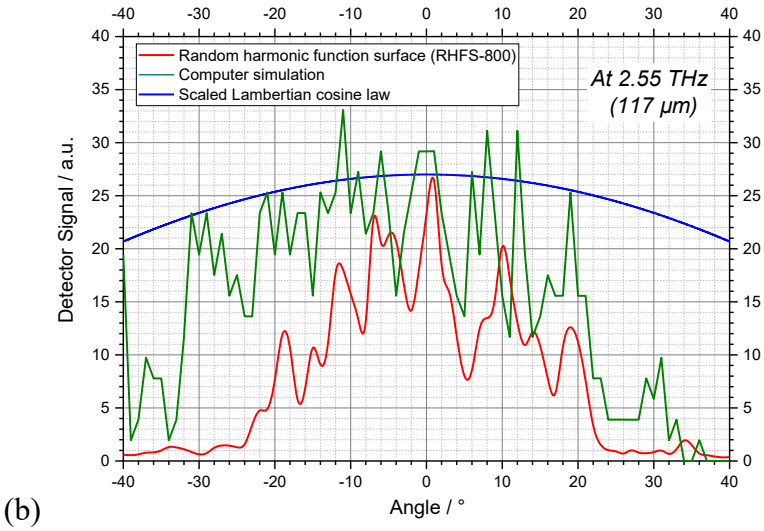
https://doi.org/10.7795/110.20260928

At λ = 214 μm, the measured distribution is significantly broader than that of the RHFS-400 surface and does not exhibit a dominant specular peak. The overall shape of the curve approaches the behaviour expected for diffuse scattering, although local intensity variations are still present.

At λ = 117 μm, the angular distribution remains wide and more uniformly distributed over the measurement range compared to RHFS-400. While deviations from the ideal Lambertian profile persist, the reflected radiation is redistributed over a broad angular range without pronounced directional peaks.



(a)



(b)

Fig. 2.20. Angular distribution of reflected radiation from the RHFS-800 surface at (a) 1.4 THz (214 μm) and (b) 2.55 THz (117 μm), compared with ray-tracing simulation and a scaled Lambertian cosine distribution.

https://doi.org/10.7795/110.20260928

The same surface was analysed using numerical ray-tracing simulations that reproduce the measurement geometry. The simulated angular distribution shows good qualitative agreement with the experimental data, capturing both the overall angular width and the characteristic intensity variations. This confirms that the observed scattering behaviour is primarily governed by the designed surface topology.

Small discrepancies between measurement and simulation can be attributed to practical factors such as slight sample misalignment, finite sample size leading to edge reflections, local surface imperfections, and variations in the illumination conditions.

Overall, the RHFS-800 surface demonstrates stable broadband scattering with significantly improved angular redistribution compared to RHFS-200 and RHFS-400. Although the distribution is not perfectly Lambertian, it provides sufficiently broad and stable diffuse-like scattering behaviour for integrating-sphere radiometric applications.

Based on the combined results of modelling, fabrication, and experimental validation, the RHFS-800 topology was therefore selected for implementation as the internal surface topology of the far-infrared integrating sphere. This choice is supported by its reproducible fabrication, stable scattering behaviour, agreement with numerical simulations, and suitability for angular redistribution at long wavelengths.

https://doi.org/10.7795/110.20260928

Chapter 3. Design and Fabrication of the Far-Infrared Integrating Sphere

This chapter presents the transition from the surface concepts developed in Chapter 2 to a physically realizable integrating sphere designed for directional–hemispherical measurements at long wavelengths.

The RHFS-based surface topology is transferred from a planar geometry to a spherical configuration while aiming to preserve the angular redistribution characteristics of the original surface. Based on the results of the previous chapter, the RHFS-800 structure is selected as the internal surface topology of the integrating sphere.

The integrating sphere was developed for the measurement of directional–hemispherical reflectance and transmittance, as introduced in Chapter 1. In this measurement configuration, radiation is incident on the sample from a defined direction, while the reflected or transmitted flux is collected over the hemisphere. This requirement imposes strict constraints on the angular redistribution behaviour and geometrical design of the sphere.

Key design parameters, including sphere diameter, wall thickness, and port configuration, are defined with respect to both radiometric requirements and manufacturing constraints. Particular attention is given to preserving the angular redistribution characteristics of the RHFS topology after transformation into the curved sphere geometry.

The implementation of the design is carried out using a segmented CAD approach suitable for additive manufacturing. Among the evaluated fabrication methods, stereolithography is selected due to its ability to reproduce the required surface topology with sufficient geometrical fidelity.

The chapter further addresses post-processing procedures, including surface finishing, gold coating of the internal structure, and assembly of the segmented sphere. The final result is a fabricated integrating sphere suitable for directional–hemispherical radiometric measurements in the wavelength range from 25 μm to 100 μm.

https://doi.org/10.7795/110.20260928

3.1 Concept and Design Requirements

The integrating sphere developed in this work is designed for directional–hemispherical reflectance and transmittance measurements in the wavelength range from 25 µm to 100 µm. Its development is motivated by increasing radiometric demands in long-wavelength applications, including future space missions (e.g., ESA FORUM), where accurate knowledge of radiative properties including both diffuse and specular contributions is required for instrument calibration and radiative transfer modelling [1, 4, 6, 7, 8].

The measurement objective is to provide stable and reproducible directional–hemispherical radiative quantities with an overall uncertainty on the order of 10% ($k = 2$), suitable for method development, validation, and comparison with metrological reference facilities. Such performance is required to support traceable long-wavelength radiometry and to bridge the gap between laboratory measurements and space-borne radiative observations [4].

A key functional requirement is that the sphere provides hemispherical collection and angular redistribution of reflected and transmitted radiation. In this way, the measured signal becomes less sensitive to the detailed angular scattering distribution of the sample. This condition is particularly important at long wavelengths, where many materials exhibit pronounced diffuse scattering components and where purely directional measurements may lead to incomplete radiative characterization [11, 33, 34].

In contrast to integrating spheres used in the visible and near-infrared spectral ranges, operation at long wavelengths imposes additional constraints related to wavelength-scale surface structures, increased absorption in conventional coatings, and the suppression of specular contributions. Consequently, the geometry must ensure efficient angular redistribution of radiation while avoiding direct optical paths between illumination, sample, and detector.

To fulfil these requirements, the sphere geometry must promote multiple internal reflections within the cavity, ensuring that the detected signal is dominated by multiply redistributed radiation rather than by direct or specular components.

https://doi.org/10.7795/110.20260928

The overall dimensions of the sphere are defined as a compromise between radiometric performance and manufacturability. A sphere with an internal diameter of 150 mm ($r_0 = 75$ mm) was selected to provide a sufficient optical path length for multiple reflections while maintaining a compact and manufacturable design.

The sphere includes multiple ports enabling flexible measurement configurations. In the substitution method, two ports remain open during measurement, whereas in the comparison method with a rotating sample stage three ports are open. All remaining ports are closed using coated plugs in order to preserve the integrating performance of the cavity and minimize radiative losses.

All main ports have a diameter of 30 mm. For the selected sphere size, this configuration ensures that the effective port fraction remains within a suitable range, allowing sufficient radiance build-up and efficient angular redistribution within the cavity. Maintaining a low port fraction is essential, since increasing open areas reduces the internal radiance level and degrades the integrating performance.

The entire inner surface of the sphere is structured using the RHFS-800 topology developed in Chapter 2. This surface provides broad diffuse-like scattering behaviour and enables efficient angular redistribution of radiation through multiple reflections. It serves as an alternative to conventional diffuse coatings, which exhibit limited performance at long wavelengths, and represents a key element of the present sphere concept. The use of a parametrically defined and reproducible surface further enables consistent fabrication by additive manufacturing.

3.2 Transfer of the RHFS-800 Surface into Spherical Geometry

This section describes the mathematical and algorithmic procedure used to transfer the RHFS-800 surface topology, developed in Chapter 2 on a planar domain, to a spherical geometry. The objective of this transformation is to preserve the statistical roughness, spatial correlation, and characteristic surface topology associated with diffuse-like scattering behaviour of the surface while adapting it to the internal geometry of the integrating sphere.

The RHFS-800 surface was originally generated as a two-dimensional stochastic height field based on randomized harmonic-function-based topology. A representative planar realization of this surface is shown again in Fig. 3.1(a). For application as

https://doi.org/10.7795/110.20260928

the internal structure of the integrating sphere, the planar surface must be mapped onto a spherical coordinate system without introducing significant distortions that would substantially alter its scattering behaviour at long wavelengths.

A direct geometric projection of a planar surface onto a sphere leads to strong deformation of microstructural features, particularly near the poles. This effect arises from the non-uniform metric of spherical coordinates, where the surface element is given by:

$$dA = r^2 \sin\,\theta\, d\theta\, d\phi \qquad (3.1)$$

where r is the sphere radius, and θ and ϕ are the polar and azimuthal angles, respectively. As the polar angle θ decreases, the effective azimuthal spacing contracts, leading to artificial compression of surface features and modification of local slopes and normals. Such distortions would influence the scattering behaviour and should therefore be minimized.

The objective of the transformation is therefore not purely geometric, but also the preservation of the characteristic optical functionality of the original surface topology. In particular, the statistical distribution of surface heights and spatial frequencies responsible for diffuse-like scattering behaviour should be preserved as closely as possible.

The initial RHFS-800 surface is represented numerically as a two-dimensional height field:

$$z = h(x, y) \qquad (3.2)$$

where $h(x, y)$ represents the surface height defined over the planar domain.

To transfer this surface to a hemispherical geometry, the planar coordinates are re-parameterized using spherical angular variables. The polar angle $\theta$is defined over the interval $[0, \pi]$, while the azimuthal angle ϕspans a hemispherical domain. The discretization is derived from the resolution of the original planar data, preserving correspondence between planar and spherical sampling points. A representative surface segment used for this mapping is shown in Fig. 3.1(b). The characteristic size of these segments corresponds to the dimensions of the planar samples used in Chapter 2

https://doi.org/10.7795/110.20260928

(approximately $36 \times 36\ \mathrm{mm}^2$), ensuring consistency between numerical modelling and experimental surface realizations.

A direct global interpolation of the high-resolution surface over the hemisphere proved to be numerically unstable and computationally inefficient. Therefore, a piecewise algorithm was implemented. The surface data were divided into contiguous angular segments along the azimuthal direction. For each segment, a local interpolation function $h_i(\theta, \phi)$was constructed, and the resulting functions were combined into a piecewise-defined representation ensuring continuity and numerical stability. The segmentation scheme of the hemisphere is illustrated in Fig. 3.1(c).

A critical aspect of the transformation is the preservation of the surface roughness distribution across the spherical geometry. Without correction, the convergence of meridians near the poles leads to artificial densification of microstructures and altered scattering behaviour. To compensate for this geometric effect, a coordinate transformation was introduced:

$$\phi' = \phi \sin\ \theta \qquad (3.3)$$

where ϕ' is the corrected azimuthal coordinate. This transformation compensates for the $\sin\theta$ dependence of the surface element (Eq. 3.1) and minimizes artificial compression of surface features. As a result, microstructural features retain their spatial distribution and are not artificially compressed near the poles.

After applying this correction, the hemispherical surface is constructed as a radial displacement from a reference sphere of radius r_0:

$$r(\theta, \phi) = r_0 - h(\theta, \phi') \qquad (3.4)$$

where r_0 is the radius of the reference sphere (75 mm), and $h(\theta, \phi')$represents the surface relief. In this formulation, the RHFS-800 structure becomes an intrinsic part of the spherical geometry.

The resulting structured hemisphere is shown in Fig. 3.1(d). This approach preserves local slopes, spatial correlations, and microfacet orientations, which are essential for maintaining diffuse scattering behaviour at long wavelengths.

https://doi.org/10.7795/110.20260928

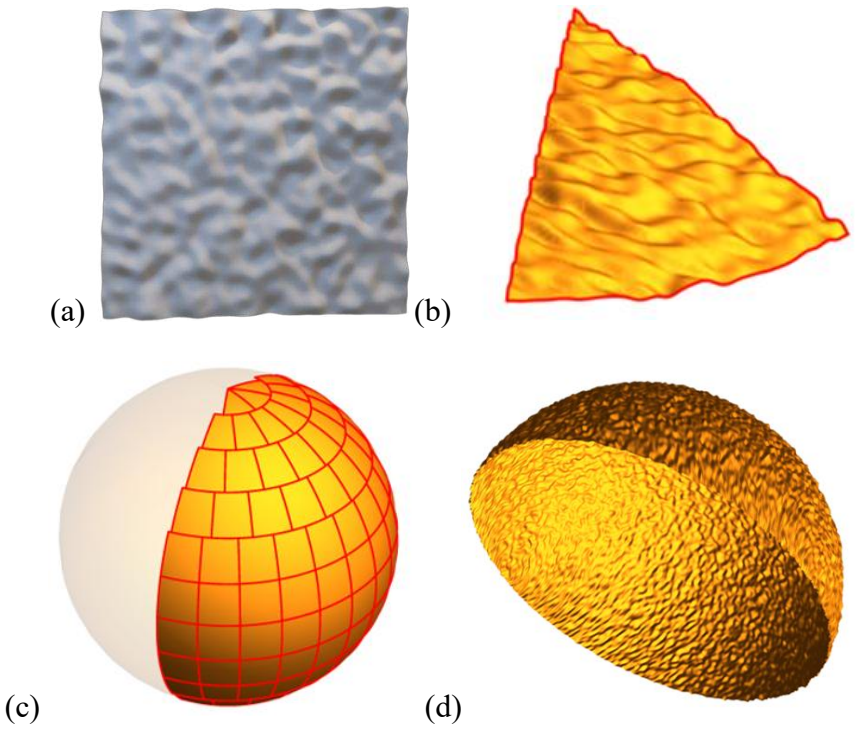


Fig. 3.1. Transfer of the RHFS-800 surface topology to a hemispherical geometry: (a) planar RHFS-800 surface (shown for reference); (b) extracted surface segment used for mapping; (c) segmentation of the hemisphere into manufacturable patches; (d) resulting structured hemispherical surface.

After obtaining the RHFS-800 surface in spherical form, the transformation defined by Eqs. (3.3) and (3.4) was applied to a sphere with a reference radius of 75 mm. To verify the correctness of the mapping and to evaluate potential distortions, a representative spherical test segment was generated in the pole region.

This test geometry is shown in Fig. 3.2. The result demonstrates that the microstructural distribution remains visually consistent even in the polar regions of the sphere, where geometric distortions are typically most pronounced due to the convergence of meridians. This indicates that the characteristic surface topology is retained after transformation.

The developed transformation method establishes a direct link between the numerical modelling of diffuse FIR surfaces (Chapter 2) and the physical realization of the integrating sphere. By preserving the statistical surface characteristics and minimizing geometrical distortions during the transformation, the method supports the

https://doi.org/10.7795/110.20260928

transfer of the diffuse-like scattering behaviour predicted for the planar RHFS-800 topology to the final spherical structure.



Fig. 3.2. Test spherical segment with RHFS-800 surface mapped onto a curved geometry in the pole region. The preserved microstructural distribution indicates that no significant geometric distortion is introduced by the transformation.

3.3 Sphere Geometry Design

The geometry of the integrating sphere developed in this work is defined based on the requirements of directional–hemispherical reflectance and transmittance measurements in the wavelength range from 25 μm to 100 μm, as well as on established radiometric principles of integrating sphere design [13, 14, 34].

The sphere combines a spherical cavity with a structured internal surface (RHFS-800) and a metallic reflective coating, forming a unified optical system for hemispherical collection and angular redistribution of radiation at long wavelengths. The geometrical configuration is therefore directly linked to the measurement methodology and cannot be considered independently of the radiometric principles governing the measurement process.

Unlike conventional integrating spheres operating in the visible or near-infrared spectral ranges, where diffuse coatings determine the optical behaviour, the present design relies on the combined effect of geometry, the RHFS-800 surface, and the effective reflectivity of the cavity walls. The RHFS-800 surface promotes angular redistribution of radiation, while the gold coating provides high effective reflectivity of the cavity walls, enabling multiple internal reflections within the sphere.

https://doi.org/10.7795/110.20260928

3.3.1 Measurement-driven geometrical concept

The geometry of the integrating sphere was derived directly from the measurement configurations it is intended to support. In this work, two principal radiometric methodologies were considered: the substitution method and the comparison method, both widely used in integrating-sphere reflectance measurements [14, 45, 46, 47]. The substitution and comparison measurement principles are illustrated in Fig. 3.3. In addition, angular configurations enabling separation of diffuse and specular reflection components were incorporated into the design.

In the substitution method (Fig. 3.3(a)), directional–hemispherical quantities are determined sequentially by measuring a reference and a sample under identical optical conditions. In this configuration, only two ports are open simultaneously: the illumination port (Port 2) and the detector port (Port 1), while the reference or sample is positioned at the lateral measurement port (Port 4). The incident radiation enters the sphere at an angle of 8° relative to the surface normal of the sample, as indicated in Fig. 3.3(a). This arrangement minimizes port losses and ensures stable integrating performance.

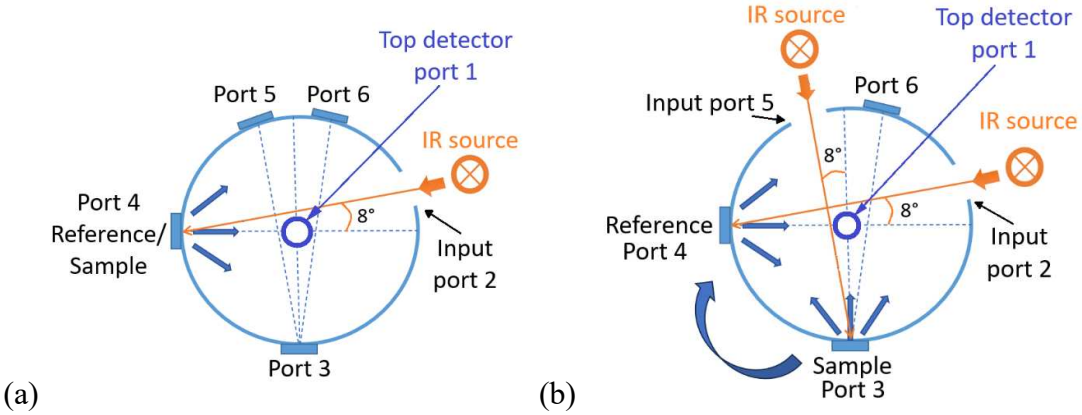


Fig. 3.3. Measurement principles used for the integrating sphere design: (a) substitution method and (b) comparison method, illustrating sequential and alternating illumination of reference and sample. In the comparison configuration, the same fixed IR source is used before and after rotation of the sphere assembly. The detector port (Port 1), located on the upper side of the sphere, is indicated schematically.

In the comparison method (Fig. 3.3(b)), the reference and sample are mounted simultaneously, while both the radiation source and the detector remain fixed. The integrating sphere is mounted on a rotating stage, allowing alternating illumination of the reference (Port 4) and the sample (Port 3) without mechanical replacement. In both

https://doi.org/10.7795/110.20260928

positions, the incident radiation is directed at 8° relative to the corresponding surface normal. In this configuration, three ports are open: the detector port (Port 1) and two illumination ports corresponding to the reference and sample positions (Ports 2 and 5).

This measurement approach is particularly advantageous for operation under vacuum conditions, where manual exchange of samples is impractical. The alternating measurement sequence enables continuous monitoring of signal drift and improves measurement stability. As a result, the method provides enhanced repeatability and reduced sensitivity to temporal variations such as temperature fluctuations and source instability.

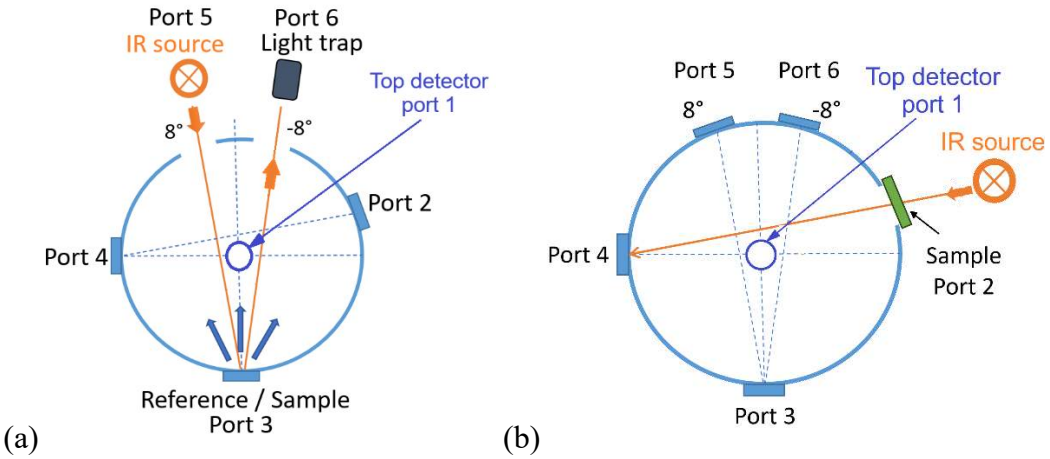


Fig. 3.4 Additional measurement configurations supported by the integrating sphere: (a) 8°/8° reflection geometry for specular-excluded measurements. Radiation is incident on the reference or sample at Port 3 through Port 5, while Port 6 is equipped with a light trap to suppress the specular reflection component. The remaining radiation is redistributed inside the sphere and detected at the top detector port (Port 1). (b) Directional–hemispherical transmittance measurement using the substitution method. In the reference state, radiation enters the sphere through the open Port 2; in the sample state, the sample is mounted at Port 2 and only the transmitted radiation enters the sphere and is detected at Port 1.

The sphere additionally supports an 8°/8° reflection geometry for separating specular and diffuse reflection contributions (Fig. 3.4(a)). In this notation, the first angle denotes the angle of incidence and the second angle denotes the observation angle, both defined with respect to the sample normal. Radiation is incident on the reference or sample at Port 3 through Port 5 at an angle of 8°. Port 6 is positioned symmetrically with respect to the sample normal and corresponds to the specular reflection direction. When Port 6 is equipped with a light trap and the detector remains located at the top

https://doi.org/10.7795/110.20260928

detector port (Port 1), the specular component is suppressed before it can contribute to the detected signal. The remaining radiation is redistributed inside the sphere and detected at Port 1. This configuration therefore enables specular-excluded directional–hemispherical reflectance measurements.

The standard directional–hemispherical reflectance configurations described above correspond to specular-included measurement conditions, since the specular component remains inside the sphere and contributes to the detected signal. In contrast, the 8°/8° geometry with a light trap at Port 6 provides access to the specular-excluded reflectance component. These measurement principles follow established approaches used in the radiometric characterization of optical materials [11, 14].

In addition to reflectance measurements, the integrating sphere also supports directional–hemispherical transmittance measurements using the substitution method (Fig. 3.4(b)). In this configuration, the incident radiation is directed towards Port 2. In the reference measurement, Port 2 remains open, so that the radiation enters the sphere without passing through a sample. The admitted radiant flux is redistributed by multiple reflections within the cavity and detected at the top detector port (Port 1). In the sample measurement, the investigated sample is mounted at Port 2 under the same optical alignment conditions. Only the radiation transmitted through the sample enters the integrating sphere, where it is collected within the cavity and detected at Port 1. The directional–hemispherical transmittance is obtained from the ratio of the detected signal with the sample in place to the signal recorded for the open-port reference measurement. This configuration therefore determines the fraction of incident radiant flux transmitted through the sample and collected over the corresponding hemisphere.

Based on the analysis of these measurement configurations, the geometrical design of the integrating sphere was defined to accommodate the required measurement modes within a single system. The resulting configuration includes five functional ports (Ports 2–6) and one detector port (Port 1). This geometry enables implementation of the substitution and comparison methods, supports specular-included and specular-excluded reflectance measurements, and allows directional–hemispherical transmittance measurements, while maintaining reproducible measurement geometry and minimizing alignment-related systematic effects.

https://doi.org/10.7795/110.20260928

3.3.2 Sphere size and port configuration

The internal diameter of the integrating sphere was selected as 150 mm (r_0=75 mm) based on a trade-off between radiometric performance and practical implementation.

A sufficiently large sphere is required to promote multiple internal reflections and effective angular redistribution of radiation. However, increasing the sphere size reduces the irradiance at the detector and complicates the mechanical realization and integration into the measurement setup. The selected diameter therefore represents a compromise that ensures adequate spatial averaging while maintaining sufficient signal level and mechanical feasibility.

The port configuration of the sphere was derived directly from the measurement concepts described in Section 3.3.1. In order to support substitution and comparison methods, as well as 8°/8° measurement geometries, one detector port (Port 1), five lateral functional ports (Ports 2–6), and one auxiliary bottom port (Port 7) were implemented. The top port (Port 1) is used for the detector, while the lateral ports enable illumination, sample and reference positioning, and optional specular-included or specular-excluded configurations.

The auxiliary bottom port (Port 7), located at the lower part of the sphere, was not used in the measurements presented in this work. It was nevertheless included in the design to provide greater flexibility for future measurement configurations. In particular, this port becomes relevant if the detector is positioned laterally rather than at the top of the sphere, enabling alternative optical geometries and extended measurement configurations.

All ports have a diameter of 30 mm. This value was selected as a compromise between sufficient optical access and minimal disturbance of the integrating performance. Larger ports would increase radiative losses, while smaller ports would restrict beam propagation and alignment flexibility.

To evaluate the influence of the port configuration on the integrating performance, the port fraction f was considered (see Chapter 1). For the given geometry, the port fraction remains in the range of approximately 0.02–0.03 for typical measurement configurations and does not exceed 0.05 even in extended configurations [13, 14]. This

https://doi.org/10.7795/110.20260928

ensures that multiple internal reflections dominate over radiative losses through the ports, allowing the sphere to operate effectively as a directional–hemispherical integrating system.

For the selected sphere diameter of 150 mm and a port diameter of 30 mm, the calculated port fraction remains within the recommended range for integrating-sphere operation even for measurement configurations involving multiple open ports [2, 3, 34]. As a result, the radiometric amplification of the sphere, described by the sphere multiplier (Chapter 1), remains sufficiently high to ensure efficient radiance build-up and stable integrating performance. In combination with the RHFS-800 surface and the gold coating, this enables effective angular redistribution of radiation at long wavelengths.

3.3.3 Integration of geometry and surface topology

In the present design, the integrating performance does not rely on a conventional diffuse coating. Instead, it results from the combined effect of three elements: the spherical cavity geometry, the RHFS-800 surface, and a high-reflectivity metallic coating.

The spherical geometry defines the radiative enclosure and governs the multiple-reflection process described by the sphere multiplier (see Chapter 1). The RHFS-800 surface introduces controlled structural features with characteristic dimensions matched to the wavelength range considered in this work, thereby promoting angular redistribution of radiation even after metallization. The gold coating provides high reflectivity and low absorption losses, ensuring that the multiple-reflection process remains effective. The approximation of diffuse-like scattering behaviour at long wavelengths is therefore achieved through the combined effect of these three elements.

This interdependence has direct implications for both design and operation. The port configuration becomes a primary radiometric parameter, since each open port introduces a perturbation of the internal radiance distribution within the sphere. Consequently, the measurement methodology - limiting the number of simultaneously open ports and closing unused ports with coated plugs - becomes an integral part of the system design.

https://doi.org/10.7795/110.20260928

Furthermore, the effective reflectivity and scattering behaviour of the internal surface are important for maintaining the applicability of integrating-sphere theory at long wavelengths. The RHFS-800 surface was selected to provide diffuse-like scattering after metallic coating, thereby supporting high effective cavity reflectivity and maintaining a sufficiently large sphere multiplier.

The present design intentionally omits internal baffles and knife-edge port geometries, which are commonly used in conventional integrating spheres to suppress direct-view contributions and reduce port-edge effects. This decision was guided by considerations of manufacturability, continuous RHFS-800 surface coverage, and compatibility with external optical components. The introduction of internal structures would interrupt the RHFS-800 surface and complicate both fabrication and coating processes.

The radiometric consequences of these simplifications are addressed experimentally. Potential systematic effects associated with port geometry and the absence of baffles are evaluated through comparison with a metrological reference setup in the validation measurements presented in Chapter 5. Since practical port geometry can introduce measurable bias in directional–hemispherical reflectance measurements, the chosen configuration is documented explicitly to support traceable uncertainty analysis and future design optimization [48].

3.4 Fabrication and Additive Manufacturing of the Integrating Sphere

The realization of the integrating sphere developed in this work requires a fabrication approach in which geometrical design, surface topology, and coating are treated as a coupled system. In contrast to conventional integrating spheres, where diffuse behaviour is achieved by applying a coating to a geometrically simple substrate, the present concept integrates the scattering functionality directly into the structural geometry of the sphere.

As a consequence, the manufacturing process is not limited to reproducing the nominal shape of the cavity, but must ensure accurate transfer of the RHFS-800 topology to the internal surface while maintaining mechanical stability and compatibility with subsequent metallization and assembly. This requirement introduces additional

https://doi.org/10.7795/110.20260928

constraints compared to standard optical fabrication, particularly with respect to surface fidelity and process-induced distortions.

The fabrication was therefore implemented as a multi-stage engineering process including CAD modelling, additive manufacturing, post-processing, vacuum metallization, and final assembly. Each step was defined by the necessity to preserve the functional internal surface, which determines the radiometric performance of the system.

The adopted workflow follows established approaches used in the fabrication of precision optical components and integrating spheres, where geometry, surface topology, and coating are considered as a unified functional system rather than independent elements [13, 14, 47].

3.4.1 Manufacturing requirements derived from FIR radiometry and RHFS-800 geometry

From a radiometric perspective, the fabrication process must satisfy several interacting requirements related to surface topology, material compatibility, and geometrical stability.

First, the RHFS-800 topology must be reproduced with high fidelity over the entire internal surface. The microstructured height field, with a characteristic amplitude on the order of 50 µm, must not be altered by smoothing, local collapses, or printing artefacts, as such deviations would directly affect the angular scattering distribution and thus the integrating performance of the sphere [33, 34].

Second, no mechanical finishing of the internal surface is permissible. Any polishing, sanding, blasting, or chemical smoothing would irreversibly modify the designed surface topology. Therefore, all post-processing operations must be restricted to external surfaces.

Third, the substrate material must be compatible with vacuum metallization processes. This includes tolerance to thermal loads during deposition and sufficient adhesion of the metallic coating required for infrared reflectivity [49, 50].

Finally, the geometry must allow precise assembly and reproducible positioning of ports. The integrating sphere is not merely a mechanical structure but a radiometric

https://doi.org/10.7795/110.20260928

system, whose performance depends on a stable internal radiance distribution and minimal disturbance by seams and interfaces [51, 52].

These requirements strongly constrain the set of feasible fabrication technologies. Several manufacturing routes were evaluated.

Subtractive machining (CNC milling) is a robust and well-established method for manufacturing smooth metallic cavities and is commonly employed in infrared optics and precision metrology hardware. However, for the RHFS-800 topology, the characteristic feature scale and strongly curved internal geometry render tool access and toolpath control impractical. Preserving high spatial frequencies on an internal curved surface would require extremely fine tool diameters and complex multi-axis machining strategies, leading to unacceptable tolerances and surface degradation. In practice, only lower-frequency surface variants such as RHFS-200 or RHFS-400 could be considered potentially manufacturable using CNC methods. The RHFS-800 topology exceeded the achievable manufacturing fidelity for this approach. Therefore, CNC machining was not suitable for fabrication of the RHFS-800 sphere geometry in the present work.

SLS (Selective Laser Sintering) printing was previously investigated for random-ball surfaces in collaboration with external partners (Fraunhofer Institute for Production Systems and Design Technology, Berlin/Brandenburg). Although SLS enables fabrication of complex geometries, it requires external infrastructure and involves comparatively long production times. These constraints limit rapid iterative design optimization and therefore made SLS less suitable for the development workflow adopted in the present work.

Metal additive manufacturing using Selective Laser Melting (SLM) was also evaluated. Test components were produced on a DMG MORI Lasertec 30 system (see Fig. 3.5). While SLM is technically capable of generating complex metallic geometries, practical limitations became apparent. Production scheduling constraints and limited industrial availability resulted in extremely long lead times; fabrication of even small test elements required nearly one year. Furthermore, realization of a full spherical structure incorporating the RHFS-800 topology would have required multiple strongly curved segments with high geometric precision and controlled surface quality. Within the project timeframe, this approach proved impractical for iterative development and reproducible fabrication.

https://doi.org/10.7795/110.20260928

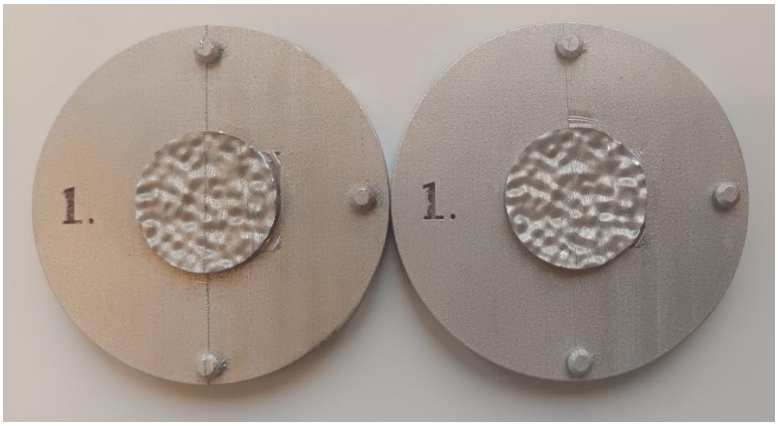


Fig. 3.5. Metallic samples fabricated by selective laser melting (SLM) with RHFS-800 topology, mounted on circular substrates.

In contrast, **stereolithography (SLA)** offers high geometric resolution and good surface fidelity for polymer components, while enabling rapid prototyping and iterative design refinement [53]. SLA is widely used for functional prototypes and precision geometries where micro-scale surface texture must be preserved [40, 54]. In the present work, the suitability of this approach was already demonstrated in the fabrication of planar RHFS samples (Chapter 2), where the required surface topology was reproduced with sufficient accuracy and successfully metallized using a reflective metallic coating.

For these reasons, SLA polymer printing was selected as the method that best combined sufficient geometric resolution, local availability, and flexibility for iterative optimization. It was therefore adopted for both prototyping and final fabrication of the sphere segments prior to metallization.

To enable fabrication, post-processing, and subsequent metallization of the internal structured surface, the sphere was designed as a set of separate segments. The final geometry has an internal diameter of 150 mm ($r_0 = 75$ mm) and a wall thickness of approximately 5 mm. This represents a compromise between structural stiffness, print stability, and manageable mass. Since the RHFS-800 topology introduces local variations of the internal surface, the wall thickness varies slightly but remains within the same order of magnitude.

In addition to the sphere structure, dedicated aluminium sample holders were developed to enable stable positioning of samples during reflectance measurements.

https://doi.org/10.7795/110.20260928

These holders were manufactured from aluminium and mounted externally at the corresponding ports, as shown in Fig. 3.6. The design ensures reproducible positioning of the sample relative to the sphere geometry and allows secure mechanical fixation without affecting the internal structured surface. It should be noted that the present holder design is suitable for reflectance measurements only and is not compatible with transmittance configurations.

The final configuration consists of six spherical segments, removable port plugs, and integrated alignment features ("puzzle-type" interlocks) to ensure reproducible positioning during assembly while preserving the integrity of the internal structured surface. The spherical segments and removable plugs were fabricated by SLA printing, while the external mounting elements and sample holders were manufactured separately from aluminium. Such a segmented construction is consistent with established design principles for precision optical cavities, where accessibility of functional surfaces and assembly reproducibility are critical parameters [14, 45, 47].

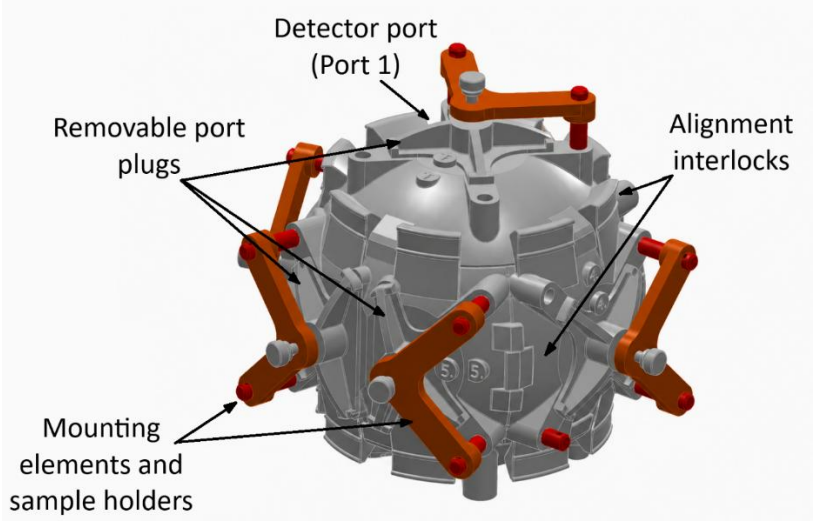


Fig. 3.6. CAD model of the integrating sphere assembly showing the SLA-printed spherical segments, removable port plugs, aluminium mounting elements and sample holders, integrated alignment interlocks.

3.4.2 Additive manufacturing process

All structural components were fabricated using SLA with a Formlabs Form 2 printer and Tough 1500 photopolymer resin. This material was selected due to its high

https://doi.org/10.7795/110.20260928

dimensional accuracy, fine layer resolution, reproducibility of structured surface topologies, and compatibility with subsequent vacuum metallization processes [40, 54].

As a first step, a segmented prototype of the integrating sphere was manufactured in order to establish a reliable process chain. The objective of this prototype was to investigate practical aspects of fabrication, including part orientation, support strategy, cleaning procedures, handling, and dimensional stability across multiple segments. The assembled prototype is shown in Fig. 3.7.



Fig. 3.7. Photograph of the segmented prototype of the integrating sphere assembled from printed SLA segments, illustrating the modular structure and port configuration.

The prototype segments were manufactured with tongue-and-groove style alignment ("puzzle-type" interlocks), ensuring reproducible positioning during assembly. The alignment is defined by the geometry of the segment interfaces and integrated port features. Importantly, the prototype was assembled without adhesive; mechanical integrity was achieved by combining the alignment geometry with metallic clamping rings at the top and bottom. This approach enabled repeated assembly and disassembly, allowed inspection and reworking of individual segments, and reduced the risk of damage to the functional surface during iterative handling [52, 55].

The prototype served to evaluate mechanical assembly feasibility, dimensional tolerances, stability of the segmentation approach, and compatibility with sample holders and accessory components. The results confirmed that the segmented design provides reliable alignment and sufficient structural integrity. Based on these findings, the fabrication process was transferred to the final sphere configuration. The use of

https://doi.org/10.7795/110.20260928

prototype-based validation is consistent with established engineering practice in precision optical instrumentation and additive manufacturing workflows [40, 56, 57].

Considering the specific characteristics of SLA fabrication, the sphere was divided into six segments in a defined manner. This segmentation reflects not only printer volume constraints but also process-related aspects such as deformation behaviour, support placement, and handling during post-processing.

Several process-related aspects were identified as critical for successful fabrication. Surface fidelity depends strongly on part size, as larger SLA components exhibit an increased risk of warping, local distortions, and surface defects due to peel forces and resin flow dynamics during printing [40, 58]. The support strategy was particularly critical, since the internal RHFS surface had to remain completely free of support structures. Therefore, each segment was oriented with the structured inner surface facing downward towards the resin bath, while the outer surface faced upward towards the build platform. In this configuration, all supports were attached exclusively to the external surfaces, preventing any modification of the functional internal surface topology.

Segmentation also simplifies handling and cleaning during post-processing, since each segment can be processed individually with reduced mechanical stress, thereby minimizing the risk of damage to the functional internal surface. In addition, the presence of openings in the segment geometry improves printing reliability. Such openings facilitate resin drainage and reduce suction effects during the peeling process, which can otherwise lead to deformation or print failure. The final segment dimensions were approximately 120 mm × 140 mm, and each segment contained one or two openings. The segment geometry is illustrated in Fig. 3.8.

The internal RHFS surface was intentionally left completely untreated in order to preserve the printed topology as the functional scattering surface. All finishing operations were restricted to external surfaces only. These measures are essential for preserving the geometric fidelity of the RHFS-800 topology, since any unintended surface modification would directly affect the angular scattering behaviour and, consequently, the radiometric performance of the integrating sphere [40, 58, 59, 60].

After printing, standard SLA post-processing was performed, including cleaning and curing according to the established workshop procedure. The internal RHFS-

https://doi.org/10.7795/110.20260928

800 surface was left untreated in order to preserve the functional topology. The segments were then prepared for subsequent vacuum metallization.

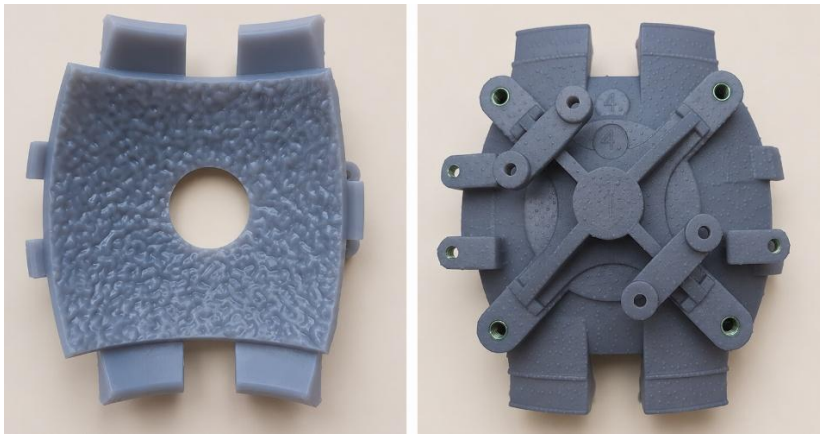


Fig. 3.8. Photographs of an SLA-printed integrating sphere segment: (a) inner side with RHFS-800 surface and integrated port opening; (b) outer side with removable port plug.

3.4.3 Metallization and gold coating

To achieve high reflectivity in the far-infrared spectral range, the polymer substrate was metallized by vacuum deposition. The metallization was performed by CREAVAC GmbH, a company specializing in vacuum coating technologies for optical and technical applications [61].

In infrared optics and metrology, gold coatings are widely used due to their high reflectivity from the mid-infrared to the far-infrared spectral range [2, 39, 62]. For polymer substrates, the application of an adhesion layer is typically required to ensure mechanical stability of the metallic film [2, 49].

The implemented coating stack consisted of a NiCr adhesion layer with a thickness of approximately 40–50 nm, followed by a gold coating with a nominal thickness of approximately 220–250 nm.

Due to the complex geometry of the components and the limited thermal resistance of the polymer substrate, the coating process could not be performed as a standard continuous deposition run. Instead, the process was carried out in multiple stages in order to limit the thermal load on the substrate to approximately 60 °C. Such process partitioning is consistent with established practice in vacuum coating of thermally

https://doi.org/10.7795/110.20260928

sensitive materials, where temperature control is required to prevent deformation, residual stress, or degradation of the substrate [49].

Process validation was performed in several stages. Initially, a representative printed component corresponding to the curved test segment described in Section 3.2 (Fig. 3.2) was coated in order to verify the feasibility of uniform metallization for this geometry. The central circular feature visible in Fig. 3.9 corresponds to a closed 30 mm port with a removable plug and illustrates the internal appearance of a closed port. Due to its pronounced curvature and structured internal surface, this segment represented a suitable test geometry for evaluating coating homogeneity both inside the cavity region and near the segment edges. The result of this coating step is shown in Fig. 3.9.

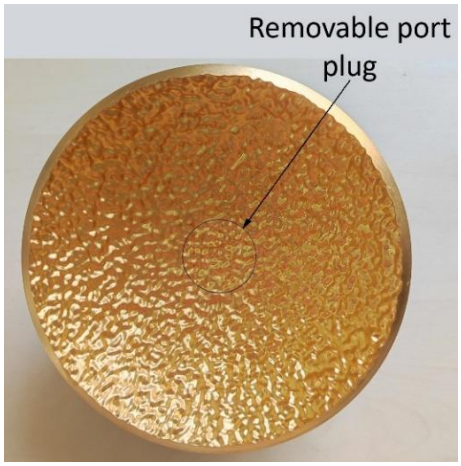


Fig. 3.9. Photograph of the curved RHFS-800 test segment after gold coating, used for initial validation of the metallization process. The circular feature in the central region indicates the internal appearance of a closed 30 mm port with a removable plug.

Following this feasibility step, additional test components were provided to the coating facility to assess adhesion and coating quality under the given process conditions. After successful qualification, the coating process was scaled to the full set of sphere segments. The final coating was performed using a larger deposition system capable of processing multiple components simultaneously, ensuring consistent metallization of all segments. The resulting coated components are shown in Fig. 3.10.

For independent characterization of the coating thickness and optical properties, a planar reference sample with a diameter of 50 mm was fabricated and coated within the same deposition batch as the sphere components. It was produced using the same additive manufacturing and metallization route as the sphere components. The visible

https://doi.org/10.7795/110.20260928

fine surface texture originates from the unpolished printed substrate. The sample was used as a representative coated surface for evaluating the deposited gold layer, verifying the coating process, and enabling reproducible positioning in the PTB reference measurement setup. The coated planar sample is shown in Fig. 3.11.

(a)



(b)



Fig. 3.10. Photographs of the fabricated integrating sphere segments with gold-coated internal surfaces and corresponding port plugs, showing (a) inner and (b) outer sides prior to final assembly.



Fig. 3.11. Photograph of the gold-coated planar reference sample with a diameter of 50 mm used for independent optical characterization and verification of the coating process. The visible fine surface texture originates from the unpolished additively manufactured substrate.

https://doi.org/10.7795/110.20260928

3.4.4 Gold coating physics and optical behaviour

The radiometric performance of the integrating sphere is strongly influenced by the effective reflectance of the metallic coating applied to the RHFS-800 surface. While the structured surface governs the angular redistribution of radiation, absorption losses within the metallic layer determine the efficiency of the multiple-reflection process inside the cavity.

As discussed in Chapter 2, the interaction of infrared radiation with the metallic coating is governed by the skin-effect regime. For the wavelength range considered in this work, the electromagnetic penetration depth remains significantly smaller than the thickness of the deposited gold layer. Consequently, the optical response is determined predominantly by the metallic coating rather than by the underlying polymer substrate.

This condition is essential for the present integrating-sphere concept, since it ensures that the cavity reflectance is governed primarily by the optical properties of gold, while the RHFS-800 surface provides diffuse-like angular redistribution of radiation. The resulting combination of high reflectivity and diffuse-like scattering forms the physical basis of the integrating performance at long wavelengths [1, 21, 63].

The optical suitability of the deposited coating was verified using the gold-coated planar reference sample shown in Fig. 3.11. The sample was not intended to reproduce the RHFS-800 surface topology. Instead, it was used to characterize the directional spectral emittance, and thus the absorption losses, of the gold coating deposited on the sphere components. A planar reference geometry was used because the EMAF measurement configuration requires reproducible positioning of the sample surface within a defined measurement area and observation geometry. The structured RHFS-800 sphere wall could not be measured directly in this setup. Therefore, the planar reference sample was used to characterize the coating itself, while the diffuse-like angular redistribution provided by the RHFS-800 topology was evaluated separately in Chapter 2.

The directional spectral emittance of the coating was investigated at PTB using the Emissivity Measurements in Air Facility (EMAF), which is designed for traceable spectral emittance measurements in the infrared and far-infrared spectral range [21, 64]. The planar reference sample positioned in the EMAF facility is shown in Fig. 3.12. Measurements were performed at a sample temperature of 80 °C and observation

https://doi.org/10.7795/110.20260928

angles of 20°, 30°, 50°, 60°, and 70°. For highly reflecting samples such as gold-coated mirrors, the 10° EMAF configuration is affected by direct back-reflection into the optical path and is therefore not used for the evaluation. Consequently, the 20° dataset represents the smallest reliable observation angle available for the present gold-coated reference sample and was selected for deriving the coating reflectance. The investigated spectral range extended from 100 cm^{-1} to 600 cm^{-1}, corresponding to wavelengths from 100 µm to 16.7 µm.

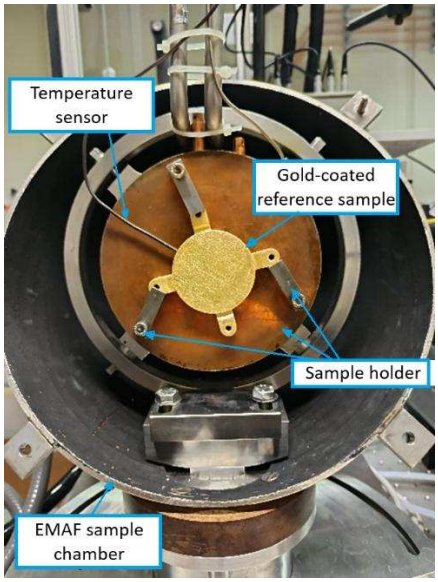


Fig. 3.12. Photograph of the gold-coated planar reference sample positioned in the EMAF facility for spectral emittance measurements. The gold-coated reference sample, sample holder, temperature sensor, and EMAF sample chamber are indicated.

The resulting directional spectral emittance spectra are shown in Fig. 3.13. For all investigated observation angles, the emittance remains low over the spectral range considered, indicating high optical quality of the deposited gold coating. A moderate angular dependence is observed, but the overall emittance level remains sufficiently low to support efficient multiple reflections inside the integrating-sphere cavity.

For the opaque gold-coated sample, the corresponding spectral reflectance can be derived from the measured spectral emittance using the relation introduced in Chapter 1. For the dataset measured at an observation angle of 20°, the resulting reflectance values are approximately 0.98–0.99 over the investigated far-infrared spectral range. These values are consistent with literature data for vacuum-deposited gold coatings [2, 62, 39].

https://doi.org/10.7795/110.20260928

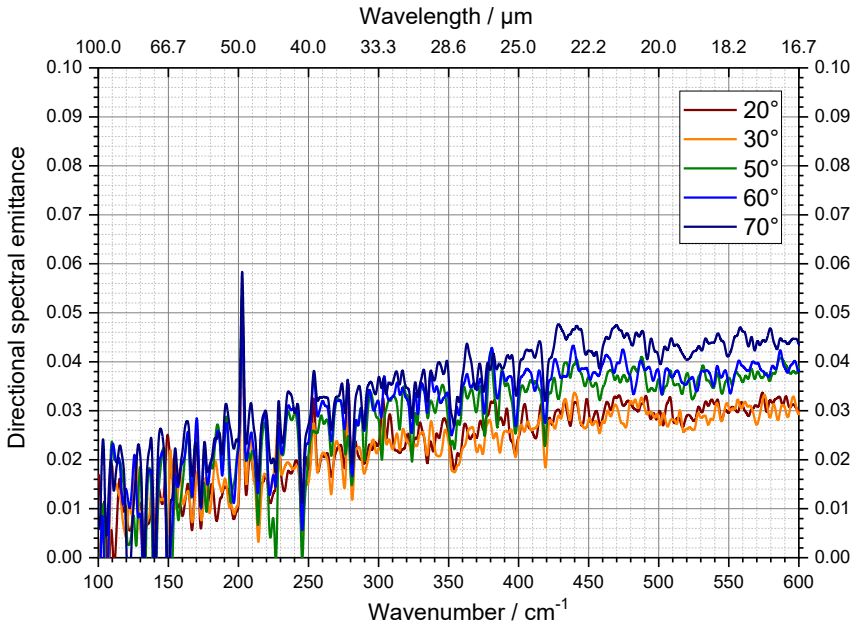


Fig. 3.13. Directional spectral emittance of the gold-coated planar reference sample measured in the EMAF facility at $T = 80°C$ for observation angles of 20°, 30°, 50°, 60°, and 70°.

The low measured emittance and the corresponding high reflectance indicate that the deposited coating provides sufficiently low absorptance to support efficient multiple reflections inside the integrating-sphere cavity. In combination with the spherical cavity geometry and the RHFS-800 surface topology, the high-reflectivity gold coating therefore forms the low-loss reflective boundary required for stable integrating performance and efficient angular redistribution within the cavity.

3.4.5 Outgassing and material suitability

To evaluate the possibility of future operation of the integrating sphere under vacuum or reduced-pressure conditions, additional material qualification tests were performed. For this purpose, a gold-coated RHFS-400 test sample fabricated from the same photopolymer material was investigated using mass spectrometry in order to assess outgassing behaviour. The measurement sample positioned in the vacuum chamber is shown in Fig. 3.14.

The corresponding mass spectrometry results are presented in Fig. 3.15. The detected species included H_2O, N_2, O_2, CO_2, short-chain hydrocarbons, acrylates, and styrene. All detected components were present at non-critical concentrations. In addition, one printed and metallized component was stored under vacuum over an extended

https://doi.org/10.7795/110.20260928

period in order to evaluate possible structural or chemical degradation effects. No measurable degradation or instability was observed during these tests.

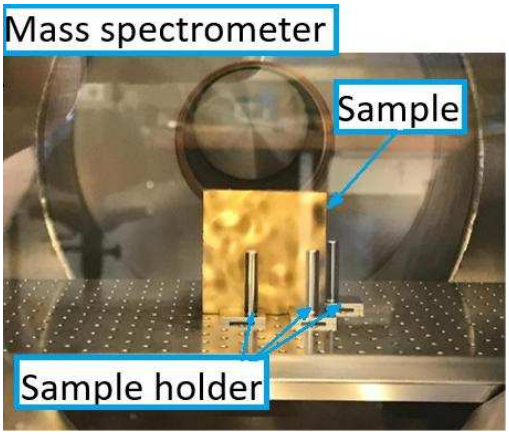


Fig. 3.14. Photograph of the gold-coated RHFS-400 test sample positioned in the vacuum chamber for mass-spectrometry-based outgassing analysis.

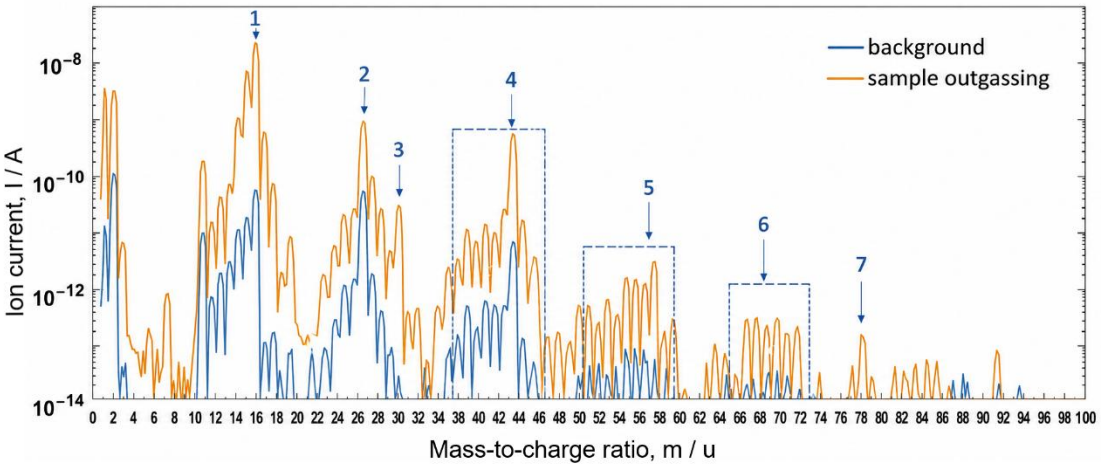


Fig. 3.15. Mass spectrometry results of the outgassing analysis of the gold-coated RHFS-400 sample. Detected species include 1 - H_2O, 2 - N_2, 3 - O_2, 4 - CO_2, 5 - short-chain hydrocarbons, 6 - acrylates, and 7 - styrene.

Although the final measurement configurations presented in this work were implemented in dry air at room temperature, the performed outgassing studies indicate the general suitability of the selected material and metallization process for optical instrumentation under reduced-pressure conditions. Such qualification procedures are consistent with established practice for vacuum-compatible polymer materials and optical coating systems [65, 66].

https://doi.org/10.7795/110.20260928

3.4.6 Final assembly, development outcome and relevance to FIR integrating-sphere realization

After metallization, mechanical post-processing was restricted to external and interface surfaces in order to prepare the coated segments for final assembly. The gold-coated internal RHFS-800 surface was not mechanically processed. Rounded external surfaces were polished to improve handling and assembly, while flat interface surfaces at the ports and sample-holder positions were milled to provide geometrically flat reference planes aligned normal to the radial direction of the sphere. This ensured reproducible mounting of port components and sample holders without modifying the functional internal surface. The polishing holder used for controlled post-processing is shown in Fig. 3.16.

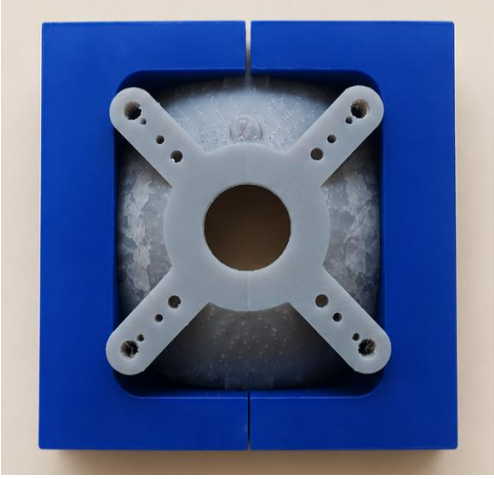


Fig. 3.16. Photograph of an integrating sphere segment mounted in a dedicated fixture for controlled and repeatable polishing of the external surfaces after metallization.

To avoid introducing geometric bias, dedicated fixtures were manufactured to hold the segments at defined orientations, enabling controlled and repeatable post-processing. This step is important in precision opto-mechanics, as external dimensional stability and reproducible positioning directly influence assembly accuracy and experimental reproducibility [52]. Threaded interfaces and mounting elements were locally reinforced to ensure mechanical reliability while maintaining the structural integrity of the polymer material.

Following this post-processing step, the final sphere was assembled using the integrated tongue-and-groove alignment geometry of the individual segments. This

https://doi.org/10.7795/110.20260928

“puzzle-type” configuration ensured reproducible positioning and minimized seam discontinuities between neighbouring parts. Once the segments had been mechanically aligned, epoxy adhesive (3M Epoxy Adhesive 2216 Grey) was applied to the segment interfaces to permanently stabilize the structure.

The adhesive was selected based on its mechanical stability, compatibility with the assembly requirements, and suitability for aerospace applications. To reduce trapped air introduced during mixing, the two-component adhesive was degassed under vacuum for approximately 10 min prior to application. Following bubble release, the adhesive was applied to the prepared interfaces during final assembly.

Importantly, the port plugs were not bonded permanently. Instead, the sphere was designed as a modular system in which the plugs are mounted using dedicated holders and mechanical fixtures. This modularity is essential for radiometric operation, since different measurement configurations require varying port states and repeated exchange of reference and sample holders. In addition, unused ports must be closed using coated plugs in order to minimize radiative losses and preserve the integrating performance of the cavity [14, 51, 67].

Once bonded, the sphere was left to cure under controlled conditions until full mechanical stability was achieved. After assembly and integration of the external components, the completed integrating sphere system, hereafter referred to as FIR-IS (Far-Infrared Integrating Sphere), was realized. The resulting FIR-IS constitutes a complete integrating sphere system in which the RHFS-800 surface is implemented throughout the internal cavity and the continuous metallic coating provides the high-reflectivity boundary condition required for operation at long wavelengths.

The final configuration of the sphere with open measurement ports is shown in Fig. 3.17, while the configuration equipped with external aluminium sample holders for reflectance measurements is presented in Fig. 3.18. These external holders represent the implemented reflectance sample-mounting configuration. They allow flat samples with diameters from 30 mm to 100 mm and thicknesses up to 25 mm to be mounted reproducibly at the measurement ports. The essential geometrical requirement is that the sample fully covers the 30 mm measurement port and can be fixed with sufficient mechanical stability. Larger samples or samples with different shapes can be accommodated by adapting the holder geometry, since the sample size is not intrinsically

https://doi.org/10.7795/110.20260928

limited by the integrating sphere itself. Thin films or flexible samples require suitable support frames or auxiliary fixation to ensure complete port coverage and reproducible positioning.

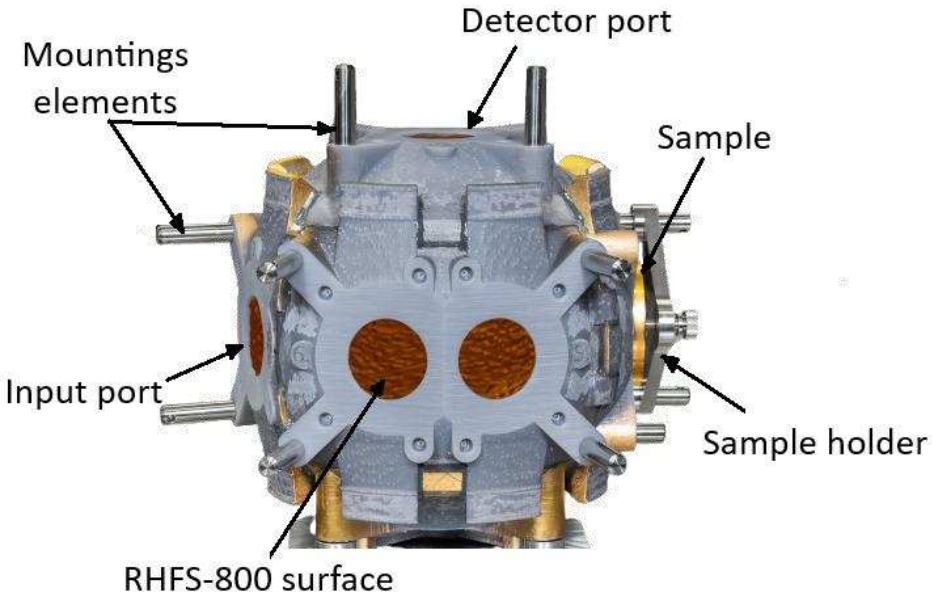


Fig. 3.17. Photograph of the final FIR-IS system with open measurement ports.

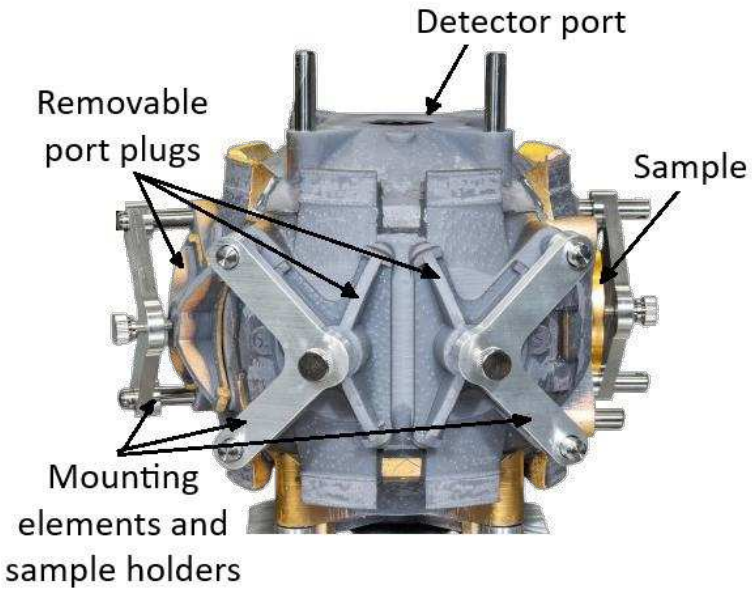


Fig. 3.18. Photograph of the final FIR-IS system equipped with external aluminium mounting elements and sample holders for reflectance measurements.

https://doi.org/10.7795/110.20260928

The completed FIR-IS represents the outcome of an extended engineering development process involving iterative prototyping, fabrication optimization, metallization validation, and assembly refinement. A major challenge throughout this process was the stabilization of printing parameters, segmentation strategy, and handling procedures required to preserve the functional internal scattering surface.

The fabrication chain established in this work shows that a structured scattering surface for long-wavelength applications can be reproducibly realized over a full integrating-sphere cavity using SLA fabrication. Furthermore, the functional surface can remain completely unprocessed after printing, thereby preserving the designed scattering behaviour. The work also shows that vacuum metallization using an adhesion layer and a sufficiently thick gold coating can be reproducibly applied to polymer-based structured components under controlled thermal conditions.

Unlike conventional integrating spheres manufactured from smooth substrates with diffuse coatings, the present design incorporates the scattering functionality directly into the structural geometry itself. As a consequence, the optical behaviour of the FIR-IS is primarily defined by the interaction between geometry, the RHFS-800 surface, and metallic reflectivity. This fabrication strategy addresses an important practical gap in long-wavelength integrating-sphere technology by enabling cavity-scale realization of structured geometries that cannot be achieved using conventional machining or coating-on-smooth-substrate approaches.

https://doi.org/10.7795/110.20260928

Chapter 4. Development of the Optical Measurement Setup

This chapter describes the development of the optical system that enables the FIR-IS to operate in combination with a FTIR spectrometer for directional–hemispherical reflectance and transmittance measurements.

Because the FIR-IS cannot be positioned directly inside the spectrometer sample compartment, a dedicated external optical coupling system was developed. The system guides radiation from the spectrometer to the sphere and subsequently returns the hemispherically collected radiation back to the detector path while preserving optical throughput [14, 27, 37].

The resulting configuration forms a unified radiometric instrument consisting of the spectrometer, the integrating sphere, and an external optical relay system enabling bidirectional beam propagation between both subsystems.

Particular attention was devoted to preservation of optical throughput, since the available radiometric power at long wavelengths is limited and the external optical relay system introduces additional geometrical constraints. Therefore, the design of the optical setup was based on throughput conservation, aperture matching, and compatibility between the spectrometer optics and the integrating-sphere geometry.

The chapter first describes the throughput constraints governing the optical design and the corresponding optimization of mirror diameters, focal lengths, and aperture geometry. Subsequently, the implementation of the external optical relay system, including beam extraction and reinjection using the Bruker A515 unit, is presented. Finally, the environmental enclosure and thermal stabilization of the measurement system are described.

4.1 Throughput Preservation and Aperture Matching

The external optical relay system enables transfer of radiation between the FTIR spectrometer and the integrating sphere. However, geometrical beam transport alone is insufficient to ensure efficient radiometric operation of the complete setup. In Fourier-transform infrared spectroscopy, the achievable detector signal is fundamentally

https://doi.org/10.7795/110.20260928

limited by the optical throughput (étendue) of the optical system [68]. Consequently, the external optical assembly must preserve the intrinsic throughput of the spectrometer while simultaneously adapting the beam geometry to the integrating-sphere ports and the external optical relay geometry [27, 28, 37, 62, 67].

The optical throughput (étendue) of a radiation beam is defined as

$$G = A_{beam}\Omega \qquad (4.1)$$

where A_{beam} denotes the beam cross-sectional area and Ω the solid angle subtended by the radiation cone. In passive optical lsystems without absorption or beam clipping, étendue remains conserved along the optical path [37, 69, 70]. Any restriction of beam diameter or angular acceptance therefore leads to irreversible reduction of optical throughput and consequently to decreased detector signal.

The FTIR spectrometer allows selection of different aperture diameters at the sample position. In principle, the aperture can be varied over a broad range depending on the required signal level and spectral resolution. However, in the present setup the maximum admissible aperture is additionally constrained by the geometry of the external optical relay system and the integrating sphere.

As described in Chapter 3 (Section 3.3), the integrating sphere employs ports with diameters of 30 mm determined by the geometrical design of the sphere and its radiometric operating conditions. These ports determine the maximum admissible beam diameter and angular acceptance for radiation entering and leaving the sphere [10, 13, 14]. If the propagated beam exceeds these geometrical limits, partial clipping occurs either at the sphere ports or at intermediate optical elements of the relay system, leading directly to throughput reduction and signal losses.

Consequently, the spectrometer aperture, mirror diameters, and focal lengths of the external optical system had to be selected jointly such that the propagated beam remained compatible with the complete optical geometry of the setup. The beam emerging from the spectrometer must first be accepted by the initial off-axis parabolic mirror without truncation, subsequently transported through the complete mirror relay system without clipping at intermediate mirrors, and finally focused through the integrating-sphere entrance port while preserving the required illumination geometry at the

https://doi.org/10.7795/110.20260928

internal sample position. Simultaneously, the detected radiation path must remain compatible with the detector-side relay optics and the return path toward the spectrometer.

The optical geometry is additionally constrained by the finite divergence of the beam exiting the external beam extraction interface. Because the beam possesses a defined focal region, its diameter changes continuously along the optical path. The dimensions and focal lengths of all mirrors therefore directly influence both the propagated beam diameter and the corresponding angular acceptance throughout the relay system. In addition, the geometry of the integrating sphere imposes further restrictions on the admissible beam envelope because radiation must pass through the 30 mm sphere ports without partial beam clipping while simultaneously maintaining the required focal geometry at the sample position and detector-side port.

Because the optical system consists of multiple coupled optical stages with different focal lengths, beam diameters, and geometrical constraints, analytical estimation alone was insufficient for reliable optimization of the complete relay geometry. Therefore, numerical propagation of étendue through the complete optical system was implemented in Mathematica. The calculation included the internal spectrometer optics, the external beam extraction and return interface, the complete external mirror relay system, and the integrating-sphere ports. At each optical stage, beam diameter and angular acceptance were recalculated under the condition of étendue conservation.

The numerical propagation was performed sequentially along the complete optical path beginning at the Globar source and the spectrometer aperture. The calculation subsequently included the internal spectrometer optics, propagation through the external beam extraction interface, transfer through all mirrors of the external optical relay system, passage through the integrating-sphere ports, and focusing at the sample position. The detected radiation path was analysed analogously in the reverse direction toward the detector path of the spectrometer.

For every optical stage, the beam diameter and the associated solid angle were recalculated while enforcing conservation of étendue. This procedure allowed determination of the admissible beam envelope throughout the complete optical system and verification that no geometrical clipping occurred either at intermediate mirrors or at the sphere ports. The calculations additionally enabled optimization of mirror

https://doi.org/10.7795/110.20260928

diameters and focal lengths while preserving compatibility between the spectrometer optics and the integrating-sphere geometry.

The numerical analysis demonstrated that the maximum spectrometer aperture compatible with the complete optical system is 3 mm. Larger apertures lead to partial beam clipping within the external relay system and at the integrating-sphere entrance port, resulting in reduced throughput and decreased detector signal levels. Smaller apertures remain fully compatible with the optical geometry but reduce the available radiometric power.

The calculations further demonstrated that focal lengths of 120 mm and 220 mm provide efficient beam transfer between the spectrometer and the integrating sphere while maintaining compatibility with the geometrical constraints imposed by the 30 mm sphere ports. Correspondingly, mirror diameters of 30 mm were found to represent the minimum dimensions compatible with loss-free beam transport throughout the complete optical relay system. Oversized mirrors would not increase throughput because the system remains fundamentally limited by the spectrometer aperture, whereas undersized mirrors would introduce clipping losses and reduce the transported optical power.

Maintaining étendue conservation is particularly important at long wavelengths, where the available radiometric power is limited and detector noise becomes significant. The developed optical system therefore preserves optical throughput while maintaining compatibility with the integrating-sphere geometry and minimizing radiometric losses. This enables external operation of the integrating sphere while maintaining stable radiometric conditions and reproducible measurement geometry comparable to conventional internal FTIR configurations [27, 67, 71, 72].

4.2 Optical Path Design

Based on the throughput constraints and geometrical requirements described in Section 4.1, an external optical relay system was developed for coupling the FTIR spectrometer to the integrating sphere.

The optical coupling is based on the Bruker A515 external reflection unit, which enables the interferometer beam to exit the spectrometer housing, propagate through

https://doi.org/10.7795/110.20260928

an external optical system, and subsequently re-enter the instrument after interaction with the integrating sphere [27, 71, 72].

Because the A515 unit alone does not provide sufficient geometrical flexibility for direct coupling to the integrating sphere, an additional optical relay system was implemented. This relay consists of flat and off-axis parabolic mirrors that transfer, shape, collimate, and refocus the radiation beam between the spectrometer and the integrating sphere while preserving the optical characteristics of the interferometer beam. Off-axis parabolic mirrors were selected because they enable broadband aberration-free collimation and focusing without introducing chromatic dispersion, which is particularly important for broadband infrared radiation [37, 69, 70].

The resulting configuration forms a bidirectional optical relay system connecting the spectrometer and the integrating sphere. A schematic representation of the complete setup is shown in Fig. 4.1.

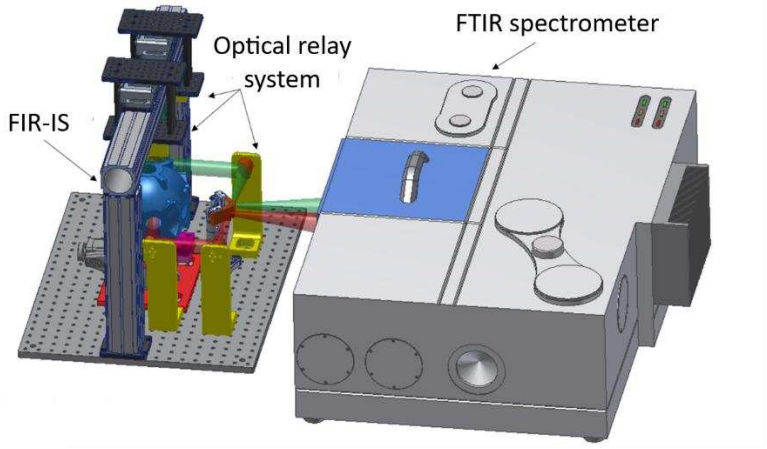


Fig. 4.1. Engineering implementation of the complete external FTIR–integrating-sphere system, including the FTIR spectrometer, the external optical relay system, and the FIR-IS. The red and green beam paths indicate the incident radiation path from the spectrometer to the sphere and the detected radiation path returning from the sphere to the detector system, respectively.

4.2.1 Optical function of the A515 unit

The external optical coupling is based on the Bruker A515 reflection unit, which serves as an interface between the FTIR spectrometer and the external optical relay system. The unit contains an internal reflective arrangement enabling the interferometer beam to exit the spectrometer housing, propagate through the external optical relay

https://doi.org/10.7795/110.20260928

system, and subsequently re-enter the instrument after interaction with the integrating sphere.

External beam-transfer units of this type are commonly employed in FTIR spectroscopy for coupling interferometers to custom experimental systems while preserving spectral integrity and optical alignment [27, 28, 37, 71, 72]. A photograph of the Bruker A515 unit is shown in Fig. 4.2.

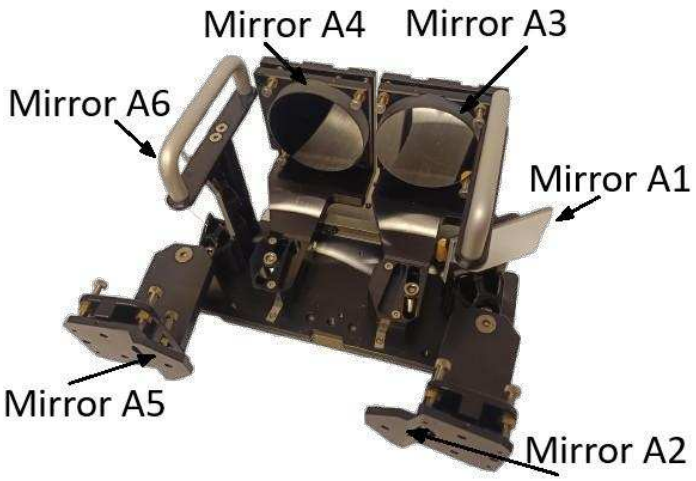


Fig. 4.2. Photograph of the Bruker A515 external reflection unit used for extraction and reinjection of the interferometer beam between the FTIR spectrometer and the external optical relay system. The internal folding mirrors A1–A6 are indicated; mirrors A3 and A4 were primarily used for angular adjustment of the separated beam paths.

In its standard configuration, the A515 unit produces a single converging beam shared by both the incident and detected radiation paths. However, operation with the integrating sphere requires spatial separation between the incident radiation path directed toward the sphere and the detected radiation path returning from the sphere.

To achieve this separation, controlled angular adjustment of the internal folding mirrors inside the A515 unit was performed. The main adjustment was carried out using the central folding mirrors A3 and A4 indicated in Fig. 4.2, while the remaining mirrors were used for fine optimization of the beam position and angular alignment. This alignment adjustment laterally separated the incident and detected beams by 30 mm while maintaining optical conjugation with the interferometer focus.

https://doi.org/10.7795/110.20260928

This alignment adjustment produces two distinct but optically matched radiation paths:

- the incident radiation path directed toward the integrating sphere (red),
- the detected radiation path returning from the integrating sphere toward the detector system (green).

The resulting internal beam routing inside the FTIR spectrometer is illustrated schematically in Fig. 4.3.

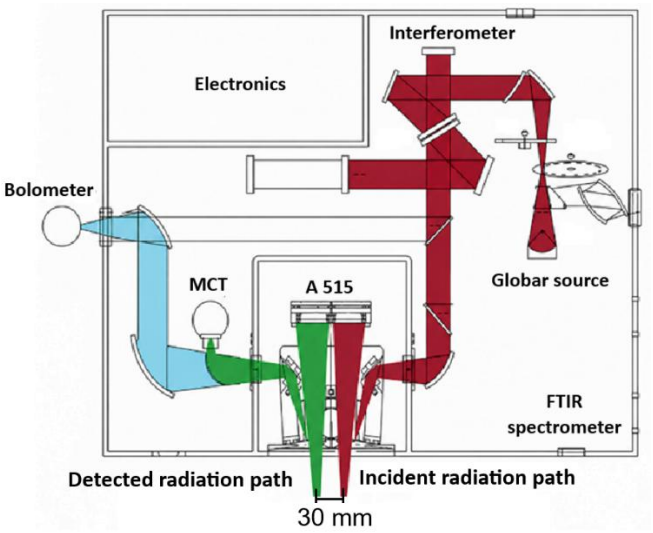


Fig. 4.3. Schematic representation of the internal radiation paths inside the FTIR spectrometer after alignment adjustment of the A515 unit. The incident and detected radiation paths are spatially separated while remaining optically conjugated with the interferometer.

4.2.2 Incident radiation path

The radiation path between the FTIR spectrometer and the integrating sphere is realized by an external mirror-based relay system. The optical assembly consists of one flat mirror (Mirror 1-1) and two off-axis parabolic (OAP) mirrors, denoted as Mirror 1-2 and Mirror 1-3.

The incident radiation originates from the Globar source of the spectrometer and is guided through the A515 unit into the external optical system. The beam exiting the A515 unit possesses a defined focal point and therefore forms a converging beam.

https://doi.org/10.7795/110.20260928

The first optical element of the incident radiation path is the flat mirror Mirror 1-1 with dimensions of 50 mm × 24.5 mm × 10 mm, positioned at an angle of 45°. This mirror is located directly before the focal region of the A515 output and redirects the radiation toward the first off-axis parabolic mirror while preserving the focusing geometry.

Mirror 1-2 has a diameter of 30 mm, an off-axis angle of 90°, and a focal length of $f_{focal} = 120$ mm. The focal region of the A515 output was matched to the focal point of Mirror 1-2. As a result, the diverging beam originating from the A515 focus is transformed by Mirror 1-2 into a collimated beam.

The collimated radiation is subsequently transferred to Mirror 1-3, which has a diameter of 30 mm, an off-axis angle of 98°, and a focal length of $f_{focal} = 220$mm. Mirror 1-3 refocuses the radiation through the 30 mm entrance port of the integrating sphere toward the internal sample region located on the opposite inner wall of the sphere.

The optical geometry was adjusted such that the incident radiation reaches the sample under an angle of 8° relative to the surface normal, corresponding to the directional–hemispherical measurement configuration implemented in the present work. A schematic representation of the incident radiation path is shown in Fig. 4.4.

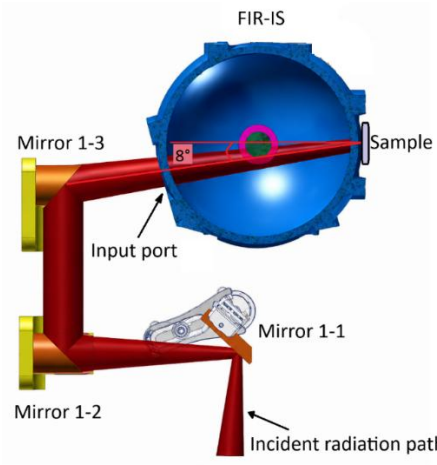


Fig. 4.4. Optical configuration of the incident radiation path between the A515 unit and the integrating sphere. Mirror 1-1 redirects the beam toward the off-axis parabolic mirrors Mirror 1-2 and Mirror 1-3, which collimate and refocus the radiation into the sphere. The beam is focused onto the sample position inside the sphere at an incidence angle of 8° relative to the sample normal.

https://doi.org/10.7795/110.20260928

The focal plane of Mirror 1-3 was positioned at the internal sample location inside the integrating sphere, ensuring reproducible illumination geometry within the sphere cavity. The resulting measurement spot at the sample position had an estimated diameter of 12 mm.

4.2.3 Detected radiation path

After interaction with the sample, the radiation undergoes multiple diffuse reflections inside the integrating sphere and subsequently exits through the detector port located at the upper part of the sphere.

The first optical element of the detected radiation path is the off-axis parabolic mirror Mirror 2-5 positioned directly above the detector port. The mirror possesses a diameter of 30 mm, an off-axis angle of 90°, and a focal length of f_{focal} =220 mm. Its focal plane was positioned on the inner surface of the integrating sphere opposite the detector port, enabling efficient collection of the hemispherically integrated radiation emerging from the sphere aperture.

Mirror 2-5 transforms the diverging radiation emerging from the detector port into a collimated beam. The collimated beam is subsequently redirected by the circular flat mirror Mirror 2-4, which deflects the radiation downward by 90°.

After vertical propagation, the beam is redirected again by the second circular flat mirror Mirror 2-3 toward the lower part of the optical relay system.

The subsequent focusing stage is realized using the off-axis parabolic mirror Mirror 2-2, which has a diameter of 30 mm and a focal length of $f_{focal} = 120$ mm. This mirror focuses the detected radiation toward the entrance region of the A515 unit.

Immediately before re-entering the A515 module, the beam is redirected by the final flat mirror Mirror 2-1 with dimensions of 50 mm × 24.5 mm × 10 mm. The radiation then propagates through the A515 unit back into the FTIR spectrometer and subsequently toward the detector system. A schematic representation of the detected radiation path is shown in Fig. 4.5.

https://doi.org/10.7795/110.20260928

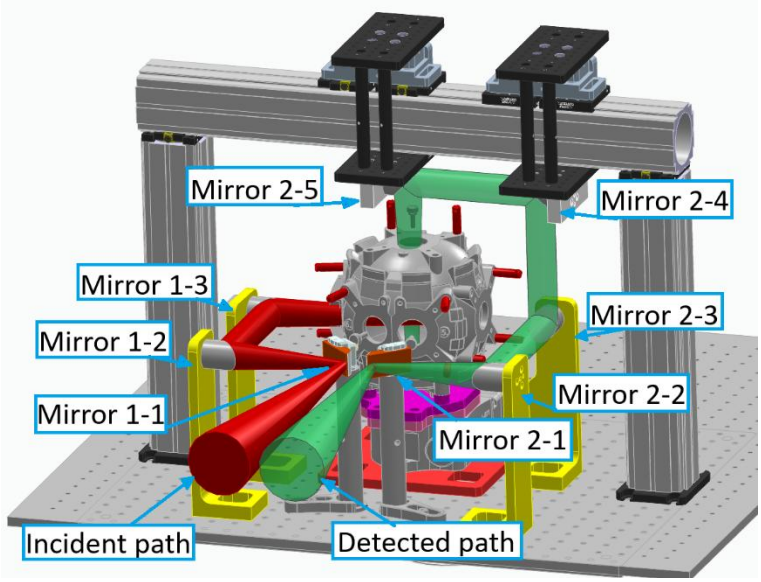


Fig. 4.5. Optical configuration of the external mirror relay system showing the incident radiation path entering the integrating sphere (red) and the detected radiation path leaving the sphere through the detector port (green). Mirrors 2-5, 2-4, 2-3, 2-2, and 2-1 guide and refocus the detected radiation within the relay system.

4.2.4 Optical relay implementation

The external optical relay system was designed such that comparable beam-transformation conditions are obtained for both the incident and detected radiation paths. For this purpose, the optical system employs partially symmetric off-axis parabolic mirror pairs. Mirrors 1-2 and 2-2 both use focal lengths of 120 mm, whereas Mirrors 1-3 and 2-5 use focal lengths of 220 mm. This configuration ensures consistent collimation and refocusing behaviour in both propagation directions and simplifies optical alignment of the overall system. The overall geometry of the optical relay system is illustrated in Fig. 4.5.

All mirrors used in the setup, including both flat and off-axis parabolic mirrors, were manufactured from aluminium alloy EN AW-6061-T6 and coated with protected gold. This material combination is widely used in infrared optical engineering because of its favourable balance of machinability, thermal stability, and high infrared reflectance [62].

https://doi.org/10.7795/110.20260928

The reflective gold coating was protected by a dielectric Y_2O_3 layer in order to reduce oxidation, mechanical degradation, and environmental contamination while preserving high optical performance over the infrared spectral range.

According to the manufacturer specifications, the mirrors provide a surface form accuracy better than 1 μm and a surface roughness below 10 nm. Low surface roughness is essential for minimizing diffuse scattering losses and preserving specular reflectance within the optical relay system. Increasing surface roughness leads to enhanced scattering and reduced optical throughput according to classical scattering theory [18].

All circular mirrors of the optical relay system were mounted in custom-designed aluminium holders manufactured in-house. The mounts incorporated precision cylindrical seating, H7 tolerance fits, angular adjustment capability, and rigid fixation after alignment in order to ensure stable and reproducible positioning of the optical components. The flat mirrors located at the spectrometer interface were mounted using commercial kinematic holders compatible with standard optical-bench components.

The upper mirrors positioned above the integrating sphere were installed on five-axis alignment stages with a translational travel range of 3 mm and an angular adjustment range of ±8°. These stages enabled fine angular correction, compensation of assembly tolerances, and precise alignment of the incident and detected radiation paths [37, 73].

The resulting optical relay system provides a stable bidirectional optical connection between the FTIR spectrometer and the FIR-IS while preserving the optical characteristics of the interferometer beam and maintaining reproducible alignment conditions during operation.

4.2.5 Alignment methodology

Alignment of the external optical relay system was performed sequentially using forward and reverse beam tracing in order to obtain reproducible overlap of the incident and detected radiation paths. Since the far-infrared beam itself cannot be directly visualized with sufficient spatial accuracy during mechanical adjustment, auxiliary near-infrared and visible alignment sources were used. The alignment principle is illustrated in Fig. 4.6.

https://doi.org/10.7795/110.20260928

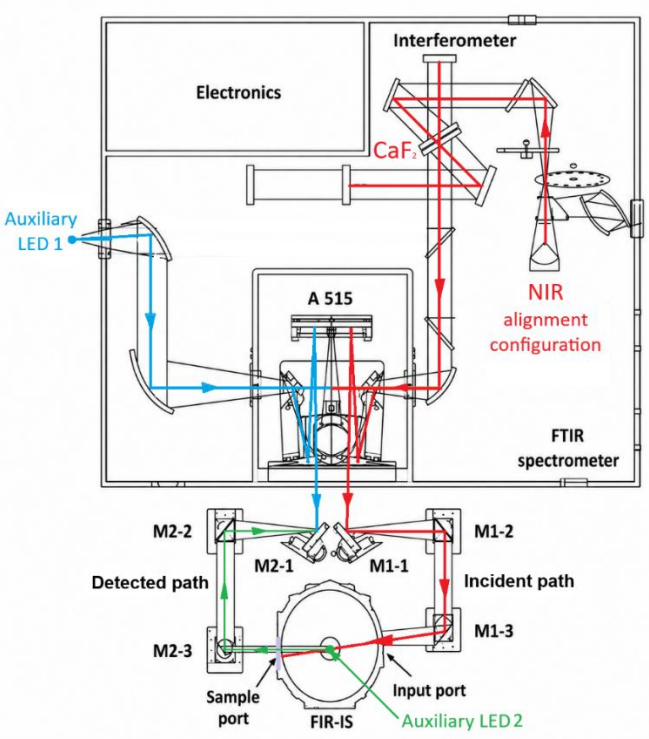


Fig. 4.6. Alignment principle of the external optical relay system. The incident path was aligned using a near-infrared spectrometer configuration with a CaF_2 beamsplitter, while the detected path was verified in reverse direction using auxiliary LED sources. LED 1 and LED 2 denote the spectrometer-side and integrating-sphere-side auxiliary sources, respectively. The red path indicates the incident beam entering the FIR-IS, the green path indicates the detected beam leaving the sphere, and the blue paths indicate auxiliary alignment beams. The abbreviations M1-* and M2-* denote mirror elements of the incident and detected radiation paths, respectively.

For the incident radiation path, the spectrometer was operated in a near-infrared alignment configuration using the internal tungsten-halogen source and a CaF_2 beamsplitter under reduced ambient-light conditions. This configuration provided an observable alignment beam during mechanical adjustment. The mirrors of the incident path were then adjusted iteratively until the beam propagated through the external relay system and was focused reproducibly at the sample position inside the integrating sphere.

The detected path was verified in reverse direction using two auxiliary LED sources. In the first step, LED 1 was positioned on the spectrometer side. With the A515 unit temporarily removed, the beam from LED 1 was adjusted to coincide with the near-infrared alignment beam at the focus in the spectrometer sample compartment, as

https://doi.org/10.7795/110.20260928

indicated schematically in Fig. 4.6. The A515 unit was then reinstalled, so that LED 1 defined the detector-side alignment path through the spectrometer interface toward Mirror 2-1.

In the second step, LED 2 was positioned on the integrating-sphere side at the focal region of the detector-side collection optics. The detector-side mirror sequence was then adjusted in reverse direction until the beam from LED 2 was spatially matched with the beam from LED 1 at Mirror 2-1. This procedure verified that radiation collected from the sphere detector port was correctly transferred through the external relay system and imaged back into the detector path of the spectrometer.

The resulting alignment strategy provided stable optical coupling between the FTIR spectrometer, the external mirror relay system, and the FIR-IS, while preserving the optical configuration required for radiometric measurements. Forward and reverse alignment procedures of this type are commonly used in infrared optical instrumentation when direct visualization of the measurement beam or direct access to detector-side focal regions is limited [3, 27, 67].

4.3 Environmental Enclosure

A dedicated enclosure was constructed around the external optical relay system and the integrating sphere assembly. The enclosure was continuously purged with dry air during operation in order to reduce atmospheric absorption caused primarily by water vapour and carbon dioxide along the external optical path. This is particularly important in infrared spectroscopy, where atmospheric gases can introduce pronounced absorption features into the measured spectra [27, 28, 62].

The enclosure consisted of transparent PMMA panels mounted on a metallic frame. The panels were attached using magnetic fixtures and equipped with handles, allowing convenient access to the integrating sphere system for sample exchange, alignment, and maintenance while maintaining a stable measurement environment during operation. In addition to enabling dry-air purging, the enclosure protected the optical relay system from external mechanical disturbances and helped preserve alignment stability throughout the measurements.

During operation, the temperature inside the enclosure was monitored using a PT100 sensor positioned near the integrating sphere. A second PT100 sensor was

https://doi.org/10.7795/110.20260928

installed inside the spectrometer housing. The FTIR spectrometer itself was operated under stabilized thermal conditions using an external thermostat. Temperature was monitored continuously during the measurements in order to verify stable operating conditions and support reproducible optical alignment throughout the experiments.

A schematic representation of the enclosure together with the incident and detected radiation paths is shown in Fig. 4.7. A photograph of the realized enclosure and the complete experimental setup is presented in Fig. 4.8.

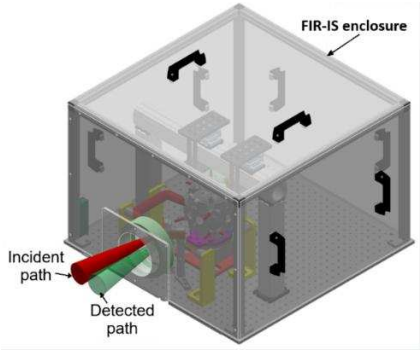


Fig. 4.7. Schematic representation of the FIR-IS enclosure surrounding the external optical relay system and the integrating sphere assembly. The incident (red) and detected (green) radiation paths are indicated.

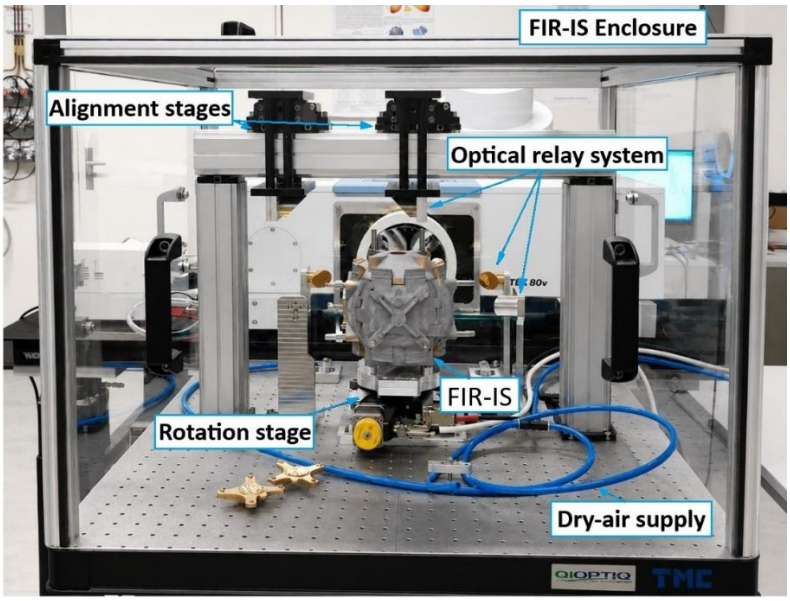


Fig. 4.8. Photograph of the realized FIR-IS enclosure containing the integrating sphere assembly and the external optical relay system. The enclosure is purged with dry air during operation in order to reduce atmospheric absorption along the optical path.

https://doi.org/10.7795/110.20260928

The resulting setup forms a fully integrated external optical measurement platform consisting of the FTIR spectrometer, the A515 beam extraction module, the mirror-based optical relay system, the integrating sphere assembly, and the environmental enclosure with dry-air purging. The developed system preserves the optical throughput and alignment stability of the spectrometer while enabling quantitative directional–hemispherical reflectance and transmittance measurements using the FIR-IS.

The realized setup therefore constitutes the experimental basis for the measurement procedures and validation experiments described in the subsequent chapter.

https://doi.org/10.7795/110.20260928

Chapter 5. Measurements, Radiometric Correction and Validation

This chapter presents the experimental investigation and validation of the FIR-IS together with the associated optical measurement setup developed in the previous chapters. While Chapters 2–4 focused on the development of the RHFS-based surface topology, the mechanical realization of the sphere, and the optical coupling to the FTIR spectrometer, the present chapter evaluates the performance of the complete system under practical operating conditions.

The FIR-IS was designed to enable directional–hemispherical reflectance and transmittance measurements in the infrared spectral range. Within the scope of this work, measurements in the MIR range were carried out from 5 µm to 16.7 µm using an MCT detector, while measurements in the FIR range covered wavelengths from 16.7 µm to 100 µm and were performed using thermal detectors.

In these measurements, radiation is incident on the sample from a defined direction, while the reflected or transmitted radiant flux is collected over the corresponding hemisphere by the integrating sphere. The resulting quantities therefore correspond to directional–hemispherical reflectance or transmittance, depending on the measurement configuration. These quantities are widely used for the characterization of radiative properties of materials and optical components, particularly in the presence of significant scattering effects [9, 10, 11, 34]. Although the FIR-IS is designed to support both quantities, the experimental validation presented in this work focuses primarily on reflectance. The transmittance capability remains part of the general measurement concept and can be implemented using the same sphere and optical coupling configuration.

The measurements were carried out using the FIR-IS coupled to an FTIR spectrometer via the external optical relay system described in Chapter 4. The spectrometer provides broadband radiation from an internal Globar source, while the FIR-IS defines the angular collection geometry after interaction of the radiation with the sample. Depending on the spectral range, different detector technologies were employed. The system was operated under ambient-pressure conditions. To reduce atmospheric

https://doi.org/10.7795/110.20260928

absorption, particularly in spectral regions affected by water vapour and carbon dioxide, selected sections of the optical path were purged with dry air [3, 27, 28].

To verify the functionality and alignment of the optical system, initial measurements were performed in the MIR spectral range using a liquid-nitrogen-cooled MCT detector. This spectral range was selected because of the higher detector sensitivity and improved signal-to-noise ratio compared with the FIR configuration, enabling reliable verification of the optical beam path, the coupling between the spectrometer and the FIR-IS, and the implemented measurement procedure. After successful verification in the MIR range, the measurements were extended to the FIR spectral range from 16.7 µm to 100 µm, where thermal detectors were employed [3, 25, 32, 33].

Two measurement approaches were implemented. The first approach is based on the substitution method, in which reference and sample measurements are performed sequentially under identical optical conditions. The second approach employs a comparison method using a rotating sphere configuration, allowing reference and sample positions to be alternated while maintaining fixed external optical alignment. Both methods are established in integrating-sphere radiometry and provide complementary strategies for evaluating measurement stability and reproducibility [9, 10, 14, 45, 46]. In the present work, however, all final reflectance results are based on the substitution method, as it provided the highest measurement stability under the implemented experimental conditions.

In addition to the experimental measurements, this chapter presents the radiometric correction procedure required for integrating-sphere measurements. The correction accounts for the finite reflectance of the gold-coated sphere wall, the geometrical port configuration, and the residual background signal of the optical system. Such correction procedures are required because the detector signal represents a coupled response of the sample, the sphere wall, the port geometry, and multiple internal reflections rather than the sample reflectance alone [1, 10, 13, 74]. The corrected directional–hemispherical reflectance is subsequently used as the final measurand for validation and uncertainty evaluation. A spectral uncertainty budget is established in accordance with the Guide to the Expression of Uncertainty in Measurement (GUM), including contributions from measurement repeatability, background correction, sphere-wall reflectance, and geometrical parameters [75].

https://doi.org/10.7795/110.20260928

Finally, the corrected measurement results are compared with reference data obtained using the PTB emissivity reference setup (EMAF), providing an independent metrological basis for assessing the performance of the FIR-IS [21, 64, 76].

5.1 Measurement Concept

The measurements performed in this work aim at determining the directional–hemispherical reflectance of material samples in the infrared spectral range. The FIR-IS also provides the optical configuration required for directional–hemispherical transmittance measurements; however, the experimental validation presented in this chapter focuses on reflectance.

In this measurement geometry, radiation is incident on the sample from a defined direction, while the reflected or transmitted radiant flux is collected over the corresponding hemisphere. Such angle-integrated quantities are widely used for the characterization of radiative properties of materials and optical components, particularly when significant scattering effects are present [1, 11, 12, 34, 77].

The measurement concept is based on the FIR-IS, which redistributes radiation by multiple reflections at its structured inner surface. After interaction with the sample, the radiation entering the sphere is repeatedly reflected within the cavity, so that the detector signal becomes proportional to the total radiant flux collected by the sphere rather than to radiation scattered into a specific direction. This principle forms the basis of integrating-sphere radiometry [10, 13].

A schematic representation of the optical configuration is shown in Fig. 5.1. The figure illustrates the incident radiation path and the detected radiation path between the FTIR spectrometer, the FIR-IS, and the detector configurations used in this work. Broadband radiation generated by the internal Globar source propagates through the interferometer and is guided to the external optical relay system via the A515 unit, as described in Chapter 4.

While Fig. 5.1 provides a top-view representation of the incident and detected radiation paths, Fig. 5.2 presents a complementary side view of the measurement setup. This perspective highlights the internal geometry of the FIR-IS, including the positions of the input, sample, and detector ports, as well as the vertical arrangement of the optical components guiding the detected radiation.

https://doi.org/10.7795/110.20260928

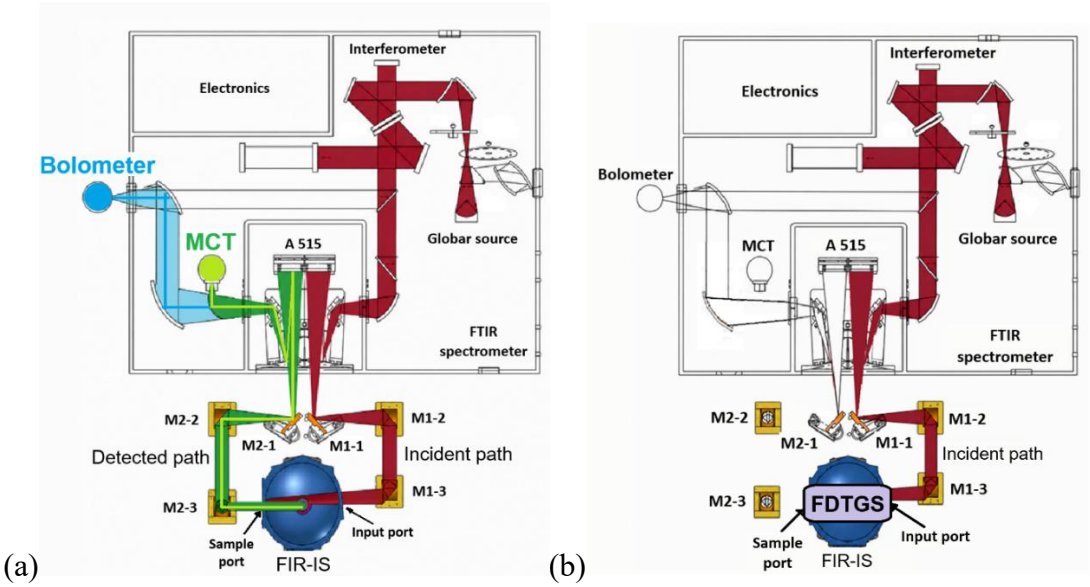


Fig. 5.1. Top-view schematic of the FIR-IS optical setup showing the beam paths between the FTIR spectrometer, the integrating sphere FIR-IS, and the detector positions: (a) external detector coupling, in which either the MCT detector or the bolometer is used as an alternative detector configuration; (b) direct detector coupling with the FDTGS detector mounted at the integrating sphere. The incident beam is shown in red, and the detected beam in green or blue.

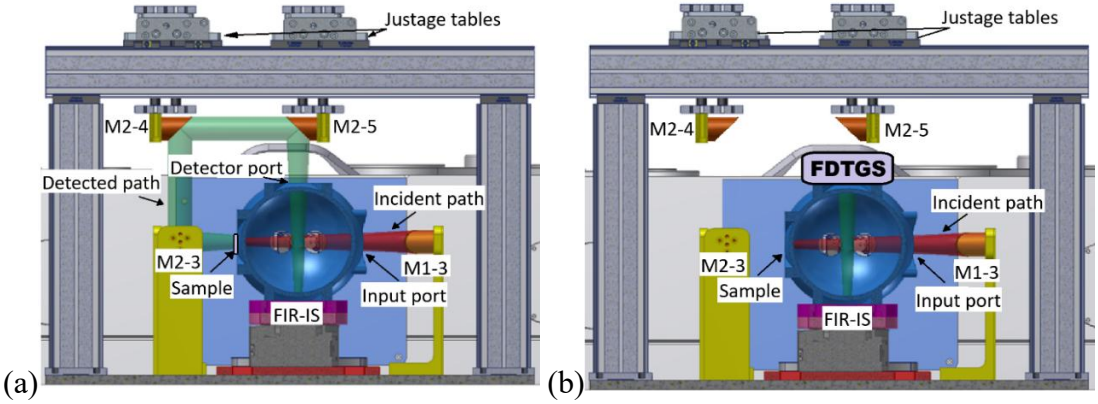


Fig. 5.2. Side-view schematic of the FIR-IS optical setup illustrating the beam paths and detector positions: (a) external detector coupling towards either the MCT detector or the bolometer as alternative detector configurations; (b) direct detector coupling with the FDTGS detector mounted at the integrating sphere. The incident beam is shown in red, and the detected beam in green.

Different detector configurations are employed depending on the spectral range. In the MIR range from 5.0 µm to 16.7 µm, measurements are performed using a liquid-nitrogen-cooled MCT detector. In this configuration, the radiation collected by the FIR-

https://doi.org/10.7795/110.20260928

IS is guided back through the detected radiation path of the external optical relay system, as indicated in Fig. 5.1(a) by the green path.

For measurements in the FIR range from 16.7 µm to 100 µm, thermal detectors are required. The optical setup therefore includes two possible FIR detector configurations: an external bolometer connected via the detected radiation path of the relay optics, and a FDTGS detector mounted directly at the integrating sphere. In the bolometer configuration, the detected radiation leaves the FIR-IS through the detector port and is guided back to the spectrometer-side detector path via the external optical relay system, as indicated in Fig. 5.1(a) by the blue path. In the FDTGS configuration, the detector is positioned directly at the detector port of the sphere, eliminating the need for the external detected radiation path and thereby reducing optical losses, alignment uncertainties, and stray-radiation contributions.

Although the external bolometer is included in the optical design, no stable and reproducible measurement signal could be obtained with this detector under the present configuration. This behaviour is attributed to the insufficient signal level reaching the bolometer under the implemented optical and geometrical conditions, in combination with its sensitivity and noise characteristics.

Consequently, all FIR measurements presented in this work were performed using the FDTGS detector mounted directly at the integrating sphere. This configuration provides an improved signal-to-noise ratio due to the reduced optical path and minimized losses.

Nevertheless, the integration of the bolometer remains an important element of the measurement concept. With further optimization of the optical coupling, alignment, and overall signal throughput, measurements using the bolometer are expected to become feasible in future work, particularly for extended FIR applications.

More generally, the FIR-IS design allows flexible detector integration. Depending on the measurement requirements, detectors can be placed either externally in combination with relay optics or directly at the sphere ports. Furthermore, different ports can be used for illumination and detection, enabling various measurement geometries. This flexibility represents an important feature of the developed system and extends its applicability across different spectral ranges and detector technologies.

https://doi.org/10.7795/110.20260928

Two measurement approaches were implemented. The primary method used in this work is the substitution method, in which the reference surface and the investigated sample are measured sequentially under identical optical conditions. As shown in Fig. 5.3, the FIR-IS is equipped with two illumination ports (Port 2 and Port 5) and two sample/reference ports (Port 3 and Port 4). In the substitution method, measurements are performed using Port 2 for illumination and Port 4 as the reference/sample port. After recording the detector signal for the reference, the sample is placed in the same position without modifying the optical alignment. The measured reflectance is then obtained from the ratio of the measured signals. This method represents the standard approach in integrating-sphere radiometry and provides robust and reproducible results [10, 14].

As a complementary approach, a comparison method based on rotation of the integrating sphere was implemented. In this configuration, the entire sphere is rotated relative to the incident beam, allowing reference and sample positions to be alternated between Port 4 and Port 3 while switching the illumination path between Port 2 and Port 5 (Fig. 5.3), without modifying the external optical alignment. Such schemes reduce alignment-related uncertainties and enable the investigation of measurement stability and drift effects over time. Particularly, alternating measurements under unchanged optical conditions can be used to identify systematic variations in detector response or source intensity [9, 10]. The integrating sphere was mounted on a motorized rotation stage, enabling sample exchange and reconfiguration of the measurement geometry without disassembly of the optical relay system.

The rotating configuration is also compatible with possible future operation under vacuum or reduced-pressure conditions, where manual sample replacement would be impractical and time-consuming. While the present measurements were performed under dry-air conditions, this approach remains relevant for future extensions of the setup. In this work, however, the final results are based exclusively on the substitution method.

https://doi.org/10.7795/110.20260928

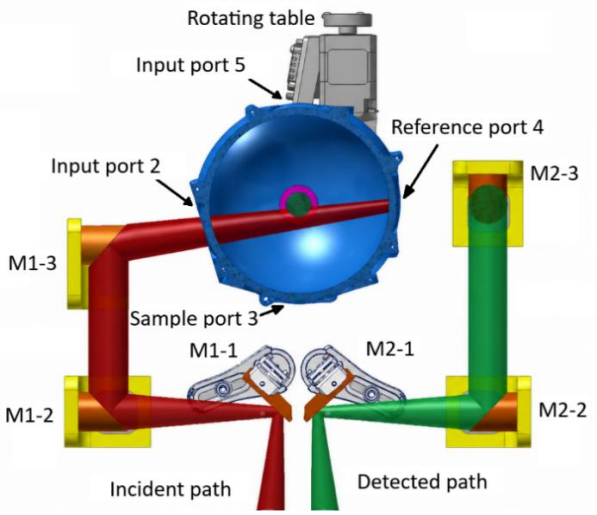


Fig. 5.3. Optical configuration of the FIR-IS with two illumination ports and two sample/reference ports. In the substitution method, Port 2 is used for illumination and Port 4 serves as the reference/sample port. In the rotating comparison configuration, the sphere is rotated relative to the incident beam, allowing alternating measurements between Port 4 and Port 3 while switching the illumination path between Port 2 and Port 5 without modifying the external optical alignment.

A critical aspect of the measurement concept is the separation of the incident and detected radiation paths in order to suppress parasitic reflections originating from the external optical system. The corresponding optical configuration is shown in Fig. 5.4. In this setup, the incident radiation path is guided into the FIR-IS, while the detected radiation path is collected separately after redistribution within the sphere. To support this separation, a beam separator coated with Acktar Velvet Black is introduced at the intersection of the incident and detected radiation paths. Due to its extremely low reflectance over a broad spectral range, this coating absorbs unwanted radiation and minimizes stray-radiation contributions [78, 79]. The implementation of this element improves measurement stability by reducing parasitic signals originating from the mirror relay system.

Further reduction of stray radiation is achieved by iris apertures placed in front of the first mirrors of the optical relay system (Fig. 5.4). These apertures constrain the beam geometry and limit the propagation of off-axis radiation, thereby improving the reproducibility of the optical coupling between the FTIR spectrometer and the FIR-IS.

In addition to sample and reference measurements, dedicated background measurements are performed. In this configuration (Fig. 5.4), the incident radiation is

https://doi.org/10.7795/110.20260928

directed into a light trap, while the sample port remains open. The detector then records the residual signal of the system, originating from stray radiation, multiple reflections, and detector offsets. This signal represents an apparent reflectance of the setup and is referred to as the underground signal R_u. It is taken into account in the data evaluation [80].

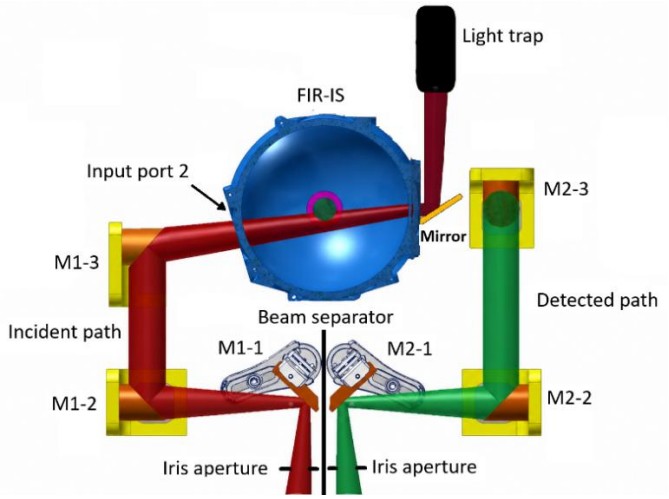


Fig. 5.4. Optical configuration of the FIR-IS illustrating the separation of the incident and detected radiation paths. The incident radiation path is guided into the sphere via the mirror relay system, while the detected radiation path is collected after redistribution within the sphere. A beam separator coated with Acktar Velvet Black is positioned at the intersection of both paths to suppress parasitic reflections. Iris apertures are used to limit off-axis radiation. For background measurements, the incident radiation is directed into a light trap, allowing determination of the underground signal R_u.

5.2 Radiometric Correction of Integrating Sphere Measurements

5.2.1 Necessity of integrating sphere correction

In first approximation, the directional–hemispherical reflectance $R_{d-h,\lambda}$ can be expressed as the ratio of detector signals obtained for the sample S_{sample} and a reference surface $S_{reference}$ under identical experimental conditions,

$$R_{d-h,\lambda} = \frac{S_{sample}}{S_{reference}}. \qquad (5.1)$$

However, when an integrating sphere is used, this ratio does not directly represent the reflectance of the sample under the defined measurement geometry. The measured detector signal is influenced not only by the optical properties of the sample but

https://doi.org/10.7795/110.20260928

also by the radiometric behaviour of the integrating sphere itself. In particular, it depends on the reflectance of the sphere wall, the relative areas of the open ports, and the redistribution of radiation within the cavity due to multiple reflections.

As a result, the measured signal represents a coupled response of the sample and the measurement system. These effects are well established in integrating-sphere radiometry [1, 10, 74, 81, 82] and lead to systematic deviations if not corrected. Therefore, a radiometric correction model is required in order to determine the corrected directional–hemispherical reflectance of the sample.

In the present work, an analytical correction model for integrating-sphere measurements was applied. The model accounts for the influence of the sphere-wall reflectance, the geometrical parameters of the sphere, and the residual background signal of the real measurement system, as described in the literature [80].

5.2.2 Geometrical parameters of the integrating sphere

The correction model requires the definition of geometrical parameters describing the relative distribution of reflective and non-reflective areas within the integrating sphere. These parameters are expressed in terms of fractional surface areas with respect to the total internal surface area of the sphere.

For a sphere with radius r, the internal surface area is given by

$$A_{sphere} = 4\pi r^2. \qquad (5.2)$$

The fractional area of the sample is defined as

$$f_s = \frac{A_{sample}}{A_{sphere}}, \qquad (5.3)$$

where A_{sample} denotes the area of the sample located at the sample port.

The fractional area of the sphere wall is defined as

$$f_g = \frac{A_{gold}}{A_{sphere}}, \qquad (5.4)$$

where A_{gold} represents the effective area of the gold-coated inner surface of the sphere.

https://doi.org/10.7795/110.20260928

The integrating sphere used in this work has an inner diameter of 150 mm and port diameters of 30 mm. During the measurements, only three ports were open: the illumination port, the detector port, and the sample port. All remaining ports were closed using gold-coated inserts designed to reproduce the optical properties of the inner sphere surface.

Under these conditions, the fractional surface areas can be approximated as

$$f_s \approx 0.01, f_g \approx 0.97, \qquad (5.5)$$

leading to a total effective reflective fraction of

$$f_{total} = f_g + f_s \approx 0.98. \qquad (5.6)$$

These parameters determine the redistribution of radiation within the sphere and therefore constitute essential input quantities for the correction model.

5.2.3 Measured quantities

The radiometric correction is based on experimentally determined spectral quantities derived from FTIR measurements.

The measured reflectance $R_m(\lambda)$ is obtained from the ratio of the spectra calculated from the Fourier-transformed interferograms of the sample and the reference measurement. After processing in the OPUS software, this quantity is given by

$$R_m(\lambda) = \frac{S_{sample}(\lambda)}{S_{reference}(\lambda)}, \qquad (5.7)$$

where S_{sample} and $S_{reference}$ denote the spectral detector signals corresponding to the sample and reference measurements, respectively [27].

The sphere-wall reflectance $R_g(\lambda)$ represents the effective reflectance assigned to the gold-coated inner surface of the integrating sphere in the correction model. Since direct measurement of the structured RHFS-800 sphere wall was not feasible with the available EMAF measurement geometry, $R_g(\lambda)$ was derived from spectral emittance measurements of the planar gold-coated reference sample described in Chapter 3. This sample was coated together with the sphere components and was used to characterize the absorption losses of the deposited gold coating. Based on the opacity of the gold

https://doi.org/10.7795/110.20260928

coating and the relation introduced in Chapter 1, the spectral reflectance assigned to the sphere wall is given by

$$R_g(\lambda) = R_{g,d-h}(\lambda) = 1 - e(\lambda) \qquad (5.8)$$

where $e(\lambda)$ denotes the measured directional spectral emittance of the gold-coated reference sample. In the present work, the emittance dataset measured at an observation angle of 20° was used for this evaluation. The 20° dataset was selected because it represents the smallest available observation angle in the EMAF measurements and is therefore closest to near-normal coating behaviour among the measured configurations [21].

In addition to R_m and R_g, the correction requires the underground signal $R_u(\lambda)$. This quantity is obtained using the light-trap configuration described in Section 5.1, in which the incident radiation is directed into a radiation trap instead of illuminating the sample position. The detector then records the residual signal of the optical system.

This signal represents the background contribution of the measurement system and includes residual stray radiation, imperfect absorption, and deviations from ideal sphere behaviour. Its inclusion in the correction model is essential for accurate data evaluation [80].

5.2.4 Correction equations

The measured reflectance $R_m(\lambda)$ does not directly represent the directional–hemispherical reflectance of the sample under the defined measurement geometry. It is influenced by multiple reflections between the sample and the sphere wall, as well as by the finite reflectance of the gold-coated sphere wall and by the port geometry of the system.

To account for these effects, a radiometric correction based on an analytical integrating-sphere model was applied [80]. The model explicitly describes the radiative coupling between the sample and the sphere.

A key quantity in this model is the correction parameter $x(\lambda)$, which accounts for the contribution of the residual background signal and the real-system radiometric response of the sphere wall. It is determined from the underground signal according to

https://doi.org/10.7795/110.20260928

$$x = R_u \cdot \frac{f_g + f_s}{f_g} \cdot \frac{1 - f_g R_g}{1 - (f_g + f_s) R_g}. \qquad (5.9)$$

In this expression, R_u is the underground signal, R_g is the reflectance assigned to the gold-coated sphere wall, f_g is the fractional area of the gold-coated sphere wall, and f_s is the fractional area of the sample.

The corrected directional–hemispherical reflectance $R_s(\lambda)$ is obtained by solving the analytical expression of the integrating-sphere model, which can be written in the form

$$R_s = \frac{A + \sqrt{B}}{C}, \qquad (5.10)$$

where A, B, and C denote algebraic terms of the analytical solution.

The term A is given by

$$\begin{aligned} A = {} & -f_g R_g + x f_g R_g - x f_s R_g + f_{total} f_g R_g^2 - x f_{total} f_g R_g^2 + x f_{total} f_s R_g^2 \\ & - f_{total} f_s R_g^2 R_m, \end{aligned} \qquad (5.11)$$

with $f_{total} = f_g + f_s$.

The term under the square root is given by

$$\begin{aligned} B = R_g^2 \Big[& \Big(4(x-1) f_s \big(f R_g - 1 \big) \\ & \cdot \big(x f_g (f_{\text{total}} R_g - 1) + f_{\text{total}} (1 - f_g R_g) R_m \big) \Big) \\ & + \Big((x-1) f_g (f_{\text{total}} R_g - 1) \\ & + f_s \big(x - x f_{\text{total}} R_g + f_{\text{total}} R_g R_m \big) \Big)^2 \Big] \end{aligned} \qquad (5.12)$$

and accounts for the nonlinear dependence introduced by multiple reflections inside the sphere.

The normalization factor is given by

$$C = 2 f_s (x-1)(f_{total} R_g - 1). \qquad (5.13)$$

https://doi.org/10.7795/110.20260928

The resulting formulation accounts for the combined influence of sphere geometry, finite sphere-wall reflectance, and residual background signal, enabling the corrected sample reflectance to be determined from the measured spectra.

The behaviour of the model can be interpreted by considering limiting cases. For an ideal integrating sphere with perfectly reflecting walls $\left(R_g \to 1 \right)$ and negligible background signal $(R_u \to 0, x \to 0)$, the correction term associated with residual background contributions vanishes. In this limit, the measured and corrected reflectance approach each other.

In real systems, however, deviations from this ideal behaviour are unavoidable. Finite sphere-wall reflectance and non-zero background signals introduce a coupling between the sample and the sphere, which is explicitly captured by the analytical formulation. This demonstrates the necessity of the correction for accurate radiometric measurements.

5.2.5 Implementation of the correction in LabVIEW

The radiometric correction was implemented in a dedicated data-processing routine developed in LabVIEW. A screenshot of the graphical user interface is shown in Fig. 5.5.

The program evaluates the corrected reflectance spectrum based on measured input data and predefined geometrical parameters. The primary input is the measured reflectance $R_m(\lambda)$, defined by Eq. (5.7), representing the uncorrected spectrum.

In addition, the sphere-wall reflectance $R_g(\lambda)$ is required. This can be provided either as a constant value or as a wavelength-dependent spectrum. In the present work, the latter approach was used, based on spectral emittance measurements of the gold-coated planar reference sample described in Chapter 3.

Similarly, the underground signal $R_u(\lambda)$ can be introduced either as a scalar value or as a measured spectrum. In this work, it was determined experimentally for each measurement using the light-trap configuration described in Section 5.1.

To ensure consistent evaluation, an interpolation routine is implemented. Since the spectra $R_m(\lambda)$, $R_g(\lambda)$, and $R_u(\lambda)$ may originate from different measurements and therefore may not share identical wavelength grids, the program resamples R_g and

https://doi.org/10.7795/110.20260928

R_u onto the wavelength grid of R_m. This ensures pointwise consistency and avoids numerical artefacts.

The geometrical parameters f_g and f_s are specified as scalar values determined from the sphere configuration and remain constant during evaluation.

The correction is performed pointwise for each wavelength. First, the correction parameter $x(\lambda)$ is calculated using Eq. (5.9). Subsequently, the corrected reflectance $R_s(\lambda)$ is obtained using Eq. (5.10).

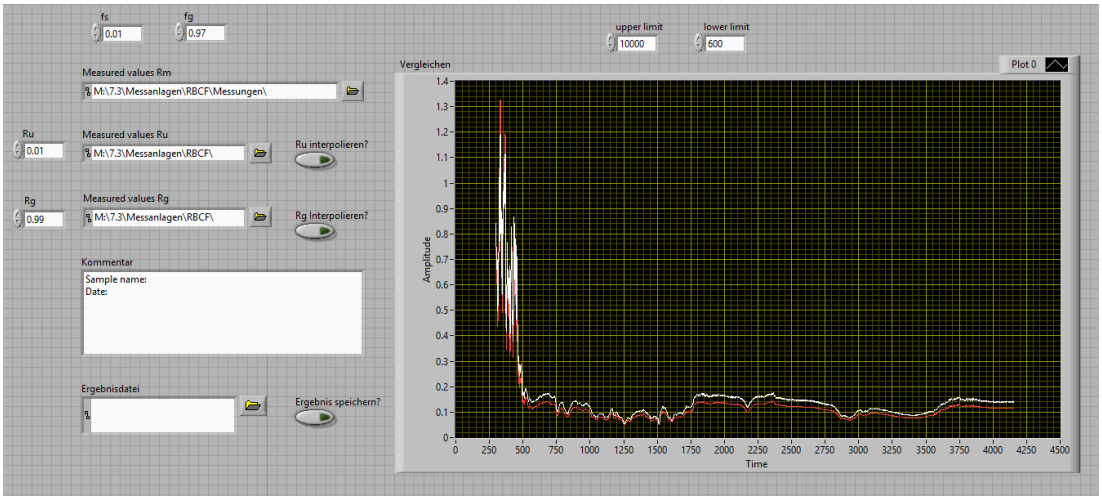


Fig. 5.5. Graphical user interface of the LabVIEW program developed for the radiometric correction of integrating sphere measurements. The program processes the measured reflectance spectrum $R_m(\lambda)$, defined as the ratio of sample and reference signals, together with the sphere-wall reflectance $R_g(\lambda)$ and the underground signal $R_u(\lambda)$. The latter quantities can be provided either as scalar values or as wavelength-dependent spectra. The geometrical parameters f_g and f_s are specified based on the sphere configuration. Optional interpolation functions allow the spectral data to be mapped onto a common wavelength grid prior to evaluation. The displayed plot compares the measured reflectance (red curve) with the corrected reflectance (white curve) obtained after applying the radiometric correction model.

The graphical output allows direct comparison between the measured and corrected spectra, enabling visualization of the correction effect. This implementation provides a flexible and reproducible framework for processing integrating-sphere measurements, supporting both simplified and fully spectral input data.

https://doi.org/10.7795/110.20260928

5.2.6 Processing sequence

The overall data-processing procedure follows a well-defined sequence to ensure consistent and reproducible evaluation.

First, interferograms of the sample and reference are recorded under identical experimental conditions using the FTIR spectrometer. These interferograms are transformed into the spectral domain via Fourier transformation in the OPUS software. Based on the resulting spectra, the measured reflectance $R_m(\lambda)$ is calculated according to Eq. (5.7).

In the next step, the measured spectrum is processed using the LabVIEW routine described in Section 5.2.5. The radiometric correction model is applied, taking into account the sphere-wall reflectance, geometrical parameters, and the underground signal.

As a result, the corrected directional–hemispherical reflectance spectrum $R_s(\lambda)$ is obtained. This spectrum represents the final measurement result of the integrating sphere system and forms the basis for validation and uncertainty evaluation.

5.3 Uncertainty Analysis

5.3.1 General approach

The corrected directional–hemispherical reflectance $R_s(\lambda)$, obtained from the radiometric correction model described in Section 5.2.4, represents the final measurand of the integrating sphere measurement. As shown in Section 5.2, the determination of $R_s(\lambda)$ is based on an analytical model that accounts for the radiative coupling between the sample and the integrating sphere, including the influence of the sphere-wall reflectance, the geometrical configuration, and the residual background signal.

As a consequence, the corrected reflectance $R_s(\lambda)$ depends on several measured and derived input quantities, namely the measured reflectance $R_m(\lambda)$, the underground signal $R_u(\lambda)$, the sphere-wall reflectance $R_g(\lambda)$, and the geometrical parameters f_s and f_g, as introduced in Sections 5.2.2 and 5.2.3. The final measurement result is therefore associated with uncertainties originating both from the experimental determination of these quantities and from the parameters of the integrating sphere model itself.

https://doi.org/10.7795/110.20260928

In accordance with the GUM [75], the measurand is expressed as a function of its input quantities,

$$R_s(\lambda) = R_s\big(R_m(\lambda), R_u(\lambda), R_g(\lambda), f_s, f_g, \lambda\big), \qquad (5.14)$$

where the functional relationship is defined by the analytical correction model given in Section 5.2.4. This model includes nonlinear terms, products of input quantities, and the auxiliary parameter $x(\lambda)$, which itself depends on $R_u(\lambda)$, $R_g(\lambda)$, f_s, and f_g.

All input quantities entering the correction model are wavelength-dependent, with the exception of the geometrical parameters f_s and f_g, which are treated as constants for a given measurement configuration. Consequently, the uncertainty evaluation is performed spectrally, i.e. pointwise as a function of wavelength. This approach enables the determination of a wavelength-dependent uncertainty associated with the corrected reflectance spectrum and is consistent with the spectral nature of the FTIR measurements.

Throughout the uncertainty propagation, all input uncertainties are expressed as standard uncertainties, corresponding to a coverage factor $k = 1$. This applies to the Type A contributions derived from repeated measurements as well as to the Type B contributions associated with the sphere-wall reflectance and geometrical parameters. The expanded uncertainty of the final corrected reflectance is calculated only after propagation of the combined standard uncertainty, using a coverage factor $k = 2$.

Due to the nonlinear structure of the correction model, analytical propagation of uncertainties based on sensitivity coefficients is not applied. In particular, the presence of the auxiliary parameter $x(\lambda)$ introduces coupling between several input quantities, which makes the derivation of analytical sensitivity coefficients cumbersome and potentially unstable. Furthermore, the square-root term in the analytical solution for $R_s(\lambda)$ (see Section 5.2.4) represents an additional source of nonlinearity.

For this reason, a numerical uncertainty propagation approach is employed in the present work. In this approach, the influence of each input quantity on the corrected reflectance is evaluated by perturbation, while consistently accounting for the nonlinear structure of the model. This method avoids the need for explicit analytical derivatives

https://doi.org/10.7795/110.20260928

and ensures that interactions between the input quantities are taken into account. The details of the numerical propagation procedure are described in Section 5.3.3.

5.3.2 Input quantities and classification

The uncertainty analysis is based on the input quantities entering the radiometric correction model introduced in Section 5.2. These quantities can be divided into two groups: experimentally determined spectral quantities and geometrical parameters of the integrating sphere.

The spectral input quantities are the measured reflectance $R_m(\lambda)$, the underground signal $R_u(\lambda)$, and the sphere-wall reflectance $R_g(\lambda)$.

The quantities $R_m(\lambda)$ and $R_u(\lambda)$ are obtained from repeated FTIR measurements and are therefore associated with Type A uncertainties derived from measurement repeatability. The sphere-wall reflectance $R_g(\lambda)$ is derived from spectral emittance measurements of the gold-coated planar reference sample described in Chapter 3. Based on the opacity of the gold coating and the relation introduced in Chapter 1, the reflectance is obtained as given in Eq. (5.8). The corresponding uncertainty is therefore derived from the uncertainty of the spectral emittance measurement and is classified as a Type B contribution. In accordance with common practice in spectral radiometry, both $R_g(\lambda)$ and its uncertainty are treated as wavelength-dependent quantities.

The geometrical parameters f_s and f_g describe the fractional surface areas of the sample port and the gold-coated inner sphere wall, respectively. These parameters are determined from mechanical measurements and geometrical considerations and are treated as constant over the entire spectral range. Their uncertainties arise from measurement tolerances and simplifications of the sphere geometry and are therefore classified as Type B uncertainties.

An overview of the input quantities and their classification is given in Table 5.1.

https://doi.org/10.7795/110.20260928

Quantity	Symbol	Type	Spectral / constant	Method of determination
Measured reflectance	R_m	A	spectral	repeatability of FTIR measurements
Underground signal	R_u	A	spectral	repeatability (light trap measurement)
Sphere wall reflectance	R_g	B	spectral	derived from spectral emittance measurements
Sample fraction	f_s	B	constant	geometrical measurement
Sphere wall fraction	f_g	B	constant	geometrical estimation

Table 5.1. Input quantities and their classification

5.3.2.1 Uncertainty of the measured reflectance $R_m(\lambda)$

The measured reflectance $R_m(\lambda)$ constitutes a primary input quantity of the radiometric correction model and is defined as the ratio of the sample and reference spectra, as described in Section 5.2.3. The associated uncertainty is evaluated as a Type A uncertainty based on the repeatability of the FTIR measurements, in accordance with the GUM [75].

Since $R_m(\lambda)$ is obtained from repeated observations under unchanged experimental conditions, the statistical analysis of these measurements provides a direct estimate of the standard uncertainty without requiring additional model assumptions.

For the repeatability evaluation, the same measurement configuration and the same reflecting surface were used for all repetitions. The gold-coated inner sphere surface was selected because of its high reflectance and stable optical behaviour, providing reproducible measurement conditions. Consequently, variations in $R_m(\lambda)$ are attributed primarily to statistical fluctuations of the measurement system, including source stability, detector noise, and interferometric repeatability.

For the MIR spectral range from 5.0 µm to 16.7 µm, measurements were performed using the FTIR configuration described in Section 5.1, comprising a liquid-nitrogen-cooled MCT detector, a Globar radiation source, and a KBr broadband beamsplitter. The aperture was set to 3 mm and the scanner velocity to 20 kHz. A series of repeated measurements ($n = 20$)was carried out under identical conditions.

https://doi.org/10.7795/110.20260928

From these measurements, the standard deviation $s(R_m, \lambda)$ was determined for each wavelength, and the standard uncertainty was calculated as

$$u(R_m, \lambda) = \frac{s(R_m, \lambda)}{\sqrt{n}}. \qquad (5.15)$$

The resulting uncertainty is wavelength-dependent and reflects the statistical variation of the measured signal. Since the same measurement configuration was used throughout, this variation directly represents the repeatability of the measurement system under the selected conditions.

The evaluated data show that the absolute uncertainty of $R_m(\lambda)$ in the MIR spectral range is on the order of 10^{-6}, indicating a low level of statistical variation. This is consistent with the high sensitivity of the MCT detector and the favourable signal-to-noise ratio in this spectral region. Figure 5.6 illustrates the repeatability of the measured signal used to estimate the Type A uncertainty contribution assigned to $R_m(\lambda)$ in the MIR range.

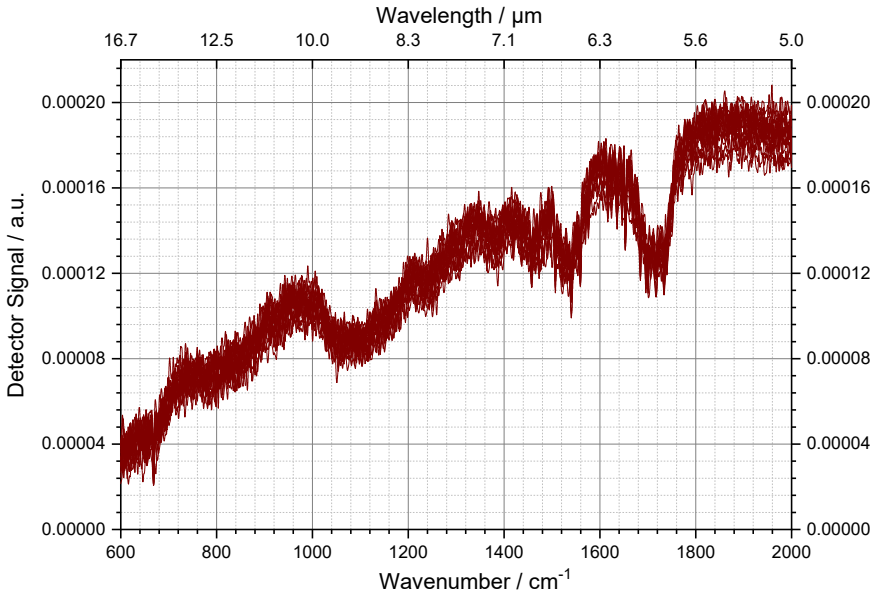


Fig. 5.6. Repeatability of the measured signal in the MIR spectral range, obtained from 20 repeated FTIR measurements using the gold-coated inner sphere surface. The spread of the curves reflects the statistical variation used for the determination of the standard uncertainty contribution assigned to $R_m(\lambda)$.

https://doi.org/10.7795/110.20260928

For the FIR spectral range from 16.7 µm to 100 µm, the same evaluation procedure was applied using the FIR configuration described in Section 5.1, employing a FDTGS detector mounted directly at the integrating sphere and a Mylar multilayer beamsplitter. The aperture was set to 3 mm and the scanner velocity to 2.5 kHz. Again, a series of repeated measurements ($n = 20$) was performed under unchanged conditions, and the standard uncertainty was determined according to Eq. (5.15).

In this spectral range, the reflectance values are on the order of 10^{-4}, while the absolute uncertainty remains on the order of 10^{-6}. Due to the increased noise of the thermal detector, the relative uncertainty is therefore higher than in the MIR range. Figure 5.7 shows the repeatability of the measured signal used to estimate the Type A uncertainty contribution assigned to $R_m(\lambda)$ in the FIR range.

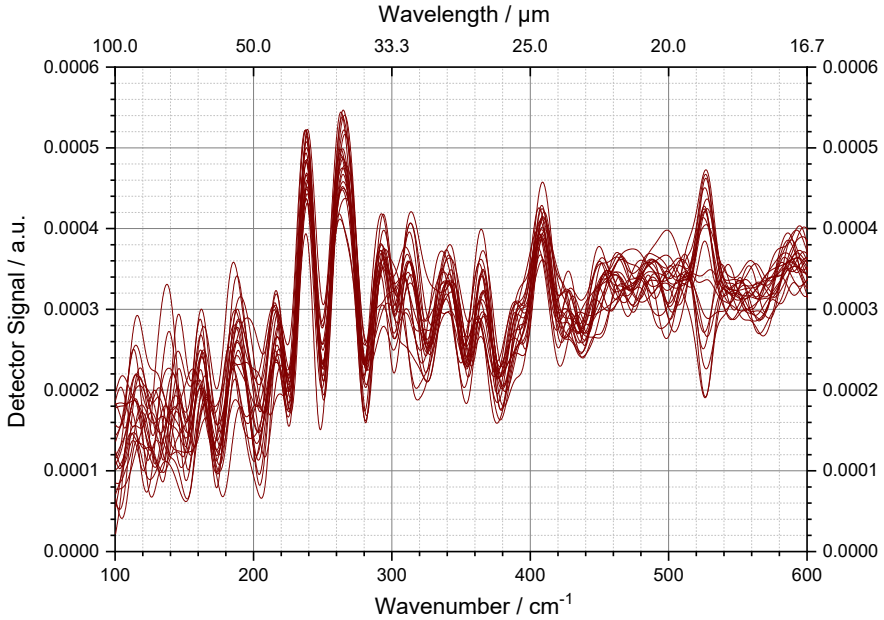


Fig. 5.7. Repeatability of the measured signal in the FIR spectral range, obtained from 20 repeated FTIR measurements using a FDTGS detector mounted directly at the integrating sphere. The increased spread reflects the lower signal-to-noise ratio in the FIR configuration and is used to estimate the standard uncertainty contribution assigned to $R_m(\lambda)$.

Overall, the uncertainty of $R_m(\lambda)$ is governed by the repeatability of the FTIR measurements and reflects the detector performance, source stability, and signal-to-noise ratio in the respective spectral range.

https://doi.org/10.7795/110.20260928

5.3.2.2 Uncertainty of the underground signal $R_u(\lambda)$

The underground signal $R_u(\lambda)$ is an experimentally determined input quantity of the radiometric correction model. It represents the residual response of the measurement system in a configuration in which the incident radiation does not interact with the sample. In the implemented setup, the incident radiation is redirected into a light trap, as described in Section 5.1, so that the detector records the residual signal of the optical system rather than radiation reflected by the sample. The detector records the remaining system signal, which originates from detector noise, stray radiation, imperfect beam suppression, and residual reflections within the optical system.

It is essential to distinguish between the underground signal $R_u(\lambda)$ itself and its associated uncertainty. The non-zero value of $R_u(\lambda)$ is not treated as an uncertainty contribution, but as a measured input quantity of the correction model. Its standard uncertainty is evaluated separately from repeated measurements. According to the GUM [75], this corresponds to a Type A evaluation based on the statistical analysis of repeated observations under unchanged measurement conditions.

For the repeatability evaluation, the underground signal was measured repeatedly using the same optical configuration as in the corresponding reflectance measurements. Since the optical alignment and measurement geometry were kept unchanged, the observed variation of $R_u(\lambda)$ can be attributed to statistical fluctuations of the measurement system.

For each wavelength, the mean underground signal was determined from the repeated measurements, and the experimental standard deviation $s(R_u, \lambda)$ was calculated. As the mean value is used in the correction model, the corresponding standard uncertainty is calculated analogously to Eq. (5.15).

For the MIR spectral range 5.0 µm – 16.7 µm, the underground measurements were performed using the same configuration as for the reflectance measurements, comprising a Globar source, a KBr broadband beamsplitter, and a liquid-nitrogen-cooled MCT detector. The aperture was set to 3 mm and the scanner velocity to 20 kHz. A series of repeated measurements was recorded under unchanged conditions. Figure 5.8 shows the repeatability of $R_u(\lambda)$ in the MIR spectral range.

https://doi.org/10.7795/110.20260928

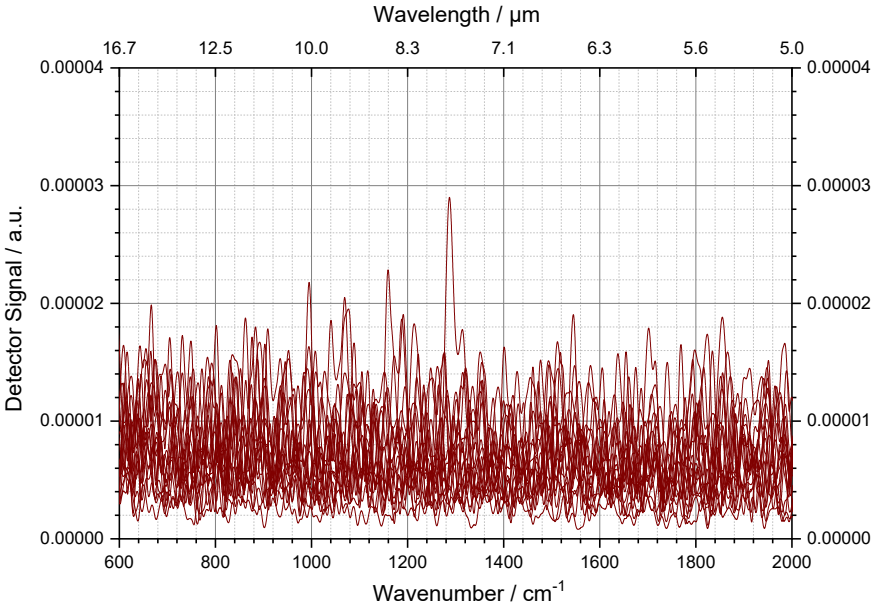


Fig. 5.8. Repeatability of the underground signal $R_u(\lambda)$ in the MIR spectral range, obtained from repeated measurements using the light-trap configuration. The spread of the curves reflects the statistical variation used for the Type A evaluation of $u(R_u, \lambda)$.

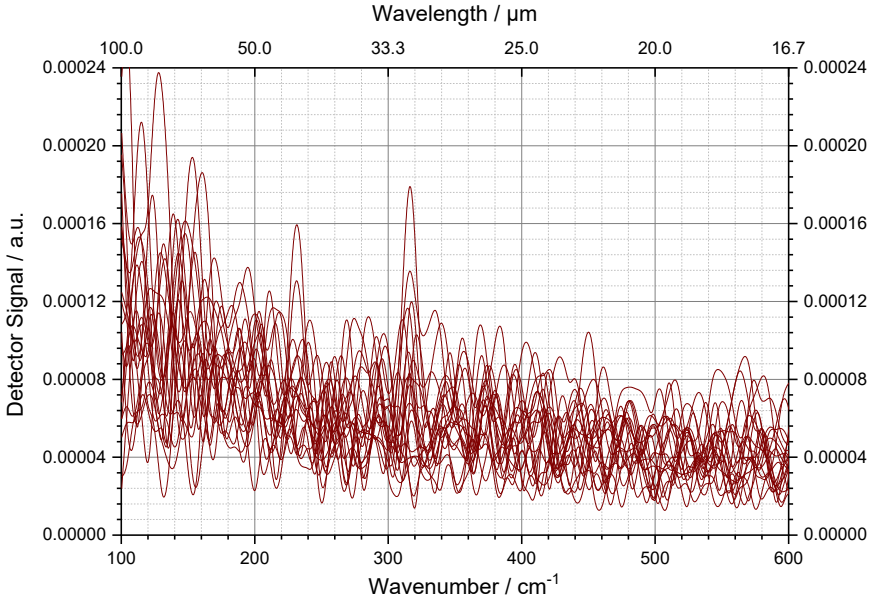


Fig. 5.9. Repeatability of the underground signal $R_u(\lambda)$ in the FIR spectral range, obtained from repeated measurements using the light-trap configuration and a FDTGS detector mounted directly at the integrating sphere. The increased spread reflects the reduced signal-to-noise ratio in the FIR configuration.

https://doi.org/10.7795/110.20260928

For the FIR spectral range 16.7 µm – 100 µm, the same procedure was applied using the FIR configuration, consisting of a Mylar multilayer beamsplitter and a FDTGS detector mounted directly at the integrating sphere. The aperture was set to 3 mm and the scanner velocity to 2.5 kHz. The repeated measurements exhibit a larger statistical spread than in the MIR range, which is consistent with the reduced signal-to-noise ratio of the thermal detector at longer wavelengths. Figure 5.9 illustrates the repeatability of $R_u(\lambda)$ in the FIR spectral range.

The resulting $R_u(\lambda)$ and $u(R_u, \lambda)$ are treated as spectral quantities over the full investigated range from 5.0 µm to 100 µm. Figure 5.10 shows the combined underground signal together with its standard uncertainty, which serves as input for the subsequent uncertainty propagation through the correction model.

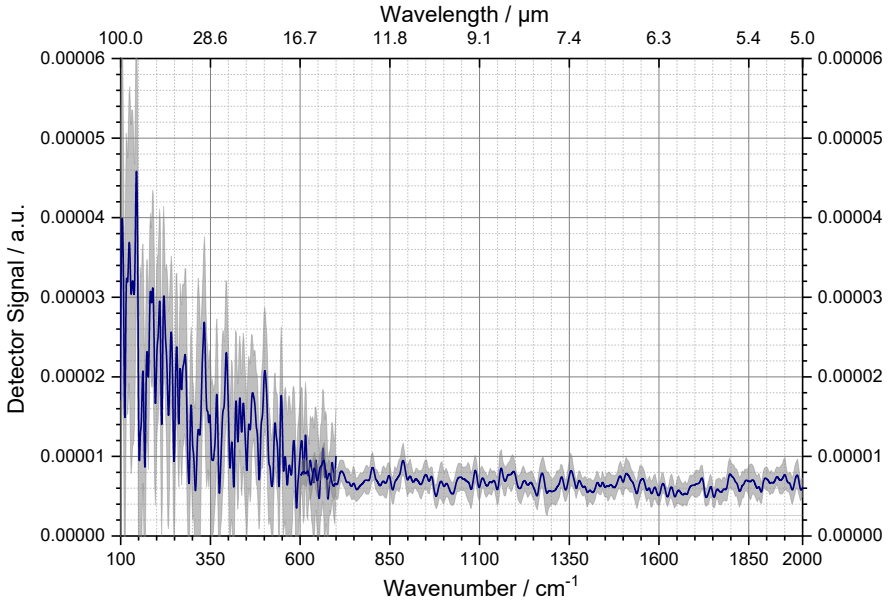


Fig. 5.10. Mean spectral underground signal $R_u(\lambda)$ over the full investigated range from 5.0 µm to 100 µm, shown together with its standard uncertainty $u(R_u, \lambda)$. The mean signal is used as an input quantity in the correction model, while the uncertainty is propagated pointwise.

Although the underground signal is small compared to the measured reflectance, it is explicitly included in the analysis, as it enters the auxiliary correction parameter $x(\lambda)$. Consequently, both the mean value $R_u(\lambda)$ and its associated uncertainty $u(R_u, \lambda)$ are propagated pointwise in the final uncertainty budget.

https://doi.org/10.7795/110.20260928

5.3.2.3 Geometrical parameters f_s and f_g

The geometrical parameters f_s and f_g describe the fractional surface areas of the sample port and the gold-coated inner sphere wall, respectively, and constitute input quantities of the radiometric correction model. These parameters determine the redistribution of radiation inside the integrating sphere and therefore influence the corrected reflectance.

The fractional surface areas are defined with respect to the total internal surface area of the sphere. Their analytical expressions were introduced in Section 5.2 and are therefore not repeated here. In the present section, the focus is placed on the determination of the corresponding input values and their associated uncertainties.

During the measurements, three ports were open, namely the input port, the detector port, and the sample port. All remaining ports were closed using gold-coated inserts designed to reproduce the optical properties of the inner sphere surface. Under these conditions, the geometrical parameters f_s and f_g are determined by the relative dimensions of the sphere and the open ports.

In order to obtain realistic input values, a representative port diameter was determined experimentally. The input port was measured at several positions and orientations, and additional check measurements were performed on other ports to verify comparable dimensions. A total of twenty measurements yielded a mean representative port diameter

$$d_p = 29.905\ \text{mm},$$

with an experimental standard deviation

$$u(d_p) = 0.423\ \text{mm}.$$

The observed spread reflects both measurement uncertainty and actual geometrical deviations of the port geometry. Therefore, the experimental standard deviation was conservatively used as the standard uncertainty of the representative port diameter, rather than as the uncertainty of the mean. The same value was used for the sample port diameter d_s, assuming comparable manufacturing tolerances.

The inner diameter of the integrating sphere could not be determined directly due to the structured surface and the gold coating. The nominal value

https://doi.org/10.7795/110.20260928

$$D = 150\,\text{mm}$$

was therefore used together with an estimated deviation of ±1 mm. Assuming a rectangular probability distribution, the corresponding standard uncertainty is

$$u(D) = \frac{1}{\sqrt{3}} = 0.577\,\text{mm}. \qquad (5.16)$$

The contribution of the gold coating thickness (approximately 200 nm) is negligible compared to the sphere diameter and was therefore not considered.

The standard uncertainties of f_s and f_g were determined using the law of propagation of uncertainty. For the sample fraction, this yields

$$u^2(f_s) = \left(\frac{\partial f_s}{\partial d_s} u(d_s)\right)^2 + \left(\frac{\partial f_s}{\partial D} u(D)\right)^2, \qquad (5.17)$$

and for the sphere wall fraction

$$u^2(f_g) = \left(\frac{\partial f_g}{\partial d_p} u(d_p)\right)^2 + \left(\frac{\partial f_g}{\partial D} u(D)\right)^2. \qquad (5.18)$$

The required sensitivity coefficients follow directly from the analytical expressions introduced in Section 5.2 and are therefore not repeated here.

Using the measured and estimated values

$$d_p = d_s = 29.905\,\text{mm}, u(d_p) = 0.423\,\text{mm}, D = 150\,\text{mm}, u(D) = 0.577\,\text{mm},$$

the resulting fractional areas are approximately

$$f_s \approx 0.01, f_g \approx 0.97,$$

with corresponding standard uncertainties

$$u(f_s) \approx 3 \cdot 10^{-4}, u(f_g) \approx 1 \cdot 10^{-3}.$$

These uncertainties are small compared to the nominal values of the geometrical parameters, which is consistent with the relatively large sphere diameter compared to the port diameters. The dominant contribution to the uncertainty originates from the variability of the port diameters, while the uncertainty of the sphere diameter has a smaller influence.

https://doi.org/10.7795/110.20260928

The geometrical parameters f_s and f_g, together with their associated uncertainties, are treated as Type B input quantities in the uncertainty budget and are assumed to be constant over the entire investigated spectral range.

5.3.2.4 Sphere-wall reflectance $R_g(\lambda)$

The sphere-wall reflectance $R_g(\lambda)$ is a key input quantity of the radiometric correction model, as it governs the radiative coupling between the sample and the gold-coated inner surface of the integrating sphere.

In the present work, $R_g(\lambda)$ was not measured directly within the integrating sphere setup. Direct spectral emittance measurement of the structured RHFS-800 sphere wall was not feasible with the available EMAF measurement geometry. Therefore, $R_g(\lambda)$ was derived from spectral emittance measurements of the planar gold-coated reference sample described in Chapter 3. This sample was coated together with the sphere components and was used to characterize the absorption losses of the deposited gold coating.

Based on the opacity of the gold coating and the relation introduced in Chapter 1, the reflectance assigned to the gold-coated sphere wall is obtained as given in Eq. (5.8), where $e(\lambda)$denotes the measured directional spectral emittance of the gold-coated reference sample. In Chapter 3, the emittance of this sample was measured at several observation angles. For the radiometric correction model, the dataset measured at an observation angle of 20° was used. This dataset was selected because it represents the smallest reliable observation angle available for the highly reflecting gold-coated reference sample; measurements at 10° are avoided for mirror-like samples in the EMAF configuration due to direct back-reflection into the optical path.

The emittance data and their associated uncertainties were obtained from measurements carried out at PTB using EMAF. The uncertainty evaluation follows the methodology established for high-accuracy spectral emittance measurements, as described in the literature [21]. Within this framework, both $e(\lambda)$ and its uncertainty are treated as wavelength-dependent quantities, enabling pointwise evaluation over the full spectral range.

The standard uncertainty of the sphere-wall reflectance is directly obtained from the emittance uncertainty as

https://doi.org/10.7795/110.20260928

$$u(R_g, \lambda) = u(e, \lambda). \qquad (5.19)$$

The provided uncertainty data correspond to a coverage factor of $k = 1$and are therefore used directly as standard uncertainties, consistent with the uncertainty treatment adopted in Section 5.3.1. The expanded uncertainty is applied only to the final corrected reflectance after uncertainty propagation.

Both $R_g(\lambda)$ and $u(R_g, \lambda)$ are treated as spectral quantities over the investigated wavelength range from 5.0 µm to 100 µm. This spectral treatment is essential, as the reflectance assigned to the gold-coated sphere wall exhibits wavelength dependence, particularly in the far-infrared region. Figure 5.11 shows the spectral reflectance $R_g(\lambda)$, derived from the 20° spectral emittance, together with its associated standard uncertainty. The shaded region represents the wavelength-dependent standard uncertainty.

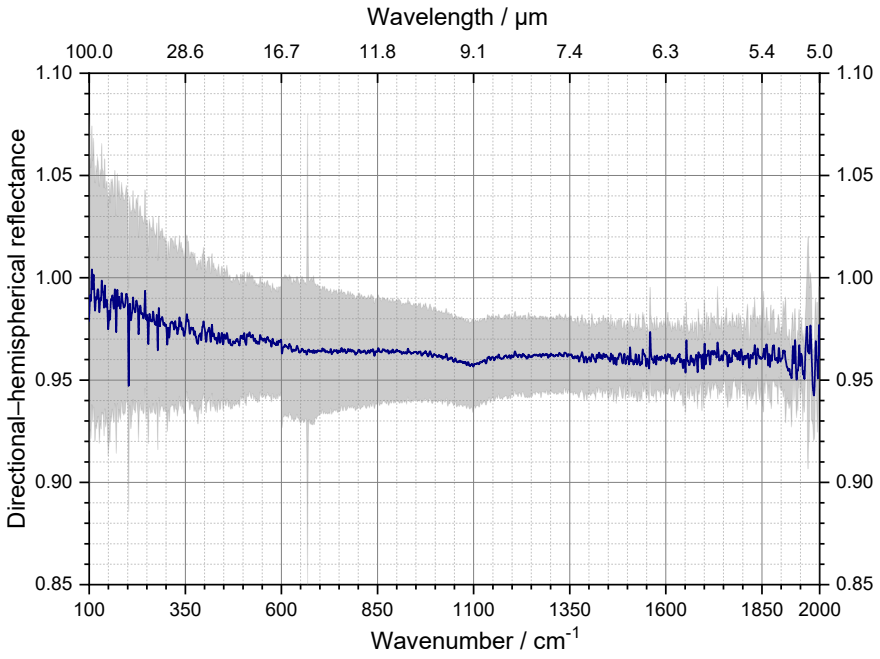


Fig. 5.11. Directional–hemispherical reflectance $R_g(\lambda)$ assigned to the gold-coated sphere wall in the radiometric correction model, derived from the directional spectral emittance of a planar gold-coated reference sample representative of the sphere-wall coating. The emittance was measured with the PTB reference setup EMAF at $T = 80\,°C$ and an observation angle of 20°. The 20° dataset was used because it represents the smallest reliable observation angle for the highly reflecting gold-coated sample. The shaded region represents the standard uncertainty $u(R_g, \lambda)$ ($k = 1$).

https://doi.org/10.7795/110.20260928

The quantities $R_g(\lambda)$ and $u(R_g, \lambda)$ are treated as Type B input quantities, as they are derived from independent measurements and not from repeated observations within the present experiment.

The influence of $R_g(\lambda)$ on the uncertainty budget is particularly significant. Due to its nonlinear role in the correction model, the uncertainty associated with the sphere-wall reflectance constitutes the dominant contribution to the combined uncertainty of the corrected reflectance over most of the investigated spectral range.

This behaviour reflects the fact that the radiative exchange within the integrating sphere is strongly governed by the wall reflectance. Consequently, uncertainties in $R_g(\lambda)$, even if moderate, propagate efficiently through the correction model and ultimately limit the achievable measurement accuracy.

5.3.3 Uncertainty propagation method

The corrected directional–hemispherical reflectance $R_s(\lambda)$, as introduced in Section 5.2.4, is obtained from an analytical radiometric correction model involving multiple coupled input quantities and nonlinear terms. Consequently, the propagation of uncertainties from the input quantities to the corrected reflectance requires a consistent and physically meaningful approach.

Within the framework of the GUM, uncertainty propagation is commonly performed using sensitivity coefficients, defined as partial derivatives of the measurand with respect to the input quantities [75]. In this approach, the combined standard uncertainty is obtained as a weighted combination of the individual contributions, providing a direct interpretation of their influence on the measurement result.

However, the correction model applied in the present work exhibits a strongly nonlinear structure. The analytical expression for $R_s(\lambda)$ contains higher-order terms, products of input quantities, and a square-root term arising from the solution of the integrating-sphere model. In addition, the auxiliary parameter $x(\lambda)$, introduced to account for the real-system radiometric response of the integrating sphere, depends explicitly on several input quantities, namely $R_u(\lambda)$, $R_g(\lambda)$, f_s, and f_g. This results in an implicit coupling between the input quantities and introduces additional nonlinear dependencies within the model.

https://doi.org/10.7795/110.20260928

Under these conditions, the determination of analytical sensitivity coefficients is not practical. Even if formally derived, their evaluation would be cumbersome and potentially numerically unstable, particularly in spectral regions where the model exhibits increased sensitivity. Moreover, the validity of the linear approximation underlying the classical GUM approach is limited in the presence of pronounced nonlinearities.

For models of this type, GUM Supplement 1 recommends the use of numerical methods, such as Monte Carlo techniques or the propagation of distributions. In the present work, a numerical perturbation approach is employed to analyse the influence of the individual input quantities on the corrected reflectance. This method can be interpreted as a finite-difference approximation of the sensitivity coefficients and is well suited for the analysis of complex nonlinear models.

In the numerical implementation, each input quantity

$$x_i \in \{R_m, R_u, R_g, f_s, f_g\}$$

is varied individually by its associated standard uncertainty $u(x_i)$, while all other quantities are kept at their nominal values. The corrected reflectance is then recalculated for positive and negative perturbations,

$$R_{s,+}(\lambda) = R_s(x_i + u(x_i)), R_{s,-}(\lambda) = R_s(x_i - u(x_i)). \qquad (5.20)$$

The resulting variation of the corrected reflectance provides a direct estimate of the sensitivity of the model to the corresponding input quantity. For input quantities exhibiting an approximately symmetric response, the associated variation is evaluated as

$$\Delta_i(R_s, \lambda) = \left| \frac{R_{s,+}(\lambda) - R_{s,-}(\lambda)}{2} \right|. \qquad (5.21)$$

This quantity represents a numerical measure of the local sensitivity and is used to analyse the relative importance of the different input quantities across the spectral range.

A specific feature of the present correction model is the presence of the auxiliary parameter $x(\lambda)$, which depends on several input quantities. Therefore, any perturbation of $R_u(\lambda)$, $R_g(\lambda)$, f_s, or f_g requires a consistent recalculation of $x(\lambda)$ prior to evaluating

https://doi.org/10.7795/110.20260928

the corrected reflectance. This step is essential to preserve the internal consistency of the model and to correctly represent the physical coupling between the quantities.

In addition to the nonlinear coupling, physical constraints must be taken into account. In particular, the reflectance of the sphere wall is physically limited to values not exceeding unity. Due to the uncertainty associated with $R_g(\lambda)$, the perturbed value $R_g(\lambda) + u(R_g, \lambda)$ may formally exceed this limit. In the numerical implementation, this is addressed by restricting the perturbed values to the physically admissible range. As a consequence, the model response may become asymmetric with respect to positive and negative perturbations. In such cases, the associated variation is evaluated conservatively as the maximum deviation from the nominal value.

The numerical perturbation analysis provides a consistent characterization of the sensitivity of $R_s(\lambda)$ to each input quantity over the entire spectral range. In particular, it enables the identification of dominant uncertainty contributions and their spectral behaviour while fully accounting for the nonlinear structure of the model.

The analysis shows that the contribution associated with the sphere-wall reflectance $R_g(\lambda)$ clearly dominates the uncertainty budget. For the investigated Nextel sample, measured with the FIR-IS at room temperature and an incidence angle of 8°, the mean relative contribution of $R_g(\lambda)$ in the MIR spectral range is approximately 0.85 and exceeds 0.95 in certain spectral regions. In contrast, the contributions associated with $R_m(\lambda)$ and $R_u(\lambda)$ are several orders of magnitude smaller and can be considered negligible, while the geometrical parameters f_s and f_g contribute at the level of approximately 1 % or less.

A similar behaviour is observed in the FIR spectral range, where the contribution of $R_g(\lambda)$ remains dominant, with a mean value close to unity (approximately 0.99), while all other contributions are significantly smaller.

These results demonstrate that the uncertainty of the corrected reflectance is primarily governed by the uncertainty of the sphere-wall reflectance over the entire investigated spectral range.

For the determination of the combined standard uncertainty, a simplified approach is adopted based on the root sum of squares of the individual standard uncertainties,

https://doi.org/10.7795/110.20260928

$$u_c(R_s,\lambda) = \sqrt{u(R_m,\lambda)^2 + u(R_u,\lambda)^2 + u(R_g,\lambda)^2 + u(f_s)^2 + u(f_g)^2}. \qquad (5.22)$$

This formulation represents a conservative estimate of the combined uncertainty used for the final uncertainty band. While the individual perturbation analysis is used to identify the relative importance of the input quantities, the final uncertainty estimate is based on this simplified root-sum-of-squares approach, which provides a robust and stable uncertainty interval consistent with the observed behaviour of the system.

The expanded uncertainty is obtained by applying a coverage factor $k = 2$, corresponding to a confidence level of approximately 95 %,

$$U(R_s,\lambda) = k \cdot u_c(R_s,\lambda), k = 2. \qquad (5.23)$$

The final measurement result is therefore expressed as

$$R_s(\lambda) \pm U(R_s,\lambda). \qquad (5.24)$$

Figure 5.12 shows the corrected reflectance of the Nextel sample together with the expanded uncertainty over the full spectral range. The uncertainty is represented as a shaded region around the corrected reflectance curve.

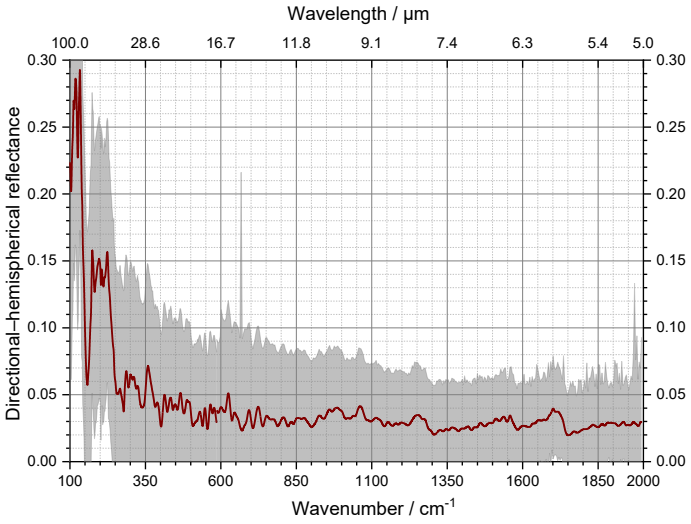


Fig. 5.12. Corrected directional–hemispherical reflectance $R_s(\lambda)$ of the Nextel 811-21 sample measured with the FIR-IS at room temperature ($T \approx 25\ °C$) and an incidence angle of 8°. The shaded region represents the expanded uncertainty $U(R_s,\lambda)$, obtained from the combined standard uncertainty using a coverage factor of $k = 2$, corresponding to a confidence level of approximately 95 %.

https://doi.org/10.7795/110.20260928

The analysis of the uncertainty budget shows that the dominant contribution to the combined uncertainty originates from the sphere-wall reflectance $R_g(\lambda)$, while all remaining contributions are significantly smaller over most of the investigated spectral range. This result demonstrates that the achievable measurement accuracy is primarily limited by the uncertainty associated with the emittance-derived reflectance of the gold-coated reference sample used to estimate the sphere-wall reflectance.

5.4 Results and validation

The validation of the integrating sphere measurement system was carried out by comparative measurements using well-characterized samples with different reflectance levels. Particular emphasis was placed on the far-infrared spectral range, where the determination of directional–hemispherical reflectance is of high relevance for radiative heat transfer applications, as discussed in the introduction.

In order to ensure reliable interpretation of the FIR results, initial measurements were performed in the MIR spectral range. Owing to the higher sensitivity of the MCT detector and the improved signal-to-noise ratio, the MIR measurements provide a suitable basis for assessing the performance of the optical system, including alignment, stability, and overall functionality of the integrating sphere.

The reflectance measurements were performed using an FTIR spectrometer in combination with the FIR-IS, as described in Section 5.1. The measurement procedure is based on the substitution method and includes correction for residual background contributions, finite sphere-wall reflectance, and geometrical effects associated with the integrating sphere configuration.

In the substitution measurements, the reference signal $S_{\mathrm{reference}}$was obtained using a gold-coated reference plug mounted at the measurement port. This reference element was fabricated together with the sphere components and provides the same gold-coated RHFS-800-based surface as the corresponding internal sphere wall. It is important to distinguish this reference plug from the sphere-wall reflectance R_g used in the radiometric correction model: the reference plug serves as the reference surface for the experimental ratio $R_m = S_{sample}/S_{reference}$, whereas R_g represents the effective reflectance assigned to the gold-coated inner sphere wall. A photograph of the reference plug used for the reflectance measurements is shown in Fig. 5.13.

https://doi.org/10.7795/110.20260928



Fig. 5.13. Gold-coated reference plug used as the reference surface in the substitution measurements of the FIR-IS. The plug was mounted at the measurement port during acquisition of the reference signal $S_{reference}$.

Different detector and beamsplitter configurations were employed depending on the spectral range. In the MIR range from 5.0 µm to 16.7 µm, a liquid-nitrogen-cooled MCT detector was used in combination with a KBr beamsplitter. This configuration provides high sensitivity and a favourable signal-to-noise ratio and is therefore well suited for system validation.

In the FIR spectral range from 16.7 µm to 100 µm, measurements were performed using a pyroelectric FDTGS detector in combination with a multilayer Mylar beamsplitter. In contrast to the MIR configuration, the detector is mounted directly at the integrating sphere. The underlying measurement principle, however, remains unchanged: the reflectance is determined using the substitution method by sequentially measuring the reference and the sample under identical conditions.

The use of different detector configurations is dictated primarily by the spectral characteristics of the source, beamsplitter, and detector. In the FIR range, both the source intensity and detector responsivity are lower than in the MIR range. Consequently, direct detector coupling at the integrating sphere is required to obtain a measurable signal. As a result, FIR measurements are associated with lower signal levels and increased noise, which is reflected in a higher measurement uncertainty.

For validation of the measurement system, samples with different optical properties were investigated. Nextel 811-21 was used as a low-reflectance, highly absorbing coating with spectrally smooth behaviour. A laser-structured aluminium sample coated with gold was used as a high-reflectance sample, where the gold coating provides high

https://doi.org/10.7795/110.20260928

reflectance while the surface structure introduces angular redistribution. In addition, an Aeroglaze Z306 coating with a thickness of 99 µm was investigated as a technically relevant material for thermal control applications. Together, these samples enable assessment of the FIR-IS over a broad range of reflectance levels and scattering behaviours.

The measured reflectance values were compared with independent reference data obtained from spectral emittance measurements performed at PTB. For opaque samples, the corresponding reference reflectance was derived from the measured emittance using the relation introduced in Chapter 1. The PTB measurements were carried out using dedicated high-accuracy setups for spectral emittance determination, including both vacuum and ambient configurations, as described in the literature [21, 64, 76]. These measurements provide an independent metrological basis for validation of the FIR-IS results.

5.4.1 Nextel 811-21

The investigated sample consists of a Nextel 811-21 coating applied to a metallic substrate. Nextel 811-21 is a well-established high-emittance coating widely used in radiometric applications, ranging from blackbody cavities to optically absorbing surfaces in instrumentation, where suppression of unwanted reflections is required [83, 84]. The coating is characterized by a low-reflectance surface with high absorption of scattered radiation, as well as favourable mechanical properties, including resistance to scratching and abrasion and good antistatic behaviour.

The coating material was originally provided by 3M and is currently available from Mankiewicz Gebr. & Co., from whom it was obtained for the present work. The sample was prepared according to the manufacturer's specifications, including spray deposition of a primer layer followed by spray application of the Nextel 811-21 coating. In this study, the coating serves as a representative low-reflectance sample for validating the integrating sphere measurement system and the applied radiometric correction procedure.

The measurements were carried out using the MIR and FIR configurations described in Section 5.1. The directional–hemispherical reflectance was corrected using the method described in Section 5.2, including correction for residual background contributions, finite sphere-wall reflectance, and geometrical effects of the integrating

https://doi.org/10.7795/110.20260928

sphere configuration. The associated uncertainty was evaluated according to the procedure described in Section 5.3.

The resulting directional–hemispherical reflectance of the Nextel coating over the spectral range from 5.0 µm to 100 µm is shown in Fig. 5.14 together with the corresponding expanded uncertainty ($k = 2$). The FIR-IS measurements were performed at room temperature ($T \approx 25\,^{\circ}\mathrm{C}$) with an incidence angle of 8°. The measured reflectance is compared with reference data derived from spectral emittance measurements performed at PTB using EMAF at a sample temperature of 80 °C and an observation angle of 10°. All FIR-IS reflectance results presented in the following sections correspond to the radiometrically corrected directional–hemispherical reflectance $R_s(\lambda)$.

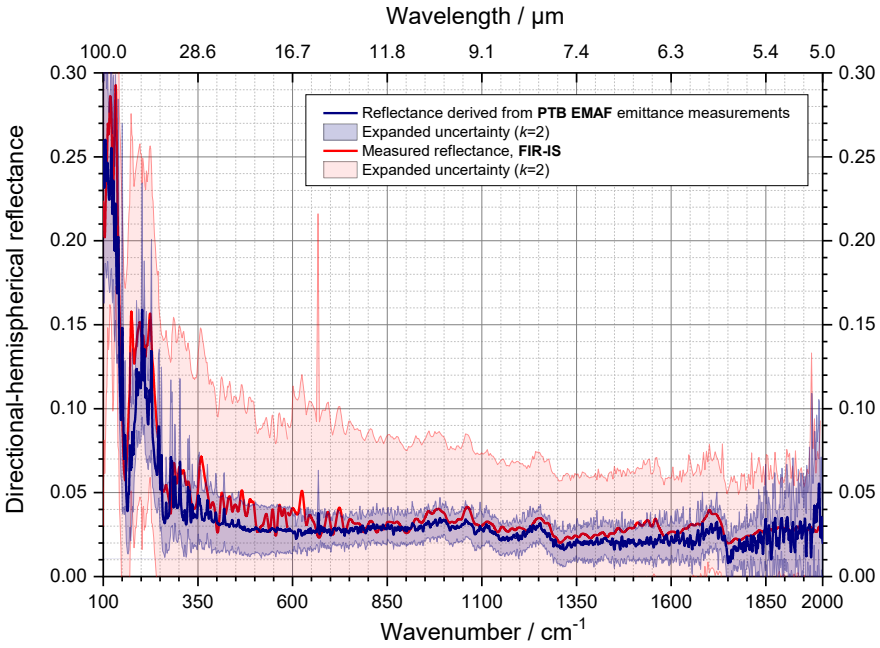


Fig. 5.14. Directional–hemispherical reflectance $R_s(\lambda)$ of the Nextel 811-21 coating over the extended spectral range, combining MIR and FIR measurements. The transition between the MIR configuration with the KBr beamsplitter and the FIR configuration with the Mylar beamsplitter occurs at 600 cm⁻¹, corresponding to 16.7 µm. The FIR-IS data were measured at $T \approx 25\,^{\circ}\mathrm{C}$ and an incidence angle of 8° and are shown in red. The blue curve represents the reference reflectance derived from PTB EMAF directional spectral emittance measurements performed at $T = 80\,^{\circ}\mathrm{C}$ and an observation angle of 10°. The shaded regions indicate the expanded uncertainty ($k = 2$).

In the MIR spectral range, corresponding approximately to wavenumbers from 2000 cm⁻¹ to 600 cm⁻¹, the reflectance remains at a low level and exhibits only minor

https://doi.org/10.7795/110.20260928

spectral variation. The measured curve is smooth and does not show pronounced spectral features, which is consistent with the expected behaviour of highly absorbing coatings. The agreement with the reference data is very good over the entire MIR range, with deviations remaining well within the expanded uncertainty. The relatively small uncertainty observed in this region reflects the favourable measurement conditions, in particular the high sensitivity of the MCT detector and the sufficiently high signal levels.

Towards lower wavenumbers, in the FIR spectral range below approximately 600 cm^{-1}, an increase in reflectance is observed. This behaviour is consistent with the known radiometric behaviour of such coatings, for which the measured emittance decreases with increasing wavelength, resulting in a corresponding increase in reflectance for optically opaque samples. In particular, the reflectance remains at a low level up to wavelengths of about 33 µm and tends to increase towards longer wavelengths, although local spectral variations are observed in the FIR range.

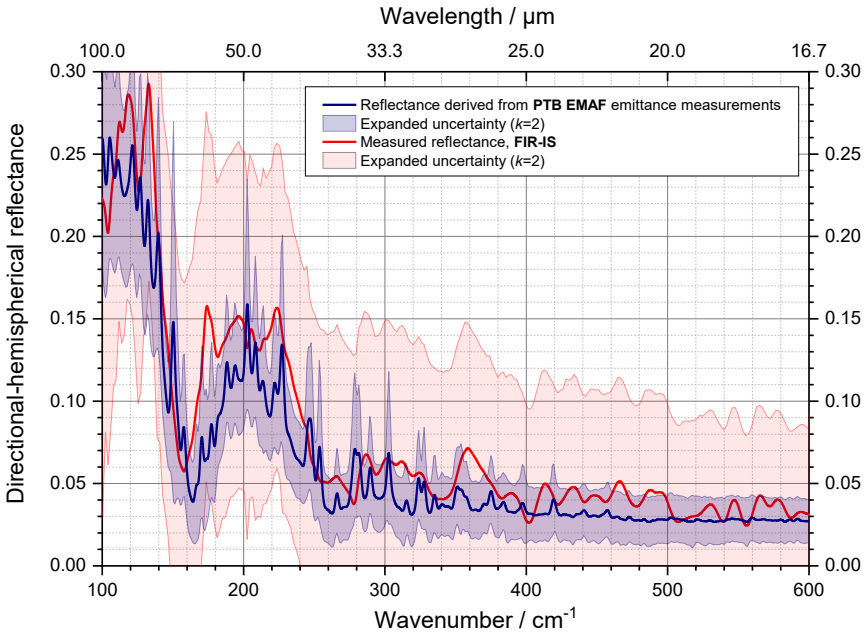


Fig. 5.15. Enlarged FIR view of the Nextel 811-21 results shown in Fig. 5.14. The FIR-IS data were measured at $T \approx 25$ °C and an incidence angle of 8° and are shown in red. The blue curve represents the reference reflectance derived from PTB EMAF directional spectral emittance measurements performed at $T = 80$ °C and an observation angle of 10°. The shaded regions indicate the expanded uncertainty ($k = 2$).

https://doi.org/10.7795/110.20260928

The transition between the MIR and FIR ranges is continuous, and no discontinuities are observed, indicating consistent performance of the measurement system and the applied correction model over the entire spectral range. The expanded uncertainty is relatively large in spectral regions where the measured reflectance of the Nextel coating is low. In these regions, small absolute variations of the measured signal lead to large relative uncertainty values, so that the uncertainty band appears broad compared with the measured reflectance.

Despite the increased uncertainty, the measured reflectance follows the reference data over the investigated spectral range. The largest deviations between measured and reference values occur in the low-wavenumber region, where the uncertainty is highest. However, these deviations remain within the expanded uncertainty and therefore do not indicate a systematic discrepancy.

Overall, the results demonstrate consistent agreement with the reference data within the expanded uncertainty ($k = 2$). In particular, the smooth transition at 600 cm^{-1} between the MIR dataset recorded with the KBr beamsplitter and the FIR dataset recorded with the Mylar beamsplitter confirms the internal consistency of the measurement approach. The results validate the applicability of the FIR-IS, together with the applied radiometric correction and uncertainty evaluation, for directional–hemispherical reflectance measurements of low-reflectance coatings over a wide spectral range.

5.4.2 Laser-structured gold-coated sample

The investigated sample consists of a laser-structured metallic substrate subsequently coated with gold (Fig. 5.16). In contrast to the highly absorbing coatings discussed previously, this sample represents a high-reflectance surface with a complex microstructured geometry. The laser structuring modifies the optical response by introducing multiple scattering, enhanced absorption within the structured relief, and geometrical effects that deviate from the behaviour of an optically smooth metallic surface [85, 86, 87].

https://doi.org/10.7795/110.20260928

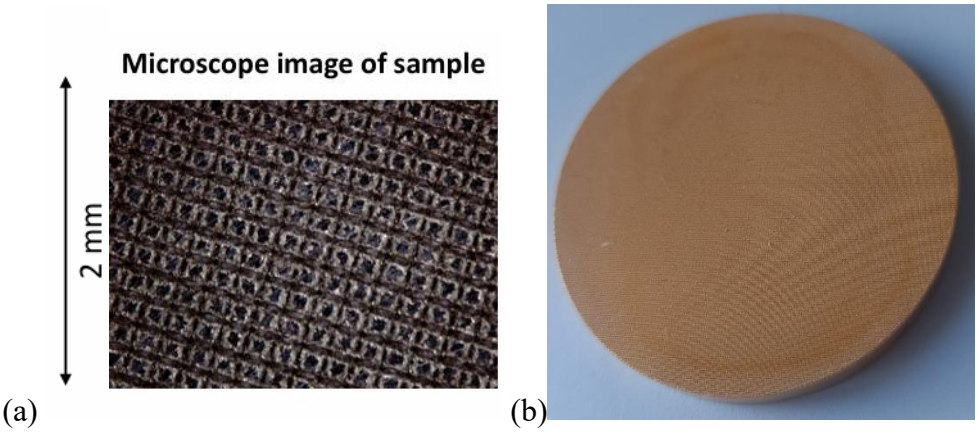


Fig. 5.16. Laser-structured metallic sample: (a) optical microscope image of the structured substrate prior to gold coating; (b) laser-structured surface after deposition of the gold coating. The periodic microstructured geometry modifies the optical response compared with a smooth metallic surface by introducing additional scattering and absorption within the surface relief.

The directional–hemispherical reflectance of the laser-structured gold-coated sample over the spectral range from 5.0 µm to 100 µm is shown in Fig. 5.17 together with the corresponding expanded uncertainty ($k = 2$). The FIR-IS measurements were performed at room temperature ($T \approx 25\ °\mathrm{C}$) and an incidence angle of 8°. The measured reflectance is compared with reference data derived from spectral emittance measurements performed at PTB using EMAF at $T = 80\ °\mathrm{C}$ and an observation angle of 10°.

In the MIR spectral range, the reflectance of the laser-structured gold-coated sample is significantly higher than that of the black coatings. Compared to an optically smooth gold surface, however, the reflectance is reduced and exhibits pronounced spectral structures. Several local minima and maxima are observed in the measured spectrum, indicating a wavelength-dependent optical response of the structured surface. These features are attributed to the combined influence of the laser-induced surface geometry, multiple reflections within the structured surface, and wavelength-dependent redistribution of specular and scattered radiation [88].

The measured reflectance is generally consistent with the PTB reference data within the expanded uncertainty. Compared with the Nextel coating, however, more pronounced local deviations are observed. These deviations are not uniformly distributed over the spectral range but correlate with the characteristic spectral structures of the sample. This behaviour indicates that the comparison is particularly sensitive to the

https://doi.org/10.7795/110.20260928

measurement geometry, sample temperature, angular collection conditions, and the redistribution of specular and diffuse components by the microstructured surface.

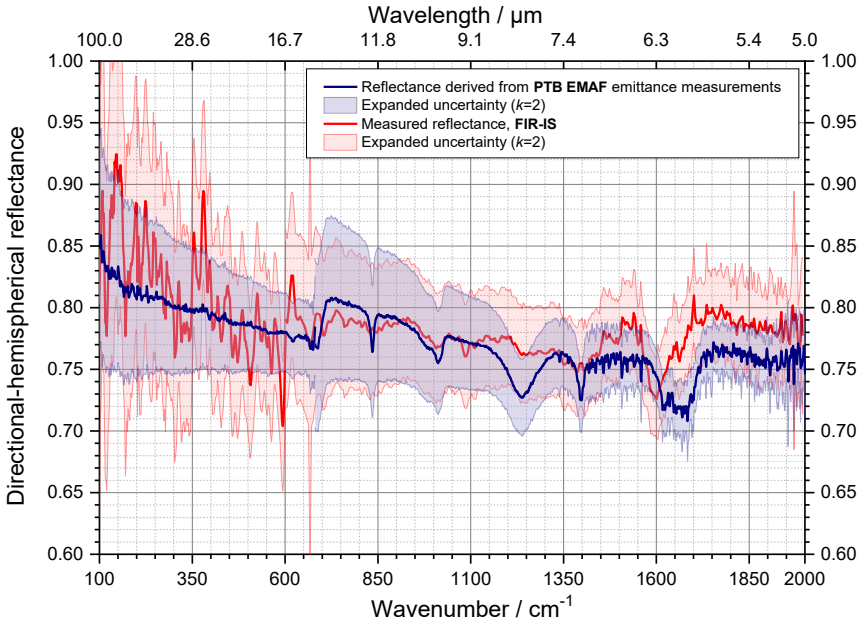


Fig. 5.17. Directional–hemispherical reflectance $R_s(\lambda)$ of the laser-structured gold-coated sample over the spectral range from 5 µm to 100 µm. The FIR-IS data were measured at $T \approx 25\,^{\circ}\mathrm{C}$ and an incidence angle of 8° and are shown in red. The blue curve represents the reference reflectance derived from PTB EMAF directional spectral emittance measurements performed at $T = 80\,^{\circ}\mathrm{C}$ and an observation angle of 10°. The shaded regions indicate the expanded uncertainty of the measurements $(k = 2)$. The reduced reflectance compared with an optically smooth gold surface and the pronounced spectral structures reflect the influence of the laser-induced surface geometry.

In the FIR spectral range below 600 cm⁻¹, the reflectance remains relatively high and shows pronounced spectral modulation. The FIR-IS data reproduce the general spectral behaviour of the reference data, although local deviations between the measured and reference curves become more visible in this region. These deviations are attributed to the complex optical response of the laser-induced surface structure and to the different measurement conditions, including sample temperature and angular collection geometry.

The measured reflectance spectrum shows a continuous transition between the MIR and FIR ranges, with no discontinuity at the detector and beamsplitter changeover around 600 cm⁻¹. This confirms the internal consistency of the measurement procedure

https://doi.org/10.7795/110.20260928

and demonstrates that the applied correction model is applicable also to high-reflectance samples with complex surface structures.

Overall, the results show that the FIR-IS is capable of reproducing the general spectral behaviour of the laser-structured gold-coated surface, including its characteristic spectral features. At the same time, the comparison demonstrates that structured high-reflectance samples represent one of the most demanding cases for integrating-sphere radiometry. Because only a small fraction of the incident radiation is absorbed, the measurement becomes highly sensitive to angular redistribution, sphere-wall reflectance, port losses, and correction parameters. The local deviations observed in parts of the FIR range therefore reflect the increased sensitivity of this sample class to the measurement configuration rather than a systematic inconsistency of the FIR-IS measurement.

5.4.3 Aeroglaze Z306 coating (99 µm)

Aeroglaze Z306 is an absorptive polyurethane coating widely used in aerospace applications due to its high thermal emittance, mechanical stability, and suitability for vacuum environments [89]. It is typically applied as a spray coating on metallic substrates and is designed to provide low reflectance and high absorption over a broad spectral range [90].

For the Aeroglaze Z306 sample investigated in this work, the coating thickness of approximately 99 µm is comparable to the characteristic wavelengths in the far-infrared spectral range. Therefore, the measured radiative behaviour is not expected to be governed solely by reflection at the coating surface. Instead, radiation can partially penetrate into the coating layer, interact with the underlying reflective substrate, and undergo multiple reflections at the coating interfaces. This can give rise to interference-related spectral features whose spacing on the wavenumber scale is determined by the optical thickness of the layer, i.e. by the product of physical coating thickness and refractive index. The observed spectral structure of Aeroglaze Z306 is therefore interpreted as a layer-related effect of the finite coating thickness rather than as a purely surface-scattering effect.

The radiative properties of Aeroglaze Z306 coatings, including their spectral emittance and the influence of thickness-dependent interference effects, have been extensively investigated at PTB. A detailed characterization is provided in the literature,

https://doi.org/10.7795/110.20260928

in particular in [91], where the complex behaviour of this material in the FIR spectral range is discussed.

In the present work, the directional–hemispherical reflectance $R_s(\lambda)$ of an Aeroglaze Z306 coating with a thickness of 99 µm was measured with the FIR-IS at room temperature ($T \approx 25\,^{\circ}\mathrm{C}$) and an incidence angle of 8°. The results are compared with two independent PTB reference datasets obtained using different measurement approaches. The first dataset is derived from spectral emittance measurements performed with EMAF, while the second dataset corresponds to directional–directional spectral reflectance measured using a Bruker A519 reflectance accessory for the VERTEX 80v spectrometer. These two comparisons are shown separately in Figs. 5.18 and 5.19, respectively.

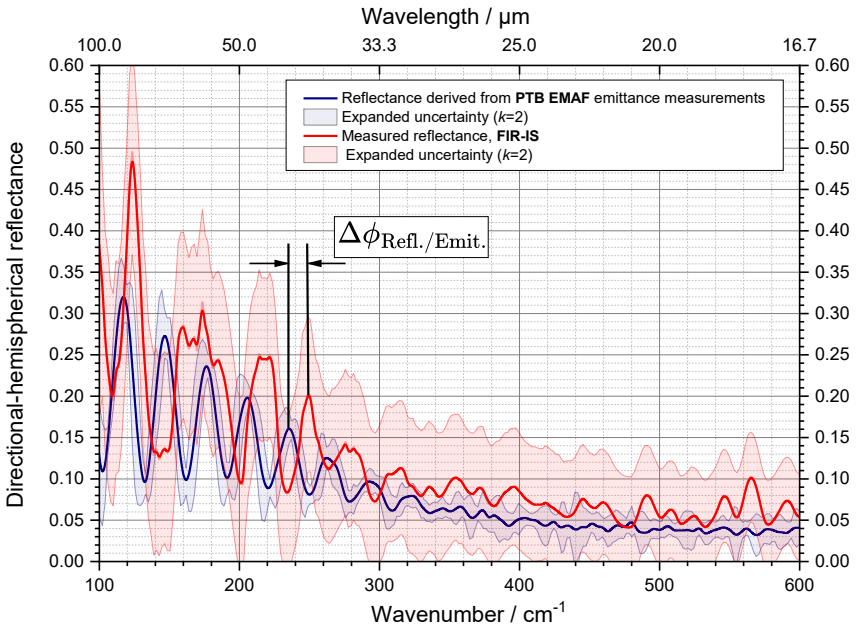


Fig. 5.18. Directional–hemispherical reflectance $R_s(\lambda)$ of the Aeroglaze Z306 coating with a thickness of 99 µm. The FIR-IS data were measured at $T \approx 25\,^{\circ}\mathrm{C}$ and an incidence angle of 8° and are shown in red. The blue curve represents the reference reflectance derived from PTB EMAF directional spectral emittance measurements performed at $T = 150\,^{\circ}\mathrm{C}$ and an observation angle of 10°. The shaded regions indicate the expanded uncertainty of the measurements ($k = 2$). A phase shift $\Delta\phi_{\mathrm{Refl./Emit.}}$ is observed between the spectral modulations.

Figure 5.18 compares the FIR-IS results with the reference data derived from EMAF spectral emittance measurements. In this comparison, the overall magnitude of the reflectance shows good agreement. However, a clear phase shift between the

https://doi.org/10.7795/110.20260928

spectral modulations is observed. This behaviour is characteristic of semi-transparent coatings and is related to the fact that emittance-derived quantities and directly measured reflectance are governed by different optical paths within the coating layer when partial transparency and interference effects are present.

In addition to the EMAF-based comparison, the same Aeroglaze Z306 sample was characterized at PTB using a Bruker A519 reflectance accessory for the VERTEX 80v spectrometer [92]. This accessory enables directional–directional spectral reflectance measurements in a 12°/12° geometry. In contrast to the FIR-IS, the A519 configuration records radiation reflected into a defined observation direction and does not collect the diffuse hemispherical contribution. The comparison between the FIR-IS data and the A519 directional reflectance data is shown in Fig. 5.19.

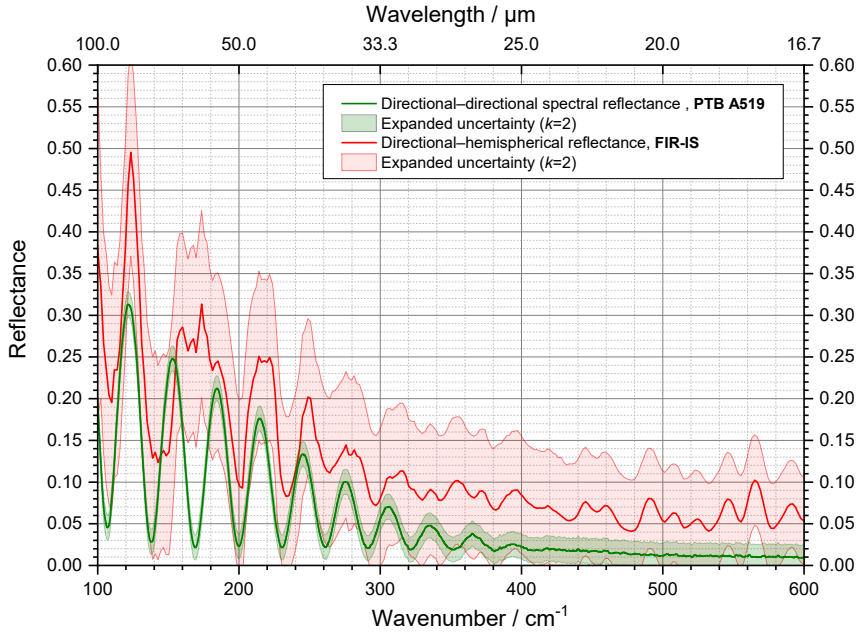


Fig. 5.19. Directional–hemispherical reflectance $R_s(\lambda)$ of the Aeroglaze Z306 coating with a thickness of 99 µm. The FIR-IS data were measured at $T \approx 25$ °C and an incidence angle of 8° and are shown in red. The green curve represents directional–directional spectral reflectance data obtained at PTB using a Bruker A519 reflectance accessory at $T \approx 25$ °C and a 12°/12° geometry. The shaded regions indicate the expanded uncertainty of the measurements ($k = 2$). Good agreement is observed in the spectral position of the interference features, while systematic differences in magnitude arise from the different measurement geometries.

When comparing the FIR-IS results with the A519 data shown in Fig. 5.19, good agreement is observed in the spectral positions of the modulation features. In

https://doi.org/10.7795/110.20260928

particular, the phase of the oscillations coincides over the investigated spectral range, indicating that the interference pattern is reproduced correctly. However, systematic differences in magnitude are observed. These differences are attributed to the different measurement geometries: the A519 accessory measures directional–directional spectral reflectance in a 12°/12° configuration and therefore records mainly the radiation reflected into the specular direction. In contrast, the FIR-IS determines directional–hemispherical reflectance and collects radiation reflected into the entire hemisphere, including both specular and diffusely scattered contributions. The observed difference in magnitude is therefore consistent with the different angular collection conditions of the two measurement approaches.

The present results therefore provide a consistent experimental confirmation of the underlying physical behaviour of the Aeroglaze Z306 coating. The spectral positions of the modulation features are governed primarily by optical interference within the coating layer, while the measured magnitude depends strongly on the angular measurement geometry and on whether diffuse contributions are included.

This observation also highlights the limitations of a direct conversion between emittance and reflectance for semi-transparent materials in the FIR spectral range. While such a relation can be applied to opaque surfaces, it cannot be transferred directly to coatings exhibiting partial transparency and interference effects.

Overall, the results show that the FIR-IS is capable of capturing the characteristic spectral structure of the Aeroglaze Z306 coating and of reproducing the expected magnitude of the directional–hemispherical reflectance within the expanded uncertainty. At the same time, the comparison demonstrates that semi-transparent coatings require careful interpretation, because specular-directional reflectance data, emittance-derived quantities, and directional–hemispherical reflectance are not directly interchangeable.

https://doi.org/10.7795/110.20260928

Conclusion

This dissertation presents the development, realization, and experimental validation of a novel integrating sphere system for directional–hemispherical reflectance measurements in the far-infrared spectral range from 25 µm to 100 µm. The work addressed a significant metrological gap in long-wavelength radiometry, where conventional integrating spheres are limited by the lack of suitable diffuse reflector materials, increased absorption of conventional coatings, and the predominance of specular reflection from metallic surfaces.

The central objective was to develop an integrating sphere concept capable of providing efficient angular redistribution of radiation at long wavelengths while maintaining high reflectance and compatibility with Fourier-transform infrared spectroscopy. To achieve this goal, the work treated surface topology, sphere geometry, fabrication technology, optical coupling, radiometric correction, and uncertainty evaluation as a coupled system-level problem rather than as independent design tasks.

A major outcome of the work was the development and selection of the RHFS-800 surface topology as the internal scattering surface of the integrating sphere. Starting from numerical surface generation and ray-tracing analysis, different structured surface concepts were evaluated with respect to their ability to redistribute reflected radiation over a broad angular range. The RHFS-800 topology was identified as the most suitable candidate because it provides broad diffuse-like scattering behaviour, is mathematically reproducible, and can be transferred to additive manufacturing. This surface concept forms the functional basis of the far-infrared integrating sphere.

The RHFS-800 topology was subsequently transferred from a planar geometry to a spherical configuration. A dedicated transformation procedure was developed in order to preserve the characteristic surface statistics and avoid distortions caused by the convergence of spherical coordinates. This enabled the realization of a structured internal sphere surface while maintaining the angular redistribution properties established in the planar surface studies.

The integrating sphere was realized as a segmented additive-manufactured system with an internal diameter of 150 mm and multiple functional ports for different measurement configurations. Stereolithography was selected as the fabrication method

https://doi.org/10.7795/110.20260928

because it provided sufficient geometrical fidelity, reproducibility, and flexibility for iterative development. The polymer sphere segments were metallized with a NiCr adhesion layer and a gold coating to provide the high reflectance required for efficient multiple reflections in the far-infrared. Measurements of a planar gold-coated reference sample confirmed the low spectral emittance and corresponding high reflectance of the deposited gold coating. Together with the spherical cavity geometry and the RHFS-800 topology, the gold coating provides the low-loss reflective boundary required for stable integrating performance.

A dedicated external optical relay system was developed to couple the integrating sphere to a Bruker VERTEX 80v FTIR spectrometer. The optical system enables controlled transport of the incident radiation path from the spectrometer to the sphere and of the detected radiation path from the sphere back toward the detector configuration. Special attention was given to optical throughput, beam separation, alignment reproducibility, stray-radiation suppression, and compatibility with different detector arrangements. The resulting setup forms a complete measurement system, referred to as FIR-IS, consisting of the FTIR spectrometer, external optical relay system, structured integrating sphere, and detector configuration.

The measurement concept was experimentally implemented using the substitution method. Although the sphere design supports both directional–hemispherical reflectance and transmittance configurations, the experimental validation presented in this work focused on reflectance. Initial measurements in the MIR range were used to verify the optical alignment and measurement procedure under favourable signal conditions. The measurements were then extended to the FIR range using a FDTGS detector mounted directly at the integrating sphere, which reduced optical losses and improved the signal-to-noise ratio compared with the external bolometer path.

A radiometric correction model was implemented to account for real-system effects in integrating-sphere measurements, including finite sphere-wall reflectance, port geometry, and residual background signal. The correction model was implemented in a LabVIEW-based data-processing routine and applied pointwise over the spectral range. The sphere-wall reflectance used in the model was derived from spectral emittance measurements of a planar gold-coated reference sample coated together with the sphere components. This approach provided the best available traceable estimate of the reflectance assigned to the gold-coated sphere wall.

https://doi.org/10.7795/110.20260928

A spectral uncertainty budget was established in accordance with the GUM. The uncertainty analysis included contributions from the measured reflectance, underground signal, sphere-wall reflectance, and geometrical parameters of the sphere. The input uncertainties were treated as standard uncertainties and propagated through the correction model, while the final expanded uncertainty was reported using a coverage factor of $k = 2$. The analysis showed that the dominant contribution to the combined uncertainty originates from the sphere-wall reflectance, whereas contributions from measurement repeatability and geometrical parameters are comparatively small over most of the investigated spectral range.

The FIR-IS was validated using samples with different radiative properties, including the low-reflectance Nextel 811-21 coating, a laser-structured gold-coated sample, and a semi-transparent Aeroglaze Z306 coating. For the Nextel coating, the measured directional–hemispherical reflectance showed good agreement with PTB EMAF reference data over the investigated spectral range. The smooth transition between MIR and FIR measurements confirmed the internal consistency of the measurement approach. For the laser-structured gold-coated sample, the system reproduced the characteristic spectral features of the structured surface and demonstrated applicability to high-reflectance samples with complex surface morphology. For Aeroglaze Z306, the comparison with different PTB reference datasets showed that semi-transparent coatings require careful interpretation, since specular-directional reflectance data, emittance-derived quantities, and directional–hemispherical reflectance are not directly interchangeable.

Overall, the results demonstrate that the developed FIR-IS can be used for directional–hemispherical reflectance measurements in the far-infrared spectral range using an integrating sphere specifically designed for long-wavelength operation. The work presents a design–fabrication–measurement–correction–validation chain for FIR integrating-sphere radiometry. It shows that a structured gold-coated internal surface provides the angular redistribution and low-loss reflective boundary required for integrating-sphere operation beyond the spectral range accessible with conventional diffuse coatings.

The developed system supports far-infrared material characterization and metrological validation of directional–hemispherical radiative quantities. It is relevant for thermal engineering, infrared material science, radiative transfer modelling, and space-

https://doi.org/10.7795/110.20260928

related radiometry. In particular, the availability of traceable laboratory measurement methods in the 25 μm to 100 μm range is important for applications connected with Earth observation and climate missions such as ESA FORUM [6, 7, 8], where reliable far-infrared radiative data are required for instrument calibration, model validation, and interpretation of outgoing longwave radiation.

Future work should focus on further reducing the uncertainty contribution associated with the sphere-wall reflectance, improving the characterization of the structured gold-coated internal surface, and optimizing detector coupling for external bolometric detection. Additional work is also required to experimentally validate the transmittance configuration and to extend the range of investigated materials. Nevertheless, the present work demonstrates the feasibility of a far-infrared integrating sphere based on a structured surface topology and provides a metrologically traceable foundation for future developments in FIR directional–hemispherical radiometry.

https://doi.org/10.7795/110.20260928

Acknowledgements

I would like to express my sincere gratitude to my doctoral supervisor, **Prof. Dr.-Ing. habil. S. Völker** from the Chair of Lighting Technology (FG Lichttechnik) at Technische Universität Berlin, for his supervision, support, and guidance throughout this doctoral work.

I am deeply grateful to **Dr. Jörg Hollandt** and **Dr. Christian Monte** for giving me the opportunity to carry out this research at PTB and for their continuous scientific support, valuable discussions, and trust during the development of this work.

I would also like to thank **Dr. Andreas Steiger**, **Dr. Albert Adibekyan**, **Dr. Benjamin Röben**, and **Dirk Fehse** for their valuable assistance, technical support, discussions, and critical feedback at different stages of this dissertation. Their expertise and willingness to help contributed significantly to the realization and validation of the measurement system presented in this work.

Special thanks are due to the entire team of **PTB Working Department 7.3** for the supportive working environment, technical assistance, and many helpful discussions during the course of this project.

Finally, I would like to express my heartfelt gratitude to my parents for their unconditional support, encouragement, and patience throughout my studies and doctoral research.

https://doi.org/10.7795/110.20260928

References

[1] R. Siegel and J. R. Howell. Thermal Radiation Heat Transfer. 4th ed. New York: Taylor & Francis, 2002. ISBN: 978-1-56032-839-1.

[2] E. D. Palik, ed. Handbook of Optical Constants of Solids. San Diego: Academic Press, 1998. ISBN: 978-0-12-544423-1.

[3] A. Rogalski. Infrared Detectors. 2nd ed. Boca Raton: CRC Press, 2010. DOI: 10.1201/b10319. ISBN: 978-1-4200-7671-4.

[4] J. Harries, B. Carli, R. Rizzi, C. Serio, M. Mlynczak and L. Palchetti. The far-infrared Earth. Reviews of Geophysics. 2008, Vol. 46, RG4004. DOI: 10.1029/2007RG000233.

[5] C. Röske and M. Birk. Water vapor self-continuum measurements in the infrared atmospheric window and ν_2 band region (700–2000 cm^{-1}). Journal of Quantitative Spectroscopy and Radiative Transfer. 2025, Vol. 347, 109602. DOI: 10.1016/j.jqsrt.2025.109602.

[6] European Space Agency (ESA). FORUM Mission Documentation (ESA Earth Explorer Programme). 2022. [Online]. Available: https://www.esa.int/Applications/Observing_the_Earth/FutureEO/Preparing_for_tomorrow/Scientific_and_technical_mission_documents

[7] European Space Agency (ESA). FORUM Mission: Science Objectives and Requirements. ESA, 2020.

[8] L. Palchetti, H. Brindley, R. Bantges, S. A. Buehler, C. Camy-Peyret, B. Carli, U. Cortesi, S. Del Bianco, G. Di Natale, B. M. Dinelli, D. Feldman, X. L. Huang, L. C.-Labonnote, Q. Libois, T. Maestri, M. G. Mlynczak, J. E. Murray, H. Oetjen, M. Ridolfi, M. Riese, J. Russell, R. Saunders and C. Serio. FORUM: Unique Far-Infrared Satellite Observations to Better Understand How Earth Radiates Energy to Space. Bulletin of the American Meteorological Society. 2020, Vol. 101, No. 12, pp. E2030–E2046. DOI: 10.1175/BAMS-D-19-0322.1.

[9] T. A. Blake, T. J. Johnson, R. G. Tonkyn, B. M. Forland, T. L. Myers, C. S. Brauer and Y. Su. Methods for quantitative infrared directional-hemispherical and diffuse

https://doi.org/10.7795/110.20260928

reflectance measurements using an FTIR and a commercial integrating sphere. Applied Optics. 2018, Vol. 57, No. 3, pp. 432–446. DOI: 10.1364/AO.57.000432.

[10] L. M. Hanssen. Integrating-sphere system and method for absolute measurement of transmittance, reflectance, and absorptance of specular samples. Applied Optics. 2001, Vol. 40, No. 19, pp. 3196–3204. DOI: 10.1364/AO.40.003196.

[11] F. E. Nicodemus, J. C. Richmond, J. J. Hsia, I. W. Ginsberg and T. Limperis. Geometrical Considerations and Nomenclature for Reflectance. Washington, DC: National Bureau of Standards, 1977. NBS Monograph 160. DOI: 10.6028/NBS.MONO.160.

[12] J. Hameury, B. Hay and J.-R. Filtz. Measurement of Infrared Spectral Directional Hemispherical Reflectance and Emissivity at BNM-LNE. International Journal of Thermophysics. 2005, Vol. 26, No. 6, pp. 1973–1983. DOI: 10.1007/s10765-005-8609-0.

[13] J. A. Jacquez and H. F. Kuppenheim. Theory of the Integrating Sphere. Journal of the Optical Society of America. 1955, Vol. 45, No. 6, pp. 460–470. DOI: 10.1364/JOSA.45.000460.

[14] Labsphere Inc. Integrating Sphere Theory and Applications. North Sutton, NH: Labsphere Inc., 2006.

[15] Labsphere Inc. Spectralon Diffuse Reflectance Material — Technical Guide. North Sutton, NH: Labsphere Inc., 2023. [Online]. Available: https://www.labsphere.com/wp-content/uploads/2023/01/Spectralon-Diffuse-Reflectance-Material-Tech-Guide.pdf.

[16] P. Beckmann and A. Spizzichino. The Scattering of Electromagnetic Waves from Rough Surfaces. Oxford: Pergamon Press, 1963. ISBN: 978-0-08-010007-4.

[17] J. A. Ogilvy. Theory of Wave Scattering from Random Rough Surfaces. Bristol: Adam Hilger, 1991. ISBN: 978-0-7503-0063-6.

[18] H. E. Bennett and J. O. Porteus. Relation Between Surface Roughness and Specular Reflectance at Normal Incidence. Journal of the Optical Society of America. 1961, Vol. 51, No. 2, pp. 123–129. DOI: 10.1364/JOSA.51.000123.

https://doi.org/10.7795/110.20260928

[19] J. C. Stover. Optical Scattering: Measurement and Analysis. New York: McGraw-Hill, 1990. ISBN: 978-0-07-061814-5.

[20] X. Wang and J. R. Izatt. Diffuse Reflecting Surfaces for the Infrared and Far Infrared. Applied Optics. 1993, Vol. 32, No. 25, pp. 4755–4762. DOI: 10.1364/AO.32.004755.

[21] C. Monte and J. Hollandt. The determination of the uncertainties of spectral emissivity measurements in air at the PTB. Metrologia. 2010, Vol. 47, No. 2, pp. S172–S181. DOI: 10.1088/0026-1394/47/2/S14.

[22] International Organization for Standardization. ISO 80000-7:2019. Quantities and units — Part 7: Light and radiation. Geneva: ISO, 2019.

[23] C. K. Hsieh and K. C. Su. Thermal radiative properties of glass from 0.32 to 206 μm. Solar Energy. 1979, Vol. 22, No. 1, pp. 37–43. DOI: 10.1016/0038-092X(79)90057-4.

[24] W. W. Beens, M. Sikkens and J. L. Verster. An emissometer with high accuracy for determination of the total hemispherical emittance of surfaces. Journal of Physics E: Scientific Instruments. 1980, Vol. 13, No. 8, pp. 873–876. DOI: 10.1088/0022-3735/13/8/018.

[25] P. L. Richards. Bolometers for infrared and millimeter waves. Journal of Applied Physics. 1994, Vol. 76, No. 1, pp. 1–24. DOI: 10.1063/1.357128.

[26] J. C. Mather. Bolometer noise: nonequilibrium theory. Applied Optics. 1982, Vol. 21, No. 6, pp. 1125–1129. DOI: 10.1364/AO.21.001125.

[27] P. R. Griffiths and J. A. de Haseth. Fourier Transform Infrared Spectrometry. 2nd ed. Hoboken, NJ: Wiley, 2007. DOI: 10.1002/047010631X. ISBN: 978-0-471-19404-0.

[28] B. C. Smith. Fundamentals of Fourier Transform Infrared Spectroscopy. 2nd ed. Boca Raton: CRC Press, 2011. DOI: 10.1201/b10777. ISBN: 978-1-4200-6929-7.

[29] L. M. Hanssen and K. A. Snail. Integrating Spheres for Mid- and Near-Infrared Reflection Spectroscopy. In: J. M. Chalmers and P. R. Griffiths, Eds. Handbook of Vibrational Spectroscopy. Chichester: Wiley, 2002, pp. 1–18. DOI: 10.1002/0470027320.s2405.

https://doi.org/10.7795/110.20260928

[30] D. K. Edwards, J. T. Gier, K. E. Nelson and R. D. Roddick. Integrating Sphere for Imperfectly Diffuse Samples. Journal of the Optical Society of America. 1961, Vol. 51, No. 11, pp. 1279–1288. DOI: 10.1364/JOSA.51.001279.

[31] L. M. Hanssen, C. P. Cagran, A. V. Prokhorov, S. N. Mekhontsev and V. B. Khromchenko. Use of a High-Temperature Integrating Sphere Reflectometer for Surface-Temperature Measurements. International Journal of Thermophysics. 2007, Vol. 28, No. 2, pp. 566–580. DOI: 10.1007/s10765-007-0180-4.

[32] D. M. Mittleman, Ed. Sensing with Terahertz Radiation. Berlin, Heidelberg: Springer, 2003. DOI: 10.1007/978-3-540-45601-8. ISBN: 978-3-540-43110-7.

[33] A. Ishimaru. Wave Propagation and Scattering in Random Media. New York: Academic Press, 1978. ISBN: 978-0-12-374701-3.

[34] B. Hapke. Theory of Reflectance and Emittance Spectroscopy. 2nd ed. Cambridge: Cambridge University Press, 2012. ISBN: 978-0-521-88349-8.

[35] J. M. Elson and J. M. Bennett. Relation Between the Angular Dependence of Scattering and the Statistical Properties of Optical Surfaces. Journal of the Optical Society of America. 1979, Vol. 69, No. 1, pp. 31–47. DOI: 10.1364/JOSA.69.000031.

[36] E. L. Church. The Measurement of Surface Texture and Topography by Differential Light Scattering. Wear. 1979, Vol. 57, No. 1, pp. 93–105. DOI: 10.1016/0043-1648(79)90143-1.

[37] W. J. Smith. Modern Optical Engineering: The Design of Optical Systems. 4th ed. New York: McGraw-Hill, 2007. ISBN: 978-0-07-159375-5.

[38] Ansys Zemax. OpticStudio User Manual. Canonsburg, PA: Ansys, 2023.

[39] M. A. Ordal, L. L. Long, R. J. Bell, S. E. Bell, R. R. Bell, R. W. Alexander Jr. and C. A. Ward. Optical Properties of the Metals Al, Co, Cu, Au, Fe, Pb, Ni, Pd, Pt, Ag, Ti, and W in the Infrared and Far Infrared. Applied Optics. 1983, Vol. 22, No. 7, pp. 1099–1120. DOI: 10.1364/AO.22.001099.

[40] I. Gibson, D. Rosen and B. Stucker. Additive Manufacturing Technologies: 3D Printing, Rapid Prototyping, and Direct Digital Manufacturing. 2nd ed. New York: Springer, 2015. DOI: 10.1007/978-1-4939-2113-3. ISBN: 978-1-4939-2112-6.

https://doi.org/10.7795/110.20260928

[41] W. M. Steen and J. Mazumder. Laser Material Processing. 4th ed. London: Springer, 2010. DOI: 10.1007/978-1-84996-062-5. ISBN: 978-1-84996-061-8.

[42] R. Leach, Ed. Optical Measurement of Surface Topography. Berlin, Heidelberg: Springer, 2011. DOI: 10.1007/978-3-642-12012-1. ISBN: 978-3-642-12011-4.

[43] A. Steiger, M. Kehrt, C. Monte and R. Müller. Traceable Terahertz Power Measurement from 1 THz to 5 THz. Optics Express. 2013, Vol. 21, No. 12, pp. 14466–14473. DOI: 10.1364/OE.21.014466.

[44] Labsphere Inc. Reflectance Coatings and Materials. North Sutton, NH: Labsphere Inc., 2024. [Online]. Available: https://www.labsphere.com/wp-content/uploads/2024/05/ReflectanceCoatingsMaterialsTechGuideRev04.pdf.

[45] Gigahertz-Optik GmbH. Design Criteria for the Configuration of Integrating Spheres for Material Characterization (ISM). Türkenfeld: Gigahertz-Optik GmbH. [Online]. Available: https://www.gigahertz-optik.com/en-us/service-and-support/knowledge-base/design-criteria-ism/

[46] J. Hwang, D.-J. Shin and K. R. Jeong. Integrating Sphere-Based Relative Methods for Reflection Measurements. Metrologia. 2016, Vol. 53, No. 6, pp. 1231–1242. DOI: 10.1088/0026-1394/53/6/1231.

[47] ASTM International. ASTM E903-20. Standard Test Method for Solar Absorptance, Reflectance, and Transmittance of Materials Using Integrating Spheres. West Conshohocken, PA: ASTM International, 2020.

[48] L. J. Sandilands and T. Cameron. Integrating Sphere Port Error in Diffuse Reflectance Measurements. Applied Optics. 2023, Vol. 62, No. 29, pp. 7700–7705. DOI: 10.1364/AO.497962.

[49] D. M. Mattox. Handbook of Physical Vapor Deposition (PVD) Processing. 2nd ed. Norwich, NY: William Andrew, 2010. DOI: 10.1016/C2009-0-18800-1. ISBN: 978-0-8155-2037-5.

[50] M. Ohring. Materials Science of Thin Films: Deposition and Structure. 2nd ed. San Diego: Academic Press, 2001. ISBN: 978-0-12-524975-1.

https://doi.org/10.7795/110.20260928

[51] A. R. Korb, P. Dybwad, W. Wadsworth and J. W. Salisbury. Portable Fourier Transform Infrared Spectroradiometer for Field Measurements of Radiance and Emissivity. Applied Optics. 1996, Vol. 35, No. 10, pp. 1679–1692. DOI: 10.1364/AO.35.001679.

[52] K. Schwertz and J. H. Burge. Field Guide to Optomechanical Design and Analysis. Bellingham, WA: SPIE Press, 2012. ISBN: 978-0-8194-9161-9.

[53] F. P. W. Melchels, J. Feijen and D. W. Grijpma. A Review on Stereolithography and Its Applications in Biomedical Engineering. Biomaterials. 2010, Vol. 31, No. 24, pp. 6121–6130. DOI: 10.1016/j.biomaterials.2010.04.050.

[54] C. K. Chua and K. F. Leong. 3D Printing and Additive Manufacturing: Principles and Applications. 4th ed. Singapore: World Scientific, 2014. DOI: 10.1142/9008. ISBN: 978-981-4578-49-3.

[55] R. W. Messler. Joining of Materials and Structures: From Pragmatic Process to Enabling Technology. Burlington, MA: Elsevier Butterworth-Heinemann, 2004. ISBN: 978-0-7506-7757-8.

[56] DIN. DIN EN ISO 9001:2025-09 Draft. Quality management systems — Requirements (ISO/DIS 9001:2025). Berlin: DIN, 2025.

[57] ISO/ASTM International. ISO/ASTM 52927:2024. Additive manufacturing — General principles — Main characteristics and corresponding test methods. Geneva: ISO, 2024.

[58] T. D. Ngo, A. Kashani, G. Imbalzano, K. T. Q. Nguyen and D. Hui. Additive Manufacturing (3D Printing): A Review of Materials, Methods, Applications and Challenges. Composites Part B: Engineering. 2018, Vol. 143, pp. 172–196. DOI: 10.1016/j.compositesb.2018.02.012.

[59] ASTM International. ASTM F2792-12a. Standard Terminology for Additive Manufacturing Technologies. West Conshohocken, PA: ASTM International, 2012.

[60] ISO/ASTM International. ISO/ASTM 52900:2021. Additive manufacturing — General principles — Fundamentals and vocabulary. Geneva: ISO, 2021.

[61] CREAVAC GmbH. Innovative Beschichtungstechnologien und Vakuumanlagen. Dresden: CREAVAC GmbH. [Online]. Available: https://www.creavac.de/de/unternehmen/

https://doi.org/10.7795/110.20260928

[62] W. L. Wolfe and G. J. Zissis, Eds. The Infrared Handbook. Revised ed. Ann Arbor, MI: Environmental Research Institute of Michigan, 1985. ISBN: 978-0-9603590-1-1.

[63] A. D. Rakić, A. B. Djurišić, J. M. Elazar and M. L. Majewski. Optical Properties of Metallic Films for Vertical-Cavity Optoelectronic Devices. Applied Optics. 1998, Vol. 37, No. 22, pp. 5271–5283. DOI: 10.1364/AO.37.005271.

[64] C. Monte, B. Gutschwager, S. P. Morozova and J. Hollandt. Radiation Thermometry and Emissivity Measurements Under Vacuum at the PTB. International Journal of Thermophysics. 2009, Vol. 30, pp. 203–219. DOI: 10.1007/s10765-008-0442-9.

[65] NASA Goddard Space Flight Center. Outgassing Database. Greenbelt, MD: NASA. [Online]. Available: https://etd.gsfc.nasa.gov/capabilities/outgassing-database/

[66] ASTM International. ASTM E595-15(2021). Standard Test Method for Total Mass Loss and Collected Volatile Condensable Materials from Outgassing in a Vacuum Environment. West Conshohocken, PA: ASTM International, 2021.

[67] R. D. Hudson Jr. Infrared System Engineering. Hoboken, NJ: Wiley-Interscience, 2006. ISBN: 978-0-470-09935-3.

[68] J. M. Palmer and B. G. Grant. The Art of Radiometry. Bellingham, WA: SPIE Press, 2009. DOI: 10.1117/3.798237. ISBN: 978-0-8194-7245-8.

[69] M. Born and E. Wolf. Principles of Optics: Electromagnetic Theory of Propagation, Interference and Diffraction of Light. 7th expanded ed. Cambridge: Cambridge University Press, 1999. DOI: 10.1017/CBO9781139644181. ISBN: 978-0-521-64222-4.

[70] W. T. Welford and R. Winston. The Optics of Nonimaging Concentrators: Light and Solar Energy. New York: Academic Press, 1978. ISBN: 978-0-12-745350-7.

[71] Bruker Optics. A515 External Reflection Unit — Technical Documentation. Ettlingen: Bruker Optics.

[72] Bruker Optics. VERTEX 80v User Manual. Ettlingen: Bruker Optics.

[73] D. Malacara, Ed. Optical Shop Testing. 2nd ed. New York: Wiley, 1992. ISBN: 978-0-471-52232-7.

https://doi.org/10.7795/110.20260928

[74] F. J. J. Clarke and J. A. Compton. Correction Methods for Integrating-Sphere Measurement of Hemispherical Reflectance. Color Research & Application. 1986, Vol. 11, No. 4, pp. 253–262. DOI: 10.1002/col.5080110406.

[75] JCGM. Evaluation of Measurement Data — Guide to the Expression of Uncertainty in Measurement. JCGM 100:2008. Sèvres: Joint Committee for Guides in Metrology, 2008.

[76] C. Monte and J. Hollandt. The Measurement of Directional Spectral Emissivity in the Temperature Range from 80 °C to 400 °C at the Physikalisch-Technische Bundesanstalt. High Temperatures–High Pressures. 2010, Vol. 39, pp. 151–164.

[77] M. F. Modest. Radiative Heat Transfer. 3rd ed. Amsterdam: Academic Press, 2013. ISBN: 978-0-12-386944-9.

[78] Acktar Ltd. Metal Velvet — Technical Data. Kiryat-Gat: Acktar Ltd. [Online]. Available: https://de.acktar.com/produkt/metal-velvet/

[79] A. Adibekyan, E. Kononogova, C. Monte and J. Hollandt. High-Accuracy Emissivity Data on the Coatings Nextel 811-21, Herberts 1534, Aeroglaze Z306 and Acktar Fractal Black. International Journal of Thermophysics. 2017, Vol. 38, 89. DOI: 10.1007/s10765-017-2212-z.

[80] J. Manara, M. Arduini-Schuster and L. M. Hanssen. Integrating Sphere Reflectance and Transmittance Intercomparison Measurements for Evaluating the Accuracies of the Achieved Results. High Temperatures–High Pressures. 2009, Vol. 38, No. 3, pp. 259–276.

[81] J. W. Pickering, S. A. Prahl, N. van Wieringen, J. F. Beek, H. J. C. M. Sterenborg and M. J. C. van Gemert. Double-Integrating-Sphere System for Measuring the Optical Properties of Tissue. Applied Optics. 1993, Vol. 32, No. 4, pp. 399–410. DOI: 10.1364/AO.32.000399.

[82] A. Roos and C. G. Ribbing. Interpretation of Integrating Sphere Signal Output for Non-Lambertian Samples. Applied Optics. 1988, Vol. 27, No. 18, pp. 3833–3837. DOI: 10.1364/AO.27.003833.

https://doi.org/10.7795/110.20260928

[83] Mankiewicz Gebr. & Co. Nextel Velvet Coating 811-21. Hamburg: Mankiewicz Gebr. & Co., 2018. [Online]. Available: https://www.nextel-coating.com/de/produkte/nextel-velvet-coating-811-21

[84] S. Matteï and E. Tang-Kwor. Emissivity Measurements for Nextel Velvet Coating 811-21 Between -36 °C and 82 °C. High Temperatures–High Pressures. 2001, pp. 551–556.

[85] E. Kononogova, A. Adibekyan, C. Monte and J. Hollandt. Characterization, Calibration and Validation of an Industrial Emissometer. Journal of Sensors and Sensor Systems. 2019, Vol. 8, pp. 233–242. DOI: 10.5194/jsss-8-233-2019.

[86] A. Y. Vorobyev and C. Guo. Direct Femtosecond Laser Surface Nano/Microstructuring and Its Applications. Laser & Photonics Reviews. 2013, Vol. 7, No. 3, pp. 385–407. DOI: 10.1002/lpor.201200017.

[87] J. Bonse and S. Gräf. Ten Open Questions about Laser-Induced Periodic Surface Structures. Nanomaterials. 2021, Vol. 11, No. 12, 3326. DOI: 10.3390/nano11123326.

[88] Y. Yang, J. Yang, C. Liang and H. Wang. Ultra-Broadband Enhanced Absorption of Metal Surfaces Structured by Femtosecond Laser Pulses. Optics Express. 2008, Vol. 16, No. 15, pp. 11259–11265. DOI: 10.1364/OE.16.011259.

[89] Socomore. Aeroglaze Z306 Absorptive Polyurethane Coating / Aeroglaze Z3 Series. Vannes: Socomore, 2025. [Online]. Available: https://www.socomore.com/en/masterproduct/aeroglaze-z3-series/

[90] European Space Agency. Chemglaze Z306 (also called Aeroglaze). ESA Materials and Processes. [Online]. Available: http://esmat.esa.int/Services/Preferred_Lists/Materials_Lists/a12_3.htm

[91] A. Adibekyan. High-Accuracy Spectral Emissivity Measurement for Industrial and Remote Sensing Applications. PhD dissertation. Wuppertal: Bergische Universität Wuppertal, 2016.

[92] Bruker Optik GmbH. Accurate Reflectance and Transmittance Measurements on Highly Refractive Materials. Ettlingen: Bruker Optik GmbH, 2018.

https://doi.org/10.7795/110.20260928

Bundesministerium
für Wirtschaft
und Energie

Die Physikalisch-Technische Bundesanstalt, das nationale Metrologieinstitut, ist eine wissenschaftlich-technische Bundesoberbehörde im Geschäftsbereich des Bundesministeriums für Wirtschaft und Energie.

PTB

Physikalisch-Technische Bundesanstalt
Nationales Metrologieinstitut
ISNI: 0000 0001 2186 1887

Bundesallee 100
38116 Braunschweig

Presse- und Öffentlichkeitsarbeit

Telefon: (0531) 592-93 21
Fax: (0531) 592-30 08
E-Mail: presse@ptb.de
www.ptb.de